



UNIVERSITY OF AMSTERDAM



**MSc Physics and Astronomy**  
Track: Astronomy & Astrophysics

Master Thesis

---

## Cosmic Carbon Clues

**Understanding the PAH Population in Titan's Upper  
Atmosphere with IR spectroscopy**

---

by

**Florence Stikkelbroeck  
12425567 (UVA)**

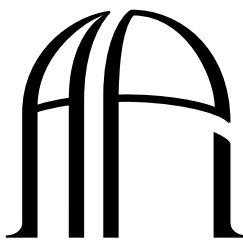
*July 26, 2025*

*60 ECTS*

*September 1, 2024 - July 25, 2025*

*Supervisor:*  
Dr. Alessandra Candian

*Examiner*  
Dr. Jean-Michel Désert



---

**ANTON PANNEKOEK  
INSTITUTE**

# Contents

<b>1</b>	<b>Introduction</b>	<b>4</b>
1.1	Titan . . . . .	5
1.2	Polycyclic Aromatic Hydrocarbons (PAHs) . . . . .	8
1.2.1	PAH features . . . . .	10
1.2.2	Formation of PAHs in Titan’s Atmosphere . . . . .	11
1.2.3	PAHs on Titan . . . . .	12
<b>2</b>	<b>Methods</b>	<b>15</b>
2.1	Preliminary Data Preparation . . . . .	15
2.1.1	Cassini/Huygens VIMS data . . . . .	15
2.1.2	CH <sub>4</sub> NLTE Model . . . . .	16
2.2	Emission model using the NASA Ames Database . . . . .	18
2.2.1	Cascade Emission Model . . . . .	18
2.2.2	Solar Data . . . . .	21
2.2.3	Photoabsorption crosssection . . . . .	21
2.2.4	Content & Constraints . . . . .	23
2.3	Spectral Fitting . . . . .	25
2.3.1	NNLS . . . . .	25
2.3.2	NNLC . . . . .	26
2.3.3	Monte Carlo error Propagation . . . . .	26
2.4	Post-Fit Evaluation and Diagnostics . . . . .	27
2.4.1	Goodness-of-Fit Assessment . . . . .	27
2.4.2	Estimating PAH Occurrence . . . . .	27
<b>3</b>	<b>Results</b>	<b>29</b>
3.1	Re-analysis of VIMS data . . . . .	29
3.2	Refining the Fit with an expanded PAHdb . . . . .	33
3.2.1	Additional constraints to the fit . . . . .	39
3.3	Fits Using PAHdb Version 4.00 . . . . .	42
3.3.1	Physically Constrained Fit with v4.00 ( $N_c < 29$ ) . . . . .	43
<b>4</b>	<b>Discussion</b>	<b>46</b>
4.1	Comparison with López-Puertas et al. (2013) . . . . .	46
4.2	Impact of database updates and constrained fits . . . . .	47

## Contents

---

4.3 Interpretation for Titan’s atmospheric chemistry . . . . .	48
4.4 Methodological limitations . . . . .	49
4.5 Future work . . . . .	50
<b>5 Conclusion</b>	<b>52</b>
<b>A Fitting Results</b>	<b>60</b>
A.1 V1.20 neutrals . . . . .	60
A.1.1 NNLS 900 km . . . . .	60
A.1.2 NNLS 950 km . . . . .	62
A.1.3 NNLS 1000 km . . . . .	63
A.1.4 Monte Carlo simulations . . . . .	64
A.2 V3.20 neutrals + anions . . . . .	65
A.2.1 NNLC 900 km . . . . .	65
A.2.2 NNLC 950 km . . . . .	66
A.2.3 NNLC 1000 km . . . . .	67
A.2.4 Monte Carlo simulations . . . . .	68
A.3 V3.20 neutrals + anions C<29 . . . . .	69
A.3.1 NNLC 900 km . . . . .	69
A.3.2 NNLC 950 km . . . . .	70
A.3.3 NNLC 1000 km . . . . .	71
A.3.4 Monte Carlo simulations . . . . .	72
A.4 V4.00 neutrals + anions . . . . .	73
A.4.1 NNLC 900 km . . . . .	73
A.4.2 NNLC 950 km . . . . .	74
A.4.3 NNLC 1000 km . . . . .	75
A.4.4 Monte Carlo simulations . . . . .	76
A.5 V4.00 neutrals + anions C<29 . . . . .	77
A.5.1 NNLC 900 km . . . . .	77
A.5.2 NNLC 950 km . . . . .	78
A.5.3 NNLC 1000 km . . . . .	79
A.5.4 Monte Carlo simulations . . . . .	80
A.6 Single PAH signals . . . . .	81
<b>B NIST list</b>	<b>85</b>

## Abstract

Titan's upper atmosphere hosts a rich organic chemistry driven by solar radiation, producing a dense haze of hydrocarbons and nitrogen-bearing molecules (Waite et al. 2007; Hörst 2017). Cassini/VIMS revealed an unexplained  $3.28\text{ }\mu\text{m}$  emission feature at 900–1000 km (Dinelli et al. 2013), widely attributed to polycyclic aromatic hydrocarbons (PAHs) (López-Puertas et al. 2013). Understanding the PAH population in Titan's upper atmosphere is important both for constraining haze formation and as an analogue for organic chemistry on early Earth (Sandford et al. 2020; Zahnle et al. 2010). The recent availability of expanded PAH databases and high-resolution observational capabilities with JWST and ALMA makes this topic particularly timely.

We analysed CH<sub>4</sub>-subtracted Cassini/VIMS spectra at 900, 950, and 1000 km using the NASA Ames PAH IR Spectroscopic Database (versions 3.20 and 4.00). Cascade emission spectra were generated and fitted to the observations with non-negative least squares (NNLS) and concentration-weighted NNLC methods, extended with Monte Carlo ensembles (López-Puertas et al. 2013; Maragkoudakis et al. 2024). Improvements over previous work include updated photon cross sections, per-PAH normalisation, and inclusion of anions.

Our results show that Titan's  $3.28\text{ }\mu\text{m}$  emission can be reproduced by a compact population of small, nitrogen-bearing PAHs. UID 527 ( $\text{C}_{10}\text{H}_8\text{N}$ ) appears in every fit and dominates the ensemble. Nitrogenated and anionic species such as UID 278 ( $\text{C}_{13}\text{H}_9\text{N}^-$ ) and UID 382 ( $\text{C}_{10}\text{H}_8^-$ ) are persistent, whereas very large PAHs appear only when size limits are relaxed. The derived ring-size distribution is stable across altitudes and lies between 10 and 18 rings.

These findings indicate that Titan's upper atmosphere is probably shaped by small, stable, nitrogen-rich aromatic species. The persistent presence of UID 527 suggests it may be a genuine carrier of the emission and a key target for follow-up at longer wavelengths, including the  $4.69\text{ }\mu\text{m}$  C≡N feature predicted by laboratory models (Zhou et al. 2025). The results also highlight the need to incorporate anions and PANHs in photochemical models of Titan's atmosphere.

This work strengthens the link between Titan's chemistry and early Earth's prebiotic pathways, providing a framework for future retrievals of PAHs in planetary atmospheres. Expanding the analysis to the full 1–5  $\mu\text{m}$  regime (Allamandola et al. 2021) and to forthcoming data from JWST and ALMA will enable individual molecules to be distinguished and improve constraints on the organic inventory of Titan and similar worlds.

# Chapter 1

## Introduction

Carbon and the molecules it forms are the foundation of life as we know it. DNA, our genetic backbone, is built from carbon-based molecules. In organic chemistry we study molecules made of carbon and hydrogen, also known as hydrocarbons. They form the structural basis of all known biological systems. Among these molecules are polycyclic aromatic hydrocarbons (PAHs): complex molecules composed of fused aromatic rings which contain either 5 or 6 carbons (see Figure 1.1). PAHs are not just biologically relevant, they are also cosmically abundant and play a key role in the chemical evolution of the universe ([Tielens 2008](#)). They have been detected in a wide range of environments, from the interstellar medium to planetary atmospheres ([Tielens 2013](#)). It is estimated that over 20% of all cosmic carbon is stored in PAHs ([Candian et al. 2018](#)). PAHs are widely studied in astrophysics because their strong infrared (IR) emission makes them effective tracers of cosmic carbon.

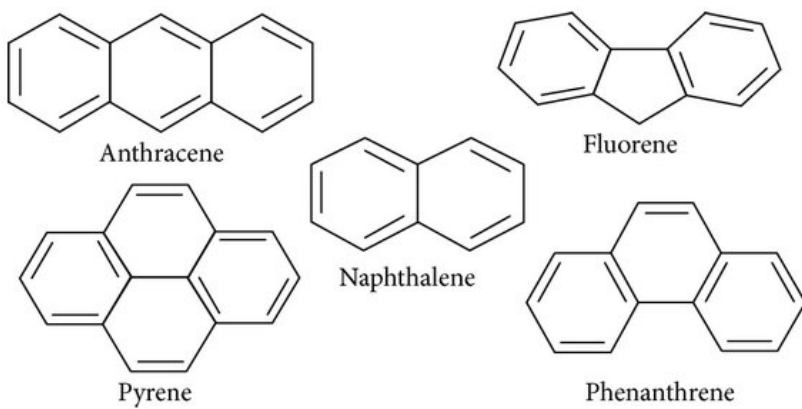


FIG. 1.1 – Example of representative groups of PAHs, containing rings of 5 or 6 carbon atoms ([Nawaz et al. 2014](#)).

One of the most interesting environments where PAHs may occur is Titan, Saturn’s largest moon. Titan’s large, nitrogen-rich atmosphere supports complex organic chemistry (Hörst 2017). Observations reveal a thick orange haze that obscures the surface in optical wavelengths, though it remains visible in the infrared (Figure 1.2). This haze, composed of hydrocarbons and other complex organics including PAHs and nitrogenated analogues, originates in the upper atmosphere and gradually settles onto the surface (Hörst 2017; Waite et al. 2010). However, the detailed mechanisms of haze formation remain poorly understood. Understanding the role of PAHs provides key insight into the link between atmospheric chemistry and surface processes. Titan may also host chemical pathways analogous to those on early Earth (Nixon 2024).

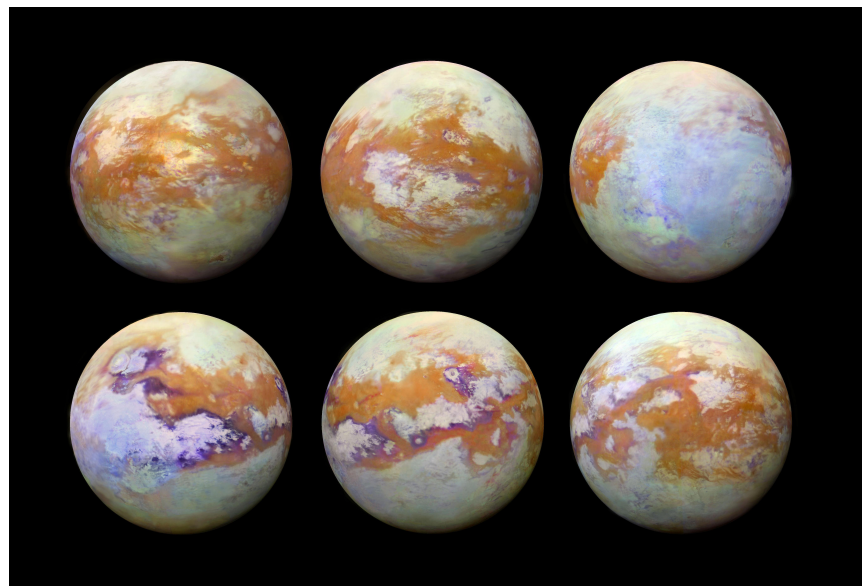


FIG. 1.2 – Infrared Image of Titan’s surface taken by Cassini/Huygens VIMS instrument, composed using 13 years of data.

## 1.1 Titan

Titan is Saturn’s largest moon. This moon is unique in the Solar System as it is the only one with a substantial atmosphere, primarily composed of nitrogen N (95%) and methane CH<sub>4</sub> (5%) (Hörst 2017; Nixon 2024). This composition is very similar to early Earth before there was life (Zahnle et al. 2010). Because the atmosphere is cold and the gravity of Titan is low, the atmosphere extends as far out as 1400 km (Flasar et al. 1981). Despite Titan being only 40% the size of Earth, its atmosphere is 10 times more extended. The discovery of Titan’s atmosphere dates back to the detection of methane by Kuiper (1944), which suggested that complex photochemical reactions

shape its composition. In the upper atmosphere, solar ultraviolet light breaks apart methane ( $\text{CH}_4$ ) and initiates a chain of reactions involving molecular nitrogen ( $\text{N}_2$ ). These processes produce a suite of hydrocarbons, nitriles, and eventually complex haze particles. Current models suggest that PAHs may begin forming around 900 km altitude, as part of this photochemical cascade. Subsequent missions, including Voyager 1 and 2 and the Cassini-Huygens mission (2004–2017), further shaped our understanding of Titan's atmosphere, surface, and climate (Brown et al. 2010). Our current understanding of the particle growth in Titan's atmosphere is summarised in Figure 1.3. The larger aerosol particles are formed lower down in the haze layer, which rain down and interact with the surface. The Cassini spacecraft's remote sensing and in situ measurements confirmed that Titan experiences a methane-based hydrological cycle, including precipitation, rivers, lakes, and seas, making it the only extraterrestrial body with stable surface liquids (Hörst 2017).

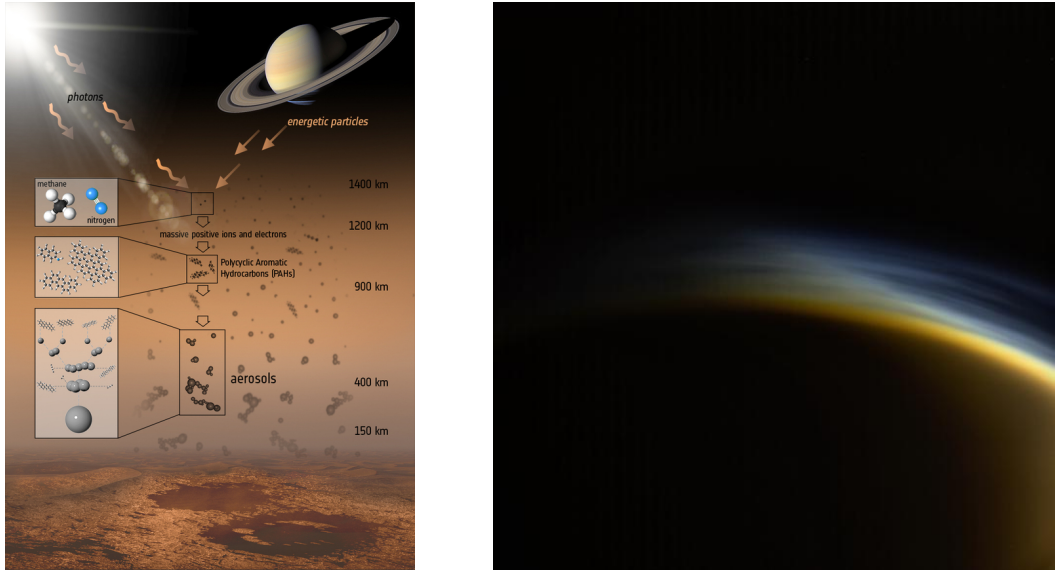


FIG. 1.3 – Structure and haze formation in Titan's atmosphere. Panel (a) Schematic of Particle growth in Titan's atmosphere from 1400 km altitude down to the surface; panel (b) shows the stratified haze layers responsible for Titan's optical appearance.

Titan's thick atmosphere is structured into distinct layers: the troposphere, stratosphere, mesosphere, and thermosphere, resembling Earth's atmospheric structure but governed by vastly different chemical and energy dynamics (Nixon 2024). In Figure 1.4 we see the vertical temperature structure in Titan's atmosphere. There are still outstanding questions about the structure of the upper atmosphere. Note the question marks and dashed lines, which highlight areas of ongoing uncertainty. (Hörst 2017).

Observations revealed the presence of key species in Titan's upper atmosphere, including but not limited to acetylene ( $\text{C}_2\text{H}_2$ ), ethane ( $\text{C}_2\text{H}_6$ ), hydrogen cyanide ( $\text{HCN}$ ),

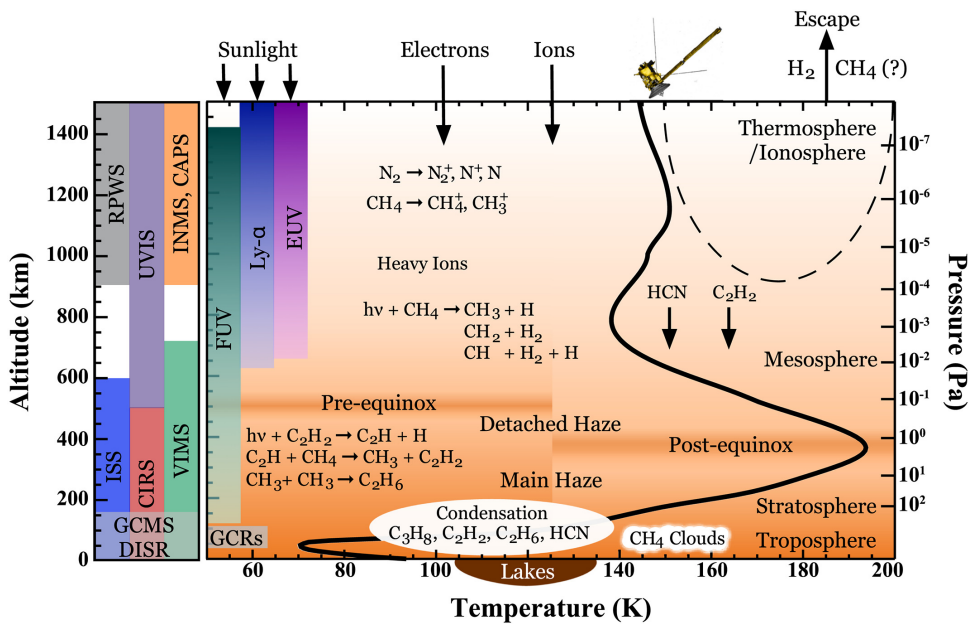


FIG. 1.4 – Shown is the temperature vs altitude/pressure profile of Titan’s atmosphere. The major chemical processes are annotated on the main figure, and the altitude coverage by the Cassini instruments is shown on the left hand side. Image source: [Hörst \(2017\)](#)

and benzene ( $C_6H_6$ ), suggesting pathways for forming larger molecules through polymerisation and aggregation (Desai et al. 2017; Hörst 2017; Nixon 2024). These larger molecules are found further down in the atmosphere as haze particles. Laboratory simulations of Titan’s atmospheric chemistry have successfully reproduced similar organic aerosols, often referred to as tholins, which are complex, tar-like compounds formed through ultraviolet (UV) driven chemistry (Sagan & Khare 1979). Tholins are thought to play a crucial role in haze formation. (Imanaka et al. 2004; Desai et al. 2017).

Titan’s organic-rich environment makes it one of the most compelling targets for studying prebiotic chemistry. The detection of oxygen-bearing molecules, such as CO and  $CO_2$ , along with complex hydrocarbons, suggests that Titan’s atmospheric chemistry may produce molecules of astrobiological interest (Hörst 2017; Nixon 2024). The interaction between the atmosphere and surface further contributes to this complexity, with organic material from the atmosphere being deposited and redistributed by aeolian and fluvial processes, forming extensive dune fields and liquid hydrocarbon reservoirs, see figure 1.2 (Lunine 1998; Hörst 2017).

Titan’s atmosphere provides a compelling analogue to early Earth’s prebiotic environment (Zahnle et al. 2010). Much like the young Earth, Titan features a predominantly nitrogen atmosphere with little to no free oxygen, creating a reducing (i.e. oxygen-poor) chemical setting (Trainer 2013). In such anoxic conditions, methane molecules

broken apart by solar ultraviolet light react with nitrogen fragments to form a cascade of complex organic molecules. This uninterrupted progression of chemistry, without oxidation halting the reactions, makes Titan an atmospheric laboratory for exploring how complex organics may form in early Earth analogue environments. Similar reactions on early Earth are thought to have produced life's building blocks: amino acids and nucleobases ([Zahnle et al. 2010](#); [Trainer 2013](#)).

Because of these chemical parallels, Titan provides a unique opportunity to study how organic molecules form and evolve under prebiotic conditions. In particular, the role of PAHs in Titan's upper atmosphere remains poorly understood ([Hörst 2017](#)). Yet these molecules may form a crucial link in the chain of reactions that drive molecular complexity and haze formation in Titan's atmosphere ([Imanaka et al. 2004](#); [Schulz et al. 2021](#); [López-Puertas et al. 2013](#)). Studying PAHs on Titan can therefore shed light on how prebiotic molecules may have formed on early Earth ([Sandford et al. 2020](#)). Despite their likely importance, the distribution and role of PAHs remain loosely constrained by current models and observations ([López-Puertas et al. 2013](#)). In the next section, we focus on PAHs: how they form, how they are detected, and why they matter.

## 1.2 Polycyclic Aromatic Hydrocarbons (PAHs)

PAHs are complex organic molecules composed of fused rings, consisting of hydrocarbons. Their structure is aromatic with delocalized  $\pi$ -electrons forming a continuous electron cloud above and below the molecular plane, see Figure 1.5. The  $\pi$ -orbitals stabilise the aromatic molecules. PAHs can range in size from a few aromatic rings to large structures with hundreds of carbon atoms. They may also incorporate other species such as nitrogen atoms, forming polycyclic aromatic nitrogen heterocycles (PANHs).

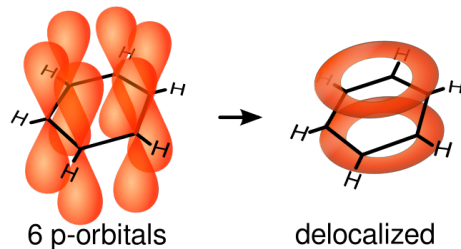


FIG. 1.5 – P-orbitals of a benzene ( $C_6H_6$ ) molecule are delocalized into  $\pi$ -orbitals to form an aromatic molecule. Image source: [Vladsginer](#)

On Earth, PAHs are commonly produced as byproducts of incomplete combustion, contributing to soot and atmospheric pollution ([Balmer et al. 2019](#); [Kaiser & Hansen](#)

2021). In astrophysical environments, however, PAHs are thought to play a key role in carbon chemistry and interstellar processes. The presence of PAHs in space was first inferred through the observation of strong mid-infrared emission features (Gillett et al. 1973). These features were termed the Unidentified Infrared Bands (UIBs) and later referred to as the Aromatic Infrared Bands (AIBs). Their carriers remained unidentified until Leger & Puget (1984) and Allamandola et al. (1985) proposed that these features originate from the vibrational relaxation of interstellar PAHs, introducing what is now widely known as the PAH hypothesis (Allamandola et al. 1989). PAHs are estimated to contain up to 20% of the total cosmic carbon budget (Candian et al. 2018), and have been implicated in prebiotic pathways, including amino acid formation (Sandford et al. 2020).

PAHs are widespread in various astrophysical settings. They are prominently found in: star-forming regions and interstellar clouds or medium, circumstellar envelopes around aging stars, (proto)planetary disks, reflection nebulae, HII regions, and even (exo)planetary atmospheres (Allamandola et al. 1989; Tielens 2008). The spectral fingerprints of PAHs arise from their unique vibrational modes, dominated by carbon-hydrogen (C–H) and carbon-carbon (C–C) stretching and bending motions (Tielens 2008). The C-H stretching is illustrated in Figure 1.6, where we can see the 6 ways carbon and hydrogens stretch in a carbohydrate such as PAHs. These vibrational modes are molecule-specific but follow general patterns, falling into three main categories: symmetric and asymmetric stretching, and bending Mackie et al. (2015). The features are shared across all PAHs regardless of size and make PAHs powerful tracers of carbonaceous material in space. We explain the how the IR features form in the following section.

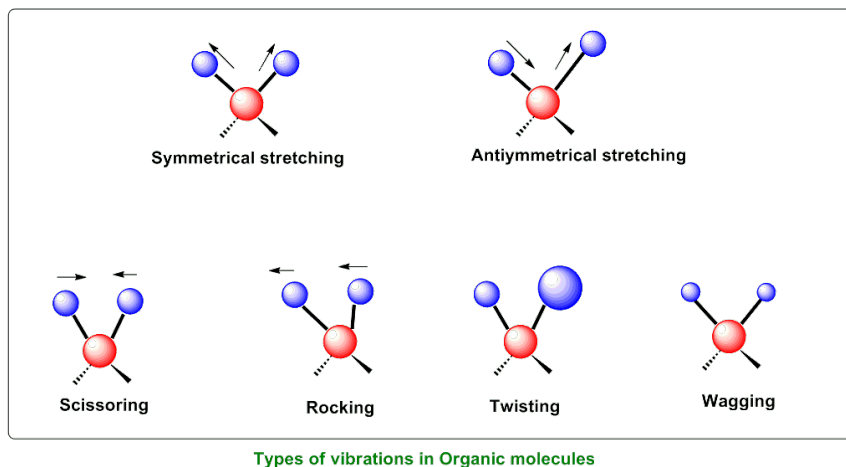


FIG. 1.6 – The vibrational modes of C-H bonds in organic molecules such as PAHs. The modes can: symmetric/asymmetric stretch and bend in the molecule plane, and twist & wag out-of-plane for the C-H stretch. Figure from [legendshub.com](http://legendshub.com).

### 1.2.1 PAH features

PAHs produce their characteristic mid-infrared emission through a fluorescence process initiated by UV photons. When a PAH molecule absorbs a UV photon, it becomes electronically excited and rapidly relaxes by redistributing the energy into its vibrational modes, see Figure 1.6 for the C-H stretch. The molecule then emits this excess energy as IR photons at specific wavelengths corresponding to its vibrational transitions. A simple schematic of the internal process is shown in Figure 1.7.

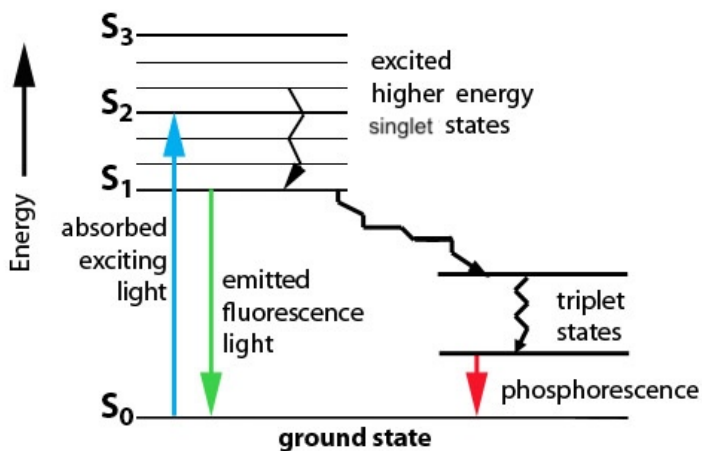


FIG. 1.7 – Simplified Jablonski diagram of PAH fluorescence. A UV photon excites the molecule from the ground singlet state ( $S_0$ ) to a higher singlet state ( $S_n$ ). The energy is quickly redistributed through internal conversion and vibrational relaxation to the lowest excited state ( $S_1$ ). Fluorescence happens when infrared photons are then emitted as the molecule returns to  $S_0$ . Each electronic state includes multiple vibrational levels that enable this stepwise decay. Occasionally the molecule crosses to a triplet state ( $T_1$ ) with unpaired electron spins and cause phosphorescence. Image adapted from Li et al. (2018)

These IR features appear at well-defined wavelengths, most prominently at 3.3, 6.2, 7.7, 8.6, 11.2, 12.7, and 16.4  $\mu\text{m}$ , and are observed in many astrophysical environments (Allamandola et al. 1989; Tielens 2008; Candian et al. 2018). Figure 1.8 shows a typical PAH emission spectrum with these characteristic peaks observed in the Orion Bar by JWST. The feature at 3.3  $\mu\text{m}$  comes from the C-H stretching mode showing in figure 1.6. However, because vibrational modes are shared across the PAH family, IR emission alone does not uniquely identify individual PAH molecules but rather a degenerate set of possible PAHs.

To simulate this emission, two key physical ingredients are needed: the vibrational frequencies and intensities per PAH, and the photon absorption cross-section. In this work the first is obtained from the NASA Ames PAH IR Spectroscopic Database<sup>1</sup>, a database hosted by NASA Ames Research Center that provides quantum-chemically

<sup>1</sup><https://www.astrochemistry.org/pahdb/>

computed and laboratory-measured infrared spectra of PAH molecules (neutral and ionized), along with analysis tools to generate synthetic emission spectra under astrophysical excitation conditions. The photon absorption cross-section is taken from experiments performed by [Mattiola et al. \(2008\)](#) and will be explained further in section 2.

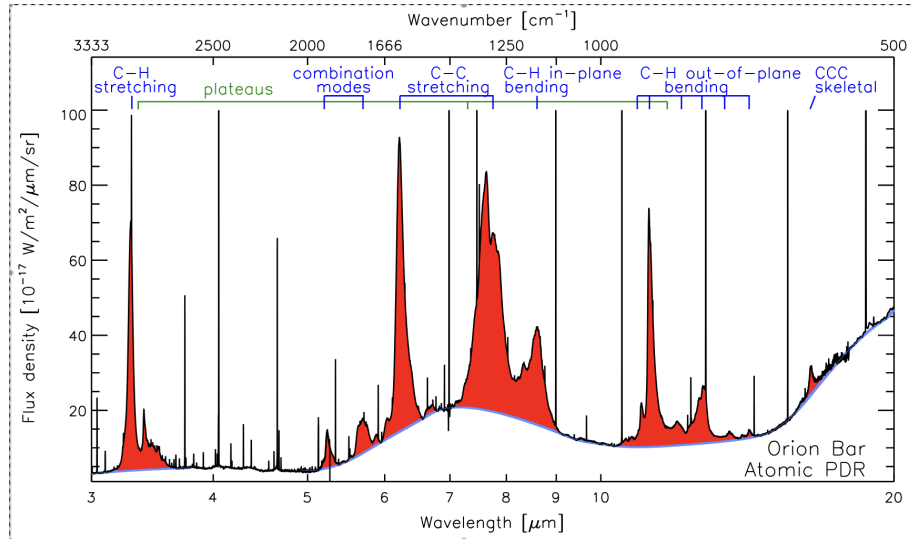


FIG. 1.8 – AIB Orion Bar atomic PDR template spectrum as seen by JWST. Red shaded regions from AIB’s while the blue curve indicates the underlying continuum. Figure from [Chown et al. \(2024\)](#).

### 1.2.2 Formation of PAHs in Titan’s Atmosphere

Polycyclic aromatic hydrocarbons (PAHs) are commonly found throughout many places in the universe. Possibly also in planetary atmospheres such as Titan’s thick organic haze ([Dinelli et al. 2013; López-Puertas et al. 2013](#)). PAH presence in such diverse environments suggests multiple formation pathways that depend on temperature, radiation, and chemical composition in the environment they form. So if PAHs were present on Titan, we need to know how exactly they would form. Titan has a cold upper atmosphere (150–200 K), low pressures, and rich nitrogen–methane chemistry. Thus PAH formation likely occurs through low-temperature, barrierless reactions. The most relevant mechanisms are:

- **HAVA (hydrogen abstraction–vinylacetylene addition):** This low-temperature, barrierless mechanism adds entire six-carbon rings like benzene ( $C_6H_6$ ) via reactions with vinylacetylene ( $C_4H_4$ ). The mechanism proceeds efficiently under Titan-like conditions and possibly dominates PAH growth in Titan’s upper atmosphere ([Zhao et al. 2018; Kaiser & Hansen 2021; Nixon 2024](#)).

- **Ion–Neutral Chemistry:** Titan’s ionosphere is rich in long-lived ions and radicals. Reactions between charged and neutral species, such as benzene cations with unsaturated hydrocarbons, can rapidly form larger aromatic molecules without activation barriers. These processes are believed to be a major contributor to PAH formation on Titan ([Vuitton et al. 2007](#); [López-Puertas et al. 2013](#); [Westlake et al. 2014](#); [Desai et al. 2017](#)).
- **MACA (methylidene addition–cyclization aromatization):** The low-T, barrierless MACA mechanism enables the conversion of vinyl-type side chains into five-membered rings, like indene ( $C_9H_8$ ), which can integrate into larger aromatic structures. Though less dominant than ring-building HAVA and ion–molecule processes, MACA contributes to structural diversity in PAHs and PAHNs in Titan’s cold conditions ([Nixon 2024](#); [Kaiser & Hansen 2021](#)).
- **HACA (Hydrogen Abstraction– $C_2H_2$  Addition):** In this high-temperature pathway, PAHs grow by reacting with acetylene after hydrogen atoms are abstracted. While efficient in combustion or stellar environments, HACA may still play a minor role at high altitudes on Titan, where energetic particles or UV radiation can trigger radical chemistry ([Vuitton et al. 2008](#); [Hörst 2017](#)).

Other mechanisms such as phenyl addition (PAC) and radical–radical recombination (RRR) have been proposed in various high temperature astrophysical contexts ([Nixon 2024](#)). However, they are less likely to dominate under Titan’s cold atmospheric conditions. A summary of the most prominent formation mechanisms in Titan’s atmosphere is in table 1.1, and for any further information that is outside the scope of this thesis we direct the reader to [Kaiser & Hansen \(2021\)](#) and [Nixon \(2024\)](#).

Mechanism	Key Reactants	Barrier	Relevance to Titan
HAVA	$C_4H_4 + PAHs$	None	High
Ion–Neutral	Ions + hydrocarbons	None	High
MACA	$CH +$ vinyl/aromatic chains	None	Moderate
HACA	$C_2H_2$ , aromatic radicals	Low (5–30 kJ/mol)	Limited

TABLE 1.1 Relevant PAH formation mechanisms under Titan conditions. Based on ([Vuitton et al. 2007](#); [López-Puertas et al. 2013](#); [Zhao et al. 2018](#); [Kaiser & Hansen 2021](#); [Nixon 2024](#))

### 1.2.3 PAHs on Titan

Many observations have already been made of Titan with the Cassini/Huygens mission. Visual and Infrared Mapping Spectrometer (VIMS), which took the image in figure 1.2. The altitude coverage of VIMS is also shown on the left hand side of figure 1.4, but the range actually extends further to the upper atmosphere. Observations of Titan’s upper atmosphere with VIMS revealed an unidentified infrared emission

near  $3.28 \mu\text{m}$ , first reported by García-Comas et al. (2011) and Dinelli et al. (2013). This emission was found hidden beneath a methane ( $\text{CH}_4$ ) branch, peaking around 950 km in amplitude and extending from 600 to 1250 km in altitude (Dinelli et al. 2013, Figure 1,2, and 3). The feature is strongly excited by solar radiation, as it vanishes during Titan's night, ruling out thermal emission as its source. The aromatic C-H stretching mode discussed in section 1.2.1 explain the signal best (Dinelli et al. 2013, Figure 4). The emission signal is shown in figure 1.9a where we can see the emission peak at  $3.28 \mu\text{m}$  for 900, 950 and 1000 km.

The emission found by Dinelli et al. (2013) is unexplained by other known atmospheric species, and was proposed to be caused by polycyclic aromatic hydrocarbons (PAHs) (Dinelli et al. 2013). Subsequent analyses by López-Puertas et al. (2013) provided strong evidence that the  $3.28 \mu\text{m}$  feature is linked to polycyclic aromatic hydrocarbons (PAHs). López-Puertas et al. (2013) analysed these features at 900, 950, and 1000 km where the signal was the strongest, see figure 1.9a. They used the NASA Ames PAH IR Spectroscopic Database version 1.20<sup>2</sup> in combination with a cascade excitation model to reproduce its spectral shape and altitude distribution Bauschlicher et al. (2010). Through non-negative least squares (NNLS) fitting, they estimated the PAH population responsible for the observed signal and derived an altitude-dependent abundance profile (López-Puertas et al. 2013, Figure 4 and 5). The derived possible PAH population in Titan's upper atmosphere was found to be substantial, with concentrations of  $(2\text{--}3) \times 10^4 \text{ particles cm}^{-3}$ , containing molecules ranging from 9 to 96 carbon atoms, with an average of 34 carbons per PAH and 10–11 rings on average per molecule. The derived PAH density profile in Titan's upper atmosphere is shown in figure 1.9b.

Additional evidence for the presence of PAHs and their precursors in Titan's upper atmosphere comes from in situ mass spectrometry with other Cassini instruments. The Ion and Neutral Mass Spectrometer (INMS) and the Cassini Plasma Spectrometer (CAPS) detected complex organic molecules at altitudes overlapping with the VIMS observations. These include benzene ( $\text{C}_6\text{H}_6$ ) (Waite et al. 2007; Vuitton et al. 2008) (Figure 1.9b), heavy positive ions up to 300 amu (Haythornthwaite et al. 2021), and a distinct population of large, negatively charged ions interpreted as PAH anions and tholins starting from 50 amu and reaching beyond 10,000 amu measured at 950 km in the ionosphere (Coates et al. 2007; Crary et al. 2009) (Figure 1.9b). From the observations analysed by Crary et al. (2009) aromatic hydrocarbons seem to be the most likely candidates to explain the mass spectrometry peaks, and not any other compounds. The vertical coincidence of these species with the  $3.28 \mu\text{m}$  emission observed by Dinelli et al. (2013), along with their molecular mass patterns, reinforces the hypothesis that PAHs are actively formed and processed in Titan's thermosphere and possible contribute to the haze layer formation (Hörst 2017).

The identification of PAHs in Titan's thermosphere is significant for two main reasons,

<sup>2</sup><https://www.astrochemistry.org/pahdb/theoretical/1.20/default/versions>

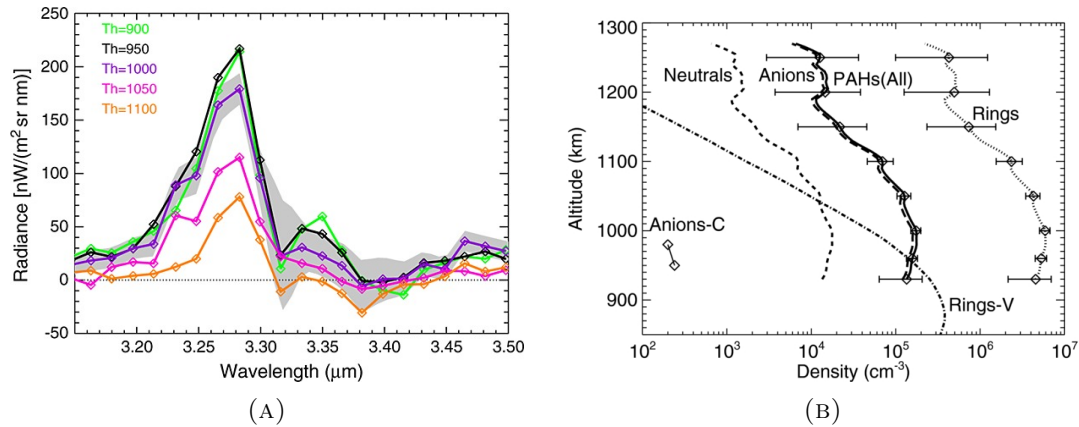


FIG. 1.9 – Detection of possible PAHs in Titan’s atmosphere. left panel: Residual emission spectra at different tangent heights (Th=900–1100 km), showing a clear Unidentified Emission feature near  $\lambda = 3.28 \mu\text{m}$  (peak radiance  $\approx 200 \text{nW}/(\text{m}^2 \text{ sr nm})$ ), with the purple curve (Th=1000 km) highlighted by the gray shaded area indicating estimated uncertainties due to instrument noise and CH<sub>4</sub> abundance retrieval errors (Dinelli et al. 2013). Right panel: Vertical density profiles of PAHs in Titan’s upper atmosphere (altitude 900–1300 km), assuming a mix of neutrals and negative ions. The solid curve shows the total PAH number density; short-dashed and long-dashed lines indicate the neutral and anionic fractions, respectively. The dot-dashed line (“Rings (V)”) represents modelled density of heavy aromatic ring-structures (Vuitton et al. 2008). Diamond symbols (“Anion-C”) mark CAPS-measured concentrations of negative ions Coates et al. (2007).

as discussed in section 1.1. First, PAHs are possible haze precursors (Nixon 2024), supporting the hypothesis that Titan’s thick organic haze layers originate at high altitudes and descend towards the lower atmosphere. Second, PAHs play a crucial role in planetary organic chemistry and may serve as key intermediates in the formation of prebiotic molecules (Sandford et al. 2020). The detection of benzene (C<sub>6</sub>H<sub>6</sub>) and heavier aromatic species in Titan’s atmosphere further suggests a progression toward larger, more complex organic structures (López-Puertas et al. 2013), see figure 1.4 at 900 km.

This research aims to improve on the methods employed by López-Puertas et al. (2013), and constrain the PAH population in the upper atmosphere more using v3.20 of the NASA Ames PAHdb and improved fitting methods, which will be explained in the following section.

# Chapter 2

## Methods

To investigate the presence and distribution of PAHs in Titan’s upper atmosphere, we developed a multi-stage analysis pipeline. First, we received Cassini/VIMS spectra from prior work in which CH<sub>4</sub> contributions had already been subtracted using non-local thermal equilibrium (NLTE) modeling by [García-Comas et al. \(2011\)](#) and [Dinelli et al. \(2013\)](#). Next, we simulated PAH emission spectra using version 3.20 of the NASA Ames PAH database adjusted for Titan’s conditions. Then, we fit these PAHs to the preprococed VIMS observations using non-negative fitting methods. Finally, we analyzed the fitting results to evaluate the fit quality, estimate PAH abundances, and extract distributions of PAH ring sizes.

### 2.1 Preliminary Data Preparation

#### 2.1.1 Cassini/Huygens VIMS data

Cassini’s Visual and Infrared Mapping Spectrometer (VIMS) is an imaging spectrometer that collects spectral cubes up to 64 × 64 spatial pixels, each with 352 wavelengths across the 0.35–5.2 μm range ([Brown et al. 2004](#)). It includes a visible (VIS: 0.35–1.08 μm) and infrared (IR: 0.85–5.2 μm) channel, with angular resolutions of 0.17 × 0.17 mrad and 0.25 × 0.5 mrad, respectively. The IR channel, used in this study, has a spectral resolution of 16 nm and enables vertical resolutions of 22–37 km for Titan limb observations ([Brown et al. 2004](#)).

For this study, we use daytime limb spectra from Cassini/VIMS flybys T34 (19 July 2007) and T35 (31 August 2007), targeting altitudes between 500 and 1200 km in Titan’s southern hemisphere, see figure 2.1 and table 2.1. These cubes were selected for their long integration times (640 ms), broad latitudinal coverage, phase angles below 60°, and vertical resolution better than 100 km. Which are criteria optimized

for detecting weak CH<sub>4</sub> emission in the upper atmosphere. The data was calibrated using pipeline version RC17, with a noise level of  $\sim 3 \times 10^{-8} \text{ W m}^{-2} \text{ nm}^{-1} \text{ sr}^{-1}$  at 3.3  $\mu\text{m}$ . Wavelengths were calibrated linearly by detector band ( $\lambda = 0.01668 \cdot B + 0.7381 \mu\text{m}$ ), accurate to within 0.1%. Observation geometry was reconstructed with NAIF-SPICE, selecting profiles aligned within 1° of the surface normal. Only daytime data are used, as non-LTE CH<sub>4</sub> emission vanishes under nighttime conditions ([García-Comas et al. 2011](#)).

Encounter/Sequence	Cube	IFOV (km)	Phase angle (°)	Profiles/Geolocations
T34/S32-GLOBMAP003	1563524168	50	60	5: 60°SE, 65°SE, 70°SE, 75°SE, 80°SE
	1563524658	47	60	6: 55°SE, 60°SE, 65°SE, 70°SE, 75°SE, 80°SE
	1563525149	45	60	6: 45°SE, 50°SE, 55°SE, 60°SE, 65°SE, 70°SE
T35/S33-CIRSSTARE001	1567269485	70	26	3: 60°SW, 40°SW, 0°W

TABLE 2.1 Cassini/VIMS limb observation cubes used in this study. All data were taken during daytime in Titan's Southern Hemisphere with 640 ms integration time. Listed are the flyby sequence, VIMS cube ID, instantaneous field of view (IFOV), phase angle, number of profiles analysed, and their corresponding geographic locations([García-Comas et al. 2011](#)). The geographic locations are visualised in figure 2.1.

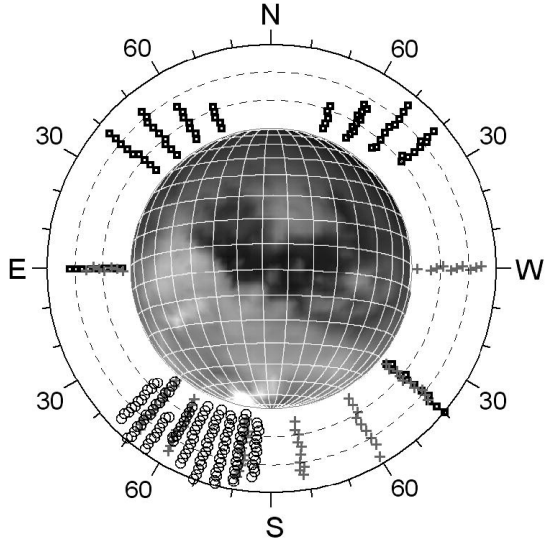


FIG. 2.1 – Geographic locations and tangent altitudes of the VIMS limb observations listed in table 2.1. Each marker corresponds to a vertical profile extracted from the spectral cubes during flybys T34 and T35. The dashed lines indicate tangent altitudes in 500 km intervals ([García-Comas et al. 2011](#)).

### 2.1.2 CH<sub>4</sub> NLTE Model

Titan's upper atmosphere is characterised by low pressures and densities ([Hörst 2017](#); [Nixon 2024](#)), where molecular collisions are too infrequent to maintain local thermodynamic equilibrium (LTE) ([López-Puertas & Taylor 2001](#)). As a result, vibrational

states of molecules like methane ( $\text{CH}_4$ ) deviate from the Boltzmann distribution set by local temperature, especially around  $3.3 \mu\text{m}$ . This non-LTE behaviour complicates the retrieval of temperature and composition from infrared spectra (López-Puertas & Taylor 2001).

To address this, we adopt the  $\text{CH}_4$  non-LTE model of García-Comas et al. (2011), which solves the steady-state populations of 22 vibrational levels by coupling radiative transfer with rate equations. It includes solar pumping,  $\text{N}_2$  collisions, and  $\text{CH}_4$  vibrational–vibrational exchanges, and accurately reproduces Titan’s  $3.3 \mu\text{m}$   $\text{CH}_4$  emission. Using this model to subtract  $\text{CH}_4$  from VIMS limb spectra, Dinelli et al. (2013) revealed a persistent residual at  $3.28 \mu\text{m}$ , peaking near 900, 950, and 1000 = km.

This feature was attributed to polycyclic aromatic hydrocarbons (PAHs) (Dinelli et al. 2013), and modelled as solar-pumped emission using the NASA Ames PAH IR Spectroscopic Database and a cascade emission model (López-Puertas et al. 2013; Bauschlicher et al. 2010). The database provides theoretical and experimental IR spectra of PAHs for astrophysical identification and analysis. Through non-negative least squares (NNLS) fitting, the PAH population and its altitude-dependent profile were estimated, see figure 1.9b.

We build on this approach by expanding NASA Ames PAH IR Spectroscopic Database from version 1.20 to 3.20 and applying improved fitting methods, explained in section 2.3. To use the preprocessed VIMS data with the `NASAAmesPythonSuite`<sup>1</sup>, we convert radiance ( $\text{nW m}^{-2} \text{sr}^{-1} \text{nm}^{-1}$ ) to surface brightness ( $\text{MJy sr}^{-1}$ ) via

$$1 \text{ nW m}^{-2} \text{sr}^{-1} \text{nm}^{-1} = \frac{10^{-9} \times \lambda^2}{c} \times 10^{20} \text{ MJy sr}^{-1},$$

where  $\lambda$  is wavelength in meters and  $c$  is the speed of light. This ensures the spectra are in frequency units as required by the model. Additional selection and normalization procedures were implemented to better constrain the PAH composition and vertical distribution in Titan’s atmosphere. The final spectra for 900, 950 and 1000 km are shown in figure 2.2.

---

<sup>1</sup><https://www.astrochemistry.org/pahdb/>

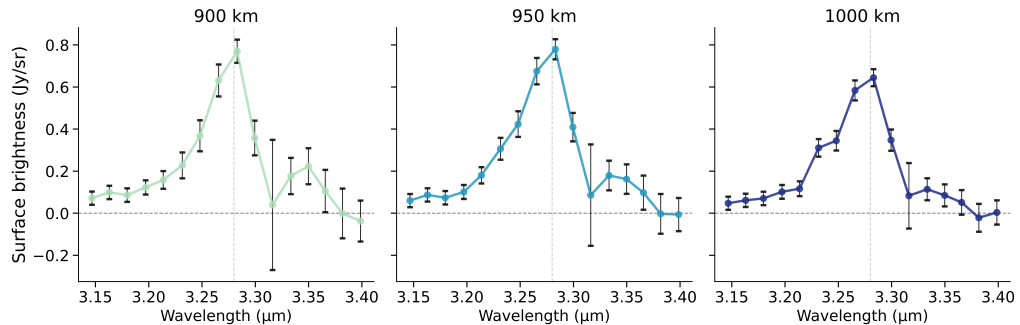


FIG. 2.2 – The three Spectra from the 4 Cassini/VIMS spectral data cubes combined into one signal, at tangent heights of 900, 950, and 1000 km. The unit of radiance is converted to surface brightness, and the spectra are shown around  $3.28 \mu\text{m}$ .

## 2.2 Emission model using the NASA Ames Database

To find out which PAHs give the best possible fit of the spectra, we utilise the NASA Ames PAH IR Spectroscopic Database ([Boersma et al. 2014](#); [Bauschlicher et al. 2018](#); [Mattiola et al. 2020](#)). In the following sections, we explain how the theoretically calculated PAHs are made to look as you would expect them to in Titan’s upper atmosphere. The selected PAHs must be processed to simulate their expected emission in Titan’s upper atmosphere. We begin with the theoretical spectra from the NASA Ames PAH IR Spectroscopic Database, calculated using density functional theory (DFT), which is outside the scope of this thesis to explain but we refer the reader to [Bauschlicher et al. \(2018\)](#) and [Mackie et al. \(2018\)](#) for more information. Each individual vibrational transition is represented as a Dirac an infinitely narrow spike at the calculated line frequency, see figure 4.3a.

### 2.2.1 Cascade Emission Model

To simulate the mid-infrared emission of PAHs excited by solar UV radiation at Titan, we apply the cascade emission model implemented in the `AmesPAHdbPythonSuite` ([Boersma et al. 2014](#)). This model describes the thermal IR emission that results when a PAH molecule absorbs a single UV photon and subsequently cools via a vibrational cascade. We start out with the DFT calculated dirac delta functions, see figure 4.3a.

The cascade model we use convolves the full stellar photon spectrum with each PAH’s absorption cross section and vibrational structure. This provides a physically realistic simulation of the emission process.

**Step 1: Radiation Field** PAHs in Titan’s upper atmosphere are primarily excited by solar photons. We represent the radiation field by a scaled solar spectrum at Titan’s heliocentric distance of 10 AU ([López-Puertas et al. 2013](#)), see section 2.2.2 for more information. Each PAH species has a wavelength-dependent photon absorption cross section  $\sigma_{\text{abs}}(\nu)$ , and the probability of photon absorption at each frequency is given by the product  $\sigma_{\text{abs}}(\nu) \cdot I_*(\nu)$ , where  $I_*(\nu)$  is the specific intensity of the stellar field. The mean absorbed photon energy is computed as:

$$\langle E \rangle = \frac{\int \sigma_{\text{abs}}(\nu) I_*(\nu) h\nu d\nu}{\int \sigma_{\text{abs}}(\nu) I_*(\nu) d\nu} \quad (2.1)$$

This formulation ensures that photon absorption is weighted by both the stellar spectrum and molecular cross section ([Andrews et al. 2015](#)).

**Step 2: Maximum Temperature Determination** Once a photon is absorbed, its energy is redistributed over the PAH’s vibrational modes  $\nu_i$ . The molecule reaches a maximum internal temperature  $T_{\text{max}}$  that satisfies the energy balance:

$$\int_{T_{\text{ini}}}^{T_{\text{max}}} C_v(T) dT = \langle E \rangle \quad (2.2)$$

Here,  $C_v(T)$  is the vibrational heat capacity of the PAH, computed from the normal modes stored in PAHdb, and  $T_{\text{ini}} = 2.73\text{ K}$  is the background temperature. The code solves this integral equation numerically using Brent’s method, a root-finding algorithm that combines bisection, secant, and inverse quadratic interpolation for convergence ([Brent 2013](#)), via the function `Transitions.attained_temperature()`.

**Step 3: Convolved Feature Strength Calculation** The emission from each vibrational mode depends on how long the PAH remains at each temperature during cooling. The temperature probability distribution function  $G(T)$  captures this, derived from the thermal approximation ([Bakes et al. 2001](#)), which assumes exponential cooling. For each vibrational mode  $\nu_i$  at frequency  $f$ , the emitted intensity is:

$$I(f) = \sigma_{\nu_i}(f) \cdot \Phi(f) \cdot \int_{T_{\text{ini}}}^{T_{\text{max}}} B(f, T) G(T) dT \quad (2.3)$$

where,  $\sigma_{\nu_i}$  is the molecular absorption cross section,  $\Phi(f) = I_*(f)/f$  represents the photon number density of the stellar field,  $B(f, T)$  is the Planck function, and  $G(T)$

describes the time the molecule spends at temperature  $T$  during relaxation. We convolve the entire radiation field with `Transitions.stellar_model_feature_strength_convolved()` because we use a real physical solar spectrum.

**Step 4: Energy Conservation and Spectrum Assembly** The code normalises each PAH's emission spectrum such that the total emitted energy equals the absorbed energy. The final intensity spectrum is constructed by summing the contributions of all vibrational modes  $\nu_i$ . For each species, the cascade function outputs the full IR emission spectrum, along with metadata such as maximum attained temperature  $T_{\max}$  and average energy  $\langle E \rangle$ , and stores the result in memory. These spectra serve as input for later spectral fitting to Titan observations. By convolving the stellar photon field with molecular properties, this cascade model captures both the thermal physics of PAH cooling and the spectral distribution of the incident radiation. It becomes a prediction of PAH infrared emission under Titan's UV irradiation conditions.

**Step 5: Band Profiles, FWHM, and Anharmonic Shift** Finally, for any version of the NASA Ames database other than version 4.00, a shift of  $15 \text{ cm}^{-1}$  is implemented to account for anharmonic corrections ([Bauschlicher et al. 2010](#); [Maragkoudakis et al. 2024](#)). Then the results from the cascade emission are convolved with a Lorentzian profile, because we use gas-phase and collisionless PAHs under isolated, lifetime-limited emission, with a FWHM of 15 to broaden the profiles as we would expect to happen in the isolated conditions of the upper atmosphere of Titan ([Tielens 2008](#)). An example what this final signal looks like for UID 527 ( $\text{C}_{10}\text{H}_8\text{N}$ ), is shown in Fig. 4.3b.

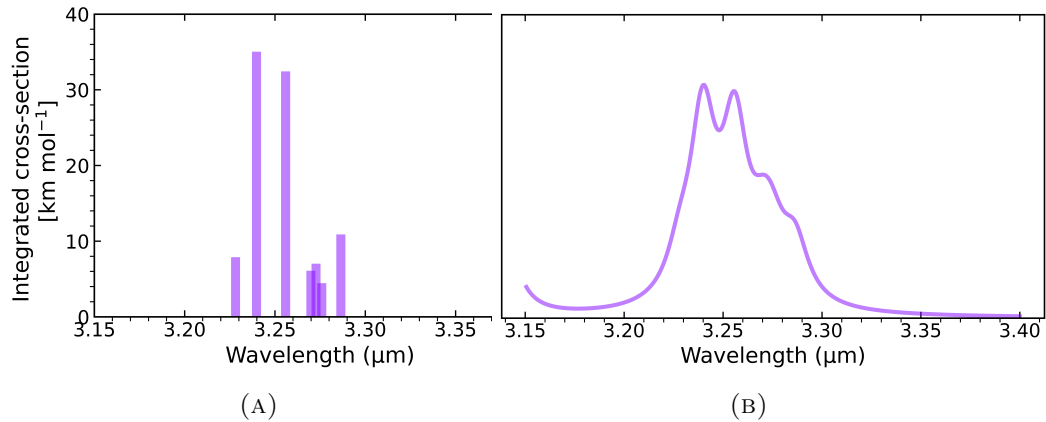


FIG. 2.3 – DFT-calculated spectrum of  $\text{C}_{10}\text{H}_8\text{N}$  UID = 527 from the NASA Ames PAH database around the  $3.28 \mu\text{m}$  feature before (A) and after (B) the cascade emission modelling.

### 2.2.2 Solar Data

To model the cascade emission realistically, we used solar spectral irradiance data from the SORCE mission for the dates of the two Titan flybys: July 19 and August 31, 2007. The SORCE mission took Solar spectra from Earth at 1 AU, thus the data had to be scaled to Titan's distance of 10 AU. Because photon absorption drives PAH excitation, the solar input must remain consistent between flybys.

Figure 2.4 shows that the absolute differences are on the order of  $10^{-5}$  W/m<sup>2</sup>/nm, mostly within the measurement uncertainties of the SORCE data, thus these deviations are not significant. We conclude that the solar input was effectively constant across both dates and proceed using the August 31, 2007 spectrum in all cascade calculations from hereon.

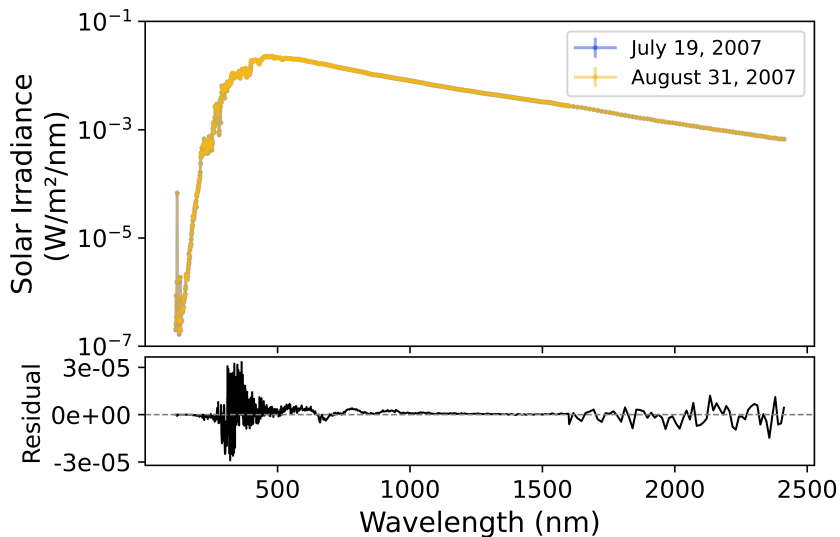


FIG. 2.4 – Comparison of solar flux scaled to Titan's distance (10 AU) used in the cascade model for two dates: July 19, 2007 (blue) and August 31, 2007 (yellow). The upper panel shows the SORCE solar irradiance with associated uncertainties; the lower panel shows the absolute residuals between the two dates. The differences are small (order  $10^{-5}$  W/m<sup>2</sup>/nm), with the largest deviations at shorter wavelengths.

### 2.2.3 Photoabsorption crosssection

PAH molecules can absorb electromagnetic radiation through electronic transitions, and electrons excite into discrete energy states. PAHs absorb in the UV and Visible (Tielens 2008) and Ionized PAHs also absorb in NIR (Mattiolla et al. 2005a). PAHs are highly efficient absorbers of radiation due to their extended conjugated  $\pi$ -orbitals, see figure 1.5. Their photon absorption cross section sets the energy available for infrared emission by how efficiently a PAH absorbs a photon at a certain wavelength.

The absorption cross-section per carbon atom,  $\sigma_{\text{PAH}}(\lambda)$ , is approximated by a combination of UV absorption models ([Li & Draine 2001](#), Eq. 11) and near-IR extensions [Mattiola et al. \(2005a\)](#).

A key parameterization is given by [Li & Draine \(2001\)](#), who describe the PAH absorption cross-section as:

$$\sigma_{\text{PAH}}(\lambda) = 3.5 \times 10^{-19} e^{-1.45\lambda/\mu\text{m}} + S_1 + S_2 - S_3, \quad (2.4)$$

where  $\lambda$  is in micrometres, and  $S_1, S_2$ , and  $S_3$  represents Drude profiles corresponding to specific vibrational and electronic transitions. This equation highlights the strong UV absorption of PAHs, which efficiently absorb high-energy photons and re-radiate in the mid-IR. However, the efficiency of PAH absorption is limited by a size-dependent cutoff as described in [Mattiola et al. \(2005b\)](#). The cutoff equation is:

$$\text{cutoff}(\lambda, \lambda_c) = \frac{1}{\pi} \arctan \left( \frac{10^3 (\lambda_c/\lambda - 1)^3}{\lambda_c/\lambda} \right) + \frac{1}{2}, \quad (2.5)$$

where  $\lambda_c$  is the wavelength at which absorption declines steeply, determined by the PAH molecular size. This function ensures that larger PAHs ( $N_c > 40$ ) absorb effectively at longer wavelengths, while smaller PAHs ( $N_c < 40$ ) exhibit a sharp cutoff in the NIR.

A NIR corrections needs to be added for Ionic PAHs since they absorb radiation in that regime more efficiently than neutral species. The correction is added after the cutoff wavelength and follows from [Mattiola et al. \(2005a\)](#):

$$\sigma_{\text{PAH}}(\lambda) = 1.5 \times 10^{-19-\lambda/\mu\text{m}} + G_1 + G_2 + G_3 + G_4 + G_5 - G_6, \quad (2.6)$$

where the first term is a continuous baseline that drops with increasing wavelength and the additional terms describe gaussian bands peaking between 0.8 to 2.4  $\mu\text{m}$  ([Mattiola et al. 2005a](#), Figure 1, table1)

Figure 2.5 illustrates the absorption efficiency across the UV-NIR range for neutral PAHs in the grey dashed line ([Li & Draine 2001](#)). The full photon absorption cross section with the NIR correction for ionic PAHs is shown in the solid grey line ([Mattiola et al. 2005a](#)). The blue line is our addition and is explained in section 2.2.4.

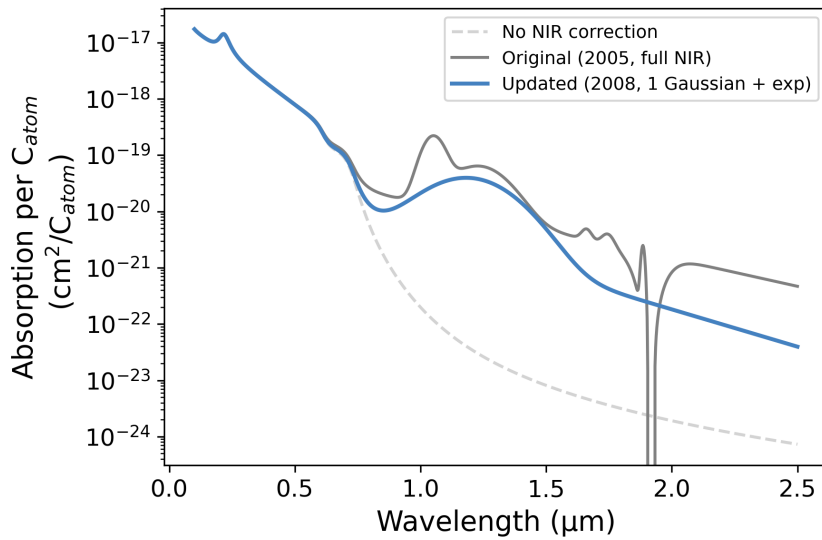


FIG. 2.5 – Photon absorption cross section per carbon atom for a PAH with  $N_C = 34$ , the average size found by Lópe-Puertas et al. (2013), assuming a non-zero charge. The dashed gray line shows the uncorrected model from Li & Draine (2001) and Mattioda et al. (2005a), without any near-infrared (NIR) correction. The solid gray curve includes the original NASA Ames NIR correction. The blue curve shows our updated parameterization using a single Gaussian and exponential tail, based on the revised laboratory data from Mattioda et al. (2008).

#### 2.2.4 Content & Constraints

We fit the spectra at 900, 950, and 1000 km using cascade-modelled PAH emission from version 3.20 of the NASA Ames PAH IR Spectroscopic Database (Boersma et al. 2014; Bauschlicher et al. 2018; Mattioda et al. 2020). This version contains over 4000 computed species and 84 experimental PAHs. Following the approach of Lópe-Puertas et al. (2013), we select only neutral species containing carbon, hydrogen, and nitrogen, excluding those with magnesium, iron, silicon, or oxygen.

We extend this selection with two additional filters. First, we remove all fully dehydrogenated PAHs ( $H = 0$ ), which do not produce emission at  $3.28 \mu\text{m}$  due to the absence of C-H bonds (Mallochi et al. 2008; Mackie et al. 2015). Second, we allow for anionic species (negatively charged ions), as they have been detected in Titan's ionosphere (Coates et al. 2007). Although cations (positive ions) have also been identified (Haythornthwaite et al. 2021), their  $3.28 \mu\text{m}$  band is an order of magnitude weaker than that of neutrals and anions (Lópe-Puertas et al. 2013, Fig. 2a), and are therefore excluded from the fit. After applying these criteria, we retain 2632 PAHs.

Although the core functionality is based on the open-source NASA Ames PAHdb Python-Suite, several key modules included bugs or lacked features critical for our cascade and fitting workflows. We incorporated two improvements into the NASA Ames

fitting process:

**The Photon absorption cross section.** we adjust the calculations discussed in section 2.2.3. In the original model used by the NASA Ames PAHdb, the near-infrared (NIR) cross section was based on outdated experimental data ([Li & Draine 2001](#); [Mattiola et al. 2005b](#)) and applied only to neutral PAHs by [López-Puertas et al. \(2013\)](#). However, since our fits include both neutral and anionic species, we must use a photon absorption cross section that reflects their true absorption behaviour. We therefore updated the Near Infrared (NIR) correction following [Mattiola et al. \(2008\)](#), which provides improved measurements and a revised parameterization of the NIR continuum for charged PAHs with the equation:

$$\sigma_{\text{PAH}}(\lambda) = 1.4 \times 10^{-19.2 - 1.34\lambda/\mu\text{m}} + G_1, \quad (2.7)$$

Where the NIR correction is now described by a single Gaussian instead of the 6 parameters in equation 2.6. The blue line in Figure 2.5 show the change, with the NIR correction now being in line with the most recent research ([Mattiola et al. 2008](#), Table 3, Figure 9, 10). This correction ensures our model captures the physical properties of the ionic PAH population more accurately.

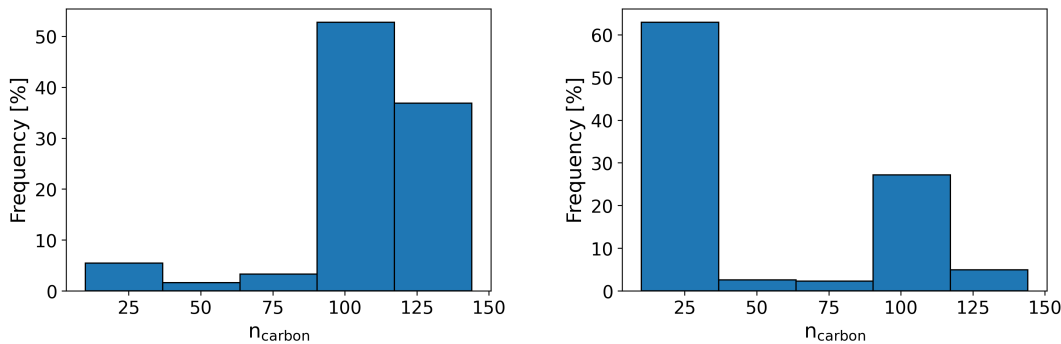


FIG. 2.6 – Frequency distribution of dominant PAHs by carbon count ( $n_{\text{carbon}}$ ) in the final fit. The left panel shows results from an NNLC fit using database-wide normalisation, which biases toward large PAHs. The right panel shows results after normalising each PAH individually to unity, reducing size bias and recovering smaller PAHs.

**Normalisation per PAH.** The default normalisation method from the NASA Ames PAHdb scales all spectra by the maximum flux across the database. This approach introduces a strong bias toward large PAHs, which naturally emit more strongly due to having more C–H bonds ([Li & Draine 2001](#); [Berné & Joblin 2019](#)). As a result, these molecules dominate the fit even when their spectral shapes are a poor match simply because of their higher amplitude. To correct this, we normalised each PAH spectrum individually to unit flux. This per-PAH normalisation removes

amplitude bias and ensures that the fit prioritises spectral shape over intensity. Figure 2.6 illustrates the visual impact of this adjustment on the fit and component breakdown, showing that larger PAHs now longer dominate the fit when normalised to unity.

## 2.3 Spectral Fitting

Next we need to compare the PAH cascade emission models to the VIMS spectra and assess how well they fit, using the tools provided in the `AmesPAHdbPythonSuite`<sup>2</sup>. For this we use two non-negative fitting routines: NNLS & NNLC for a single fit. And then to assess statistics and error margins on the derived values we apply a Monte Carlo fit for 1000 runs and apply NNLS.

### 2.3.1 NNLS

To quantify the contribution of PAHs to Titan’s  $3.28\text{ }\mu\text{m}$  emission, López-Puertas et al. (2013) did non-negative least squares (NNLS) fitting to match observed spectra with cascade-modeled PAH templates from the NASA Ames PAH IR Spectroscopic Database (Boersma et al. 2014; Bauschlicher et al. 2018; Mattioda et al. 2020). NNLS minimizes the squared residual between the observed spectrum  $\mathbf{y}$  and a non-negative linear combination of  $N$  model spectra  $\mathbf{x}_i$ :

$$\min_{\mathbf{a} \geq 0} \left\| \mathbf{y} - \sum_{i=1}^N a_i \mathbf{x}_i \right\|_2^2, \quad (2.8)$$

where each coefficient  $a_i$  reflects the relative contribution of PAH  $i$ . This method ensures physical consistency by excluding negative emission and allows efficient spectral decomposition across large molecule sets (Bro & Jong 1997; Rosenberg et al. 2011). As emphasized by López-Puertas et al. (2013), NNLS fitting reveals the statistical makeup of the emitting PAH population but does not identify individual molecules. Instead the method traces population or PAH size (Boersma et al. 2010), (Boersma et al. 2011). Most importantly, this method does not include the error margins on the datapoints, and weights them all equally. This is an issue when the error bars differ per point.

---

<sup>2</sup><https://pahdb.github.io/AmesPAHdbPythonSuite/>

### 2.3.2 NNLC

While NNLS treats all data points equally, the signal-to-noise ratio in the spectra varies significantly and some datapoints have large errors making these less reliable, see figure 2.2. To account for this, we implement non-negative least chi-square (NNLC) fitting ([Désesquelles et al. 2009](#)), which generalizes NNLS by weighting the residuals by the inverse of their uncertainties:

$$\chi^2 = \sum_i \frac{(y_i - \sum_j a_j x_{ij})^2}{\sigma_i^2}, \quad (2.9)$$

where  $y_i$  is the observed flux in spectral channel  $i$ ,  $\sigma_i$  its associated uncertainty, and  $x_{ij}$  the model value from PAH  $j$  at channel  $i$ . As in NNLS, the fit solves for non-negative coefficients  $a_j$ , using the same iterative algorithm shown in Equation 2.8. The only difference is that the input spectrum is scaled by its error margins. This weighting improves fitting by emphasizing the most reliable parts of the spectrum by reducing the influence of noisy data points ([Désesquelles et al. 2009](#)). However, a single fit of the +2600 PAHs on the 16 datapoints per height is not enough to track trends in frequency and sizes of PAHs. Most importantly we are unable to calculate statics and error margins on these values.

### 2.3.3 Monte Carlo error Propagation

To quantify uncertainties in the fitted PAH populations, we apply a Monte Carlo (MC) error propagation technique following [Maragkoudakis et al. \(2022\)](#) and [López-Puertas et al. \(2013\)](#). The datapoints of the VIMS spectra are varied within their error margins randomly following a normal distribution. Each random variation procures a new perturbed spectrum of the ones shown in figure 2.2. Each perturbed spectrum is independently fitted using NNLS, producing a distribution of coefficients for PAH abundance across iterations. From this ensemble, we derive the mean, standard deviation, and skewness of key PAH properties applying inverse-variance weighting to account for fit uncertainty, more is explained in section 2.4. This approach transforms measurement noise into interpretable uncertainty on PAH population characteristics. It supports robust statistical comparisons across altitudes or spectral subsets, and provides reliable error estimates in a degenerate, underdetermined regime of +2600 PAHs on 16 datapoints.

## 2.4 Post-Fit Evaluation and Diagnostics

Like [Maragkoudakis et al. \(2022\)](#), we fit Gaussian models to the output distributions and report both the empirical and model-derived statistics.

### 2.4.1 Goodness-of-Fit Assessment

To evaluate the quality of the NNLS and NNLC fits, we compute the reduced  $\chi^2$  statistic:

$$\chi_{\nu}^2 = \frac{1}{\nu} \sum_{i=1}^n \left( \frac{y_i - f_i}{\sigma_i} \right)^2, \quad (2.10)$$

where  $y_i$  is the observed flux,  $f_i$  the model flux,  $\sigma_i$  the uncertainty in channel  $i$ , and  $\nu = n - p$  the degrees of freedom. Here,  $n = 16$  and  $p =$  number of PAHs per NNLS/NNLC fits. The number of PAHs in the fit can vary between the fits and therefore gives a different degrees of freedom each time. This is also the reason why we calculate the reduced version of the  $\chi^2$ . This metric weights residuals by uncertainty and normalizes by complexity, allowing direct comparison between fits and how good they are. Values near  $\chi^2 = 1$  indicate consistency with the noise, while higher/lower values suggest poor fits or underestimated errors.

In the Monte Carlo runs, each perturbed spectrum is fitted using NNLS, which does not use uncertainties in the optimization. We still compute  $\chi_{\nu}^2$  for each fit to assess its plausibility and identify outliers. Though NNLS does not minimize this statistic, it remains a robust, interpretable measure across the ensemble and see how well the model fits the data ([Désesquelles et al. 2009](#); [Dieck 2007](#)).

### 2.4.2 Estimating PAH Occurrence

Each NNLS/NNLC fit includes 6–14 PAHs, each contributing a fraction of the total model flux. These fractions sum to 100%, so the fit represents a weighted composition. Aggregating results across the Monte Carlo ensemble reveals consistent patterns and highlights PAHs that dominate the observed spectrum. Diagnostic plots summarize each fit. The first compares model, data, and residuals, showing where the fit succeeds or fails. The second decomposes the total signal into contributions from individual PAHs. Additional plots group contributions by chemistry (pure vs. nitrogen-containing), by size (small, medium, large), and, when applicable, by charge state (neutral, anion, cation). A final histogram of carbon atom counts ( $N_C$ ) gives

the size distribution. Figure 2.6 illustrates these outputs. Ensemble plots further show the mean fit and its  $1\sigma$  spread.

### Concentration-Weighted PAH Counts

To estimate the prevalence of each PAH species, we integrate each PAH contribution to the fits across the full Monte Carlo ensemble. Each iteration yields a non-negative coefficient  $a_{ij}$  for PAH  $j$ , representing its relative contribution to the  $n$  number of fits. Summing over all 1000 iterations produces a concentration-weighted count  $C_j = \sum_i a_{ij}$ , which captures both the frequency and strength of a PAH's contribution. This approach provides a quantitative ranking of PAHs that consistently shape the emission spectrum and enables comparisons across altitudes or spectral regimes. However, due to spectral degeneracies in the  $3.3 \mu\text{m}$  region (Boersma et al. 2011), the method is better suited for tracking population-level trends than for identifying individual species.

### PAH Ring Sizes

Even though we are not able to confirm the existence of specific PAHs with the above written method we can assess structural trends of the PAHs such as ring size. Since the emission of PAHs in the region of  $3.28 \mu\text{m}$  is proportional to the amount of C-H bonds, it is thus proportional to the total number of rings (Boersma et al. 2010, 2011). We analyze the distribution of PAH ring sizes across the Monte Carlo ensemble. A PAH ring consists out of 5 or 6 carbons. Each fit coefficient is mapped to the ring count of its associated PAH, producing a concentration-weighted distribution of ring sizes. We fit this distribution with a Gaussian and extract the mean, median and standard deviation, providing a statistical summary of the dominant molecular structures. This approach enables comparisons between altitudes or fitting conditions. It also enables comparison with the results of López-Puertas et al. (2013).

The methodology as discussed in sections 2.3 and 2.4 is available in the `Titan_PAHs` GitHub repository<sup>3</sup>. Custom modifications to the `AmesPAHdbPythonSuite`, as discussed in section 2.2.4, are documented and implemented in a forked version of the original repository<sup>4</sup>, using the `feature/norm-per-pah` branch.

---

<sup>3</sup>[https://github.com/STIK98/Titan\\_PAHs](https://github.com/STIK98/Titan_PAHs)

<sup>4</sup>[https://github.com/STIK98/AmesPAHdbPythonSuite\\_forked/tree/feature/norm-per-pah](https://github.com/STIK98/AmesPAHdbPythonSuite_forked/tree/feature/norm-per-pah)

# Chapter 3

## Results

This chapter presents the main findings of this study. We begin by validating our methodology through the reproduction of results from López-Puertas et al. (2013) using version 1.20 of the NASA Ames PAHdb. We then apply updated fitting techniques (Section 2) and database versions 3.20 and 4.00 to refine the identification of PAHs in Titan’s upper atmosphere. To streamline presentation, we focus on the results at 950 km which is representative of the dataset’s vertical range. Full-height fits for 900, 950 and 1000 km and single PAH fits are shown in Appendix A. Height-averaged results are included in this chapter.

### 3.1 Re-analysis of VIMS data

To validate our approach, we replicated the method of López-Puertas et al. (2013) using PAHdb v1.20, which includes 201 neutral PAHs, and performed a non-normalized NNLS fit on CH<sub>4</sub>-subtracted VIMS spectra at 900, 950, and 1000 km. An important difference is that López-Puertas et al. (2013) used the IDL programming whereas we use the Python Suite for the NASA Ames database. López-Puertas et al. (2013) found a concentration-weighted mean size of 34 carbon atoms and a significant fraction of nitrogen-containing PAHs, with the average PAH size being 10-11 rings.

Figure 3.1 shows the NNLS fit at 950 km, with subplots detailing the fitted spectrum, residuals, size distribution, and molecular composition, as explained in section 2.4.2. The fit we emulate with NNLS has a reduced  $\chi^2$  of 2.278, 0.969, and 0.518 for the heights of 900, 950, and 1000 km respectively. This tells us that the fit is in reasonable agreement with the data, see section 2.4.1. Especially at 950 km where  $\chi^2_\nu \approx 1$  indicates a statistically sound fit. The higher value at 900 km suggests that the model underfits the data, failing to fully capture the spectral structure. In contrast, the lower value at 1000 km implies possible overfitting, where the model

may be fitting noise or has too many free parameters, thus PAHs in the fit. Looking at the top left panel of figure 3.1 we see that the residuals are higher at the wings of the signal, especially at the red wing around  $3.35 \mu\text{m}$ . This is also true for 900 and 1000 km, see figures A.1 and A.1.3 in appendix A.

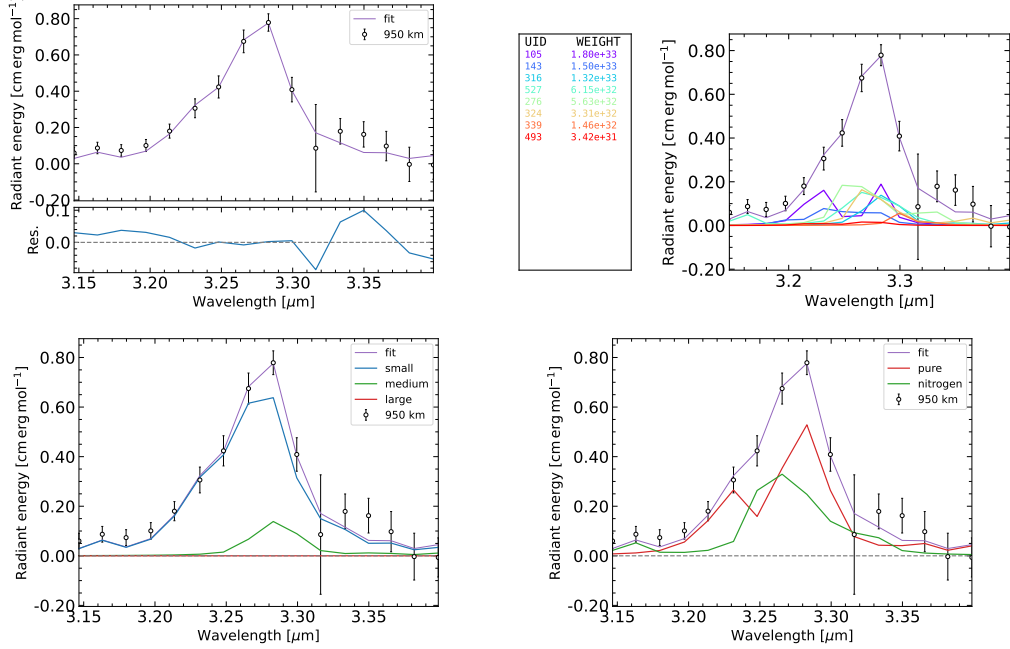


FIG. 3.1 – NNLS fit using PAHdb v1.20 to VIMS observations at 950 km. Top left: observed (black dots) and fitted (purple line) spectra with residuals. Top right: contributions from the eight selected PAH UIDs. The selected PAHs are: UID 493 ( $\text{C}_9\text{H}_7$ ), 527 ( $\text{C}_{10}\text{H}_8\text{N}$ ), 276 ( $\text{C}_{13}\text{H}_9\text{N}$ ), 339 ( $\text{C}_{14}\text{H}_{16}$ ), 324 ( $\text{C}_{15}\text{H}_{12}$ ), 105 ( $\text{C}_{42}\text{H}_{18}$ ), 143 ( $\text{C}_{48}\text{H}_{22}$ ), and 316 ( $\text{C}_{55}\text{H}_{20}$ ). Bottom left: contributions by PAH size class (small, medium, large). Bottom right: composition breakdown into pure PAHs (red) and nitrogen-containing PANHs (green). Wavelength is in  $\mu\text{m}$  and radiant energy in  $\text{cm erg mol}^{-1}$ . The reduced  $\chi^2 = 0.969$ .

The other panels of figure 3.1 and in appendix A show that the fit is dominated by small-sized PAHs ( $N_c < 50$ ), with a small contribution of medium sized PAHs ( $50 < N_c < 70$ ) except for 1000 km which has only small PAHs. There is also a notable contribution from nitrogen-containing species, which at  $3.25 \mu\text{m}$  even seem to overtake the contribution of pure species in figure 3.1. This is also apparent for 900 but not 1000 km, see figures A.1 and A.1.3.

Compared to López-Puertas et al. (2013, fig. 4), our fit shows two key differences with the corresponding panel in Figure 3.1. First, we do not include a “rest” group, which contributes significantly especially at 950 km in their analysis. Our model includes 8-9 individual PAHs, whereas theirs includes only 6 plus a rest component. Second, their fitted spectrum appears smoother, despite being based on just 16 data points.

Nonetheless, the overall agreement is strong. Both fits show underfitting in the red wing, with the poorest performance at 900 km and the best at 1000 km (Figures 3.1, A.1, and A.1.3 top left panels). Several dominant PAHs are shared, including UID 527 ( $C_{10}H_8N$ ), UID 143 ( $C_{48}H_{22}$ ), 493, and 276. However, UID 143 is far less prominent in our fit, and large species such as UID 108 ( $C_{96}H_{24}$ ) and UID 174 ( $C_{84}H_{24}$ ) are absent (Figures 3.1, A.1, and A.1.3 top right panels). Despite these differences, our results broadly align with those of [López-Puertas et al. \(2013\)](#).

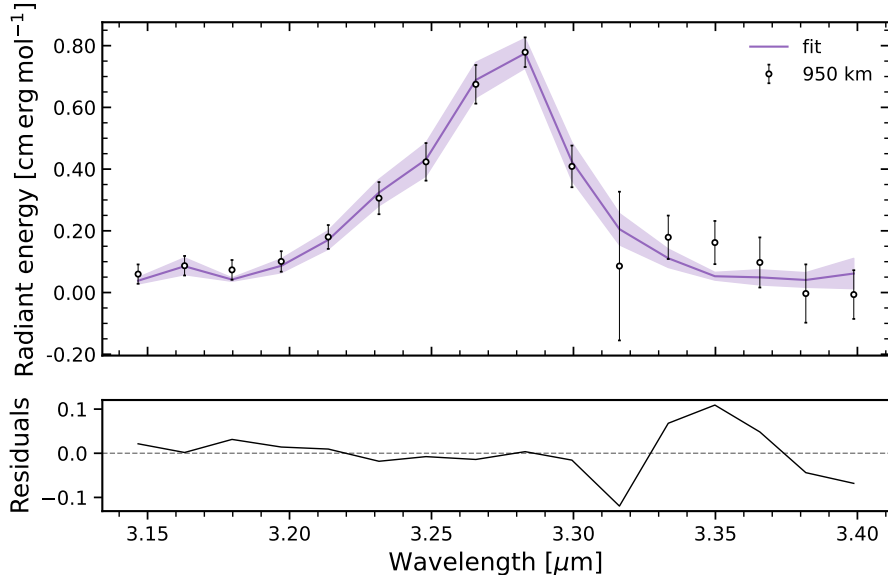


FIG. 3.2 – Monte Carlo fit using PAHdb v1.20 for 950 km, based on 1000 iterations. Top: median fit (purple) and  $1\sigma$  uncertainty band (shaded) over observed data. Bottom: residuals between median fit and data. The median reduced  $\chi^2 = 1.63$ .

However, the single NNLS fits of 900, 950, and 1000 km provide limited insight into the underlying PAH population, as they do not capture uncertainties or the variability introduced by spectral noise and the degenerate regime we are fitting with +200 PAHs on 16 datapoints. To address this, we apply a Monte Carlo approach to assess the robustness of our results and estimate uncertainties on derived quantities such as PAH frequency and ring-size distribution. As described in Section 2.3.3, this method involves randomly perturbing the VIMS spectrum within its error margins using a normal distribution and refitting the perturbed spectrum each time with NNLS. [López-Puertas et al. \(2013\)](#) do not specify the number of iterations used. We adopt 1000 simulations because it strikes a balance between statistical reliability and computational cost. This number is used consistently throughout the remainder of the analysis.

The median MC fit at 950 km is shown in Figure 3.2, with the shaded region indicating

the  $1\sigma$  uncertainty band. The residual is consistent with the NNLS results in figure 3.1. Doing this analysis for all three heights allows us to compare our results to the 19 most prominent UIDs reported by López-Puertas et al. (2013, Table 2).

As shown in Figure 3.3, 10 of the PAHs listed in López-Puertas et al. (2013, Table 2) also appear in our results. For most of these species, the relative abundances agree within uncertainty, suggesting a consistent core population across both fits. An exception is UID 105 ( $C_{42}H_{18}$ ), which appears more prominently in our results, and has a two-peaked signal around 3.21 and 3.28  $\mu m$ . Notably, UID 356 ( $C_{22}H_{16}$ ), which contributes  $8.3 \pm 13.6\%$  in López-Puertas et al. (2013), is absent from our fits. Instead, we find higher contributions from UID 357 ( $C_{24}H_{24}$ ) and UID 378 ( $C_{24}H_{16}$ ), with abundances of  $8.3 \pm 12.0\%$  and  $5.9 \pm 8.3\%$ , respectively. These molecules are similar in size and structure to UID 356. Both UID 356 and UID 378 produce a sharp emission feature at 3.28  $\mu m$  with a steep drop-off between 3.28 and 3.30  $\mu m$ , indicating their importance in reproducing the red edge of the main PAH band. UID 357 contributes more broadly in the red wing of the spectrum. These differences suggest that while the overall population is consistent, the specific PAHs contributing to key spectral regions vary slightly depending on methods used.

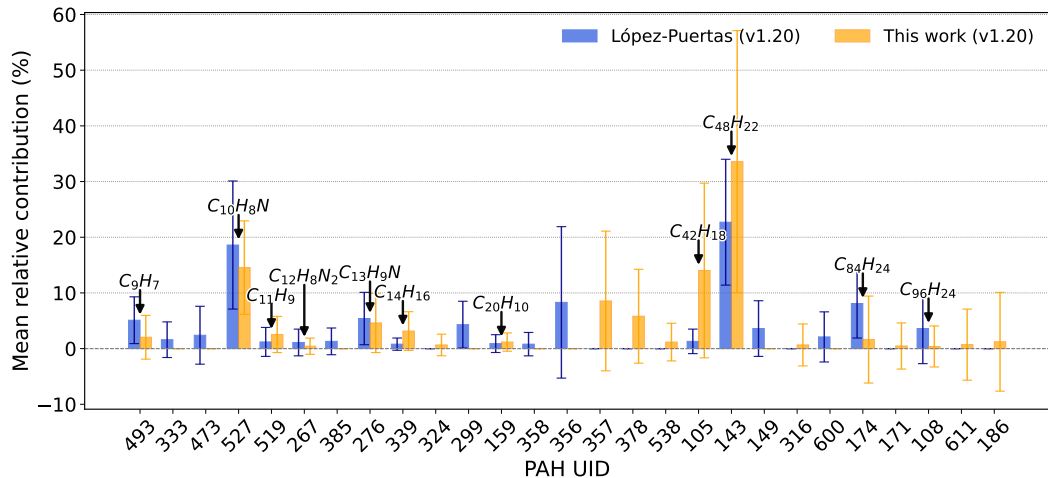


FIG. 3.3 – Comparison of mean relative contributions from our MC fit (v1.20) in orange and Table 2 from López-Puertas et al. (2013) in blue. The x-axis shows PAH UIDs ordered by carbon count. Annotated labels indicate the 10 overlapping UIDs in both sets. The error bars indicate the standard deviation of the value.

We use the Monte Carlo ensemble to analyze the distribution of PAH ring sizes at each altitude. Figure 3.4 shows the normalized ring count distributions from 1000 MC runs for 900, 950, and 1000 km indicated in green, blue, and purple respectively. The black vertical lines mark the 10–11 ring range reported by López-Puertas et al. (2013).

At 900 km and 950 km, the median ring sizes are  $8.93 \pm 2.38$  and  $8.87 \pm 3.11$ , re-

spectively. This value is slightly below the previously reported range, but still within  $1\sigma$  of the reference values. At 1000 km, the median increases to  $10.63 \pm 7.02$ , consistent with the earlier estimate but with a much broader spread. Unlike the results of López-Puertas et al. (2013), we do not observe a strong height dependence: the mean values at all three altitudes lie within each other's  $1\sigma$  intervals.

Together with the NNLS and MC fits (Figures 3.1 and 3.2), the PAH comparison (Figure 3.3), and the ring distributions (Figure 3.4), our results suggest partial agreement with López-Puertas et al. (2013), despite methodological differences such as programming language (IDL vs. Python).

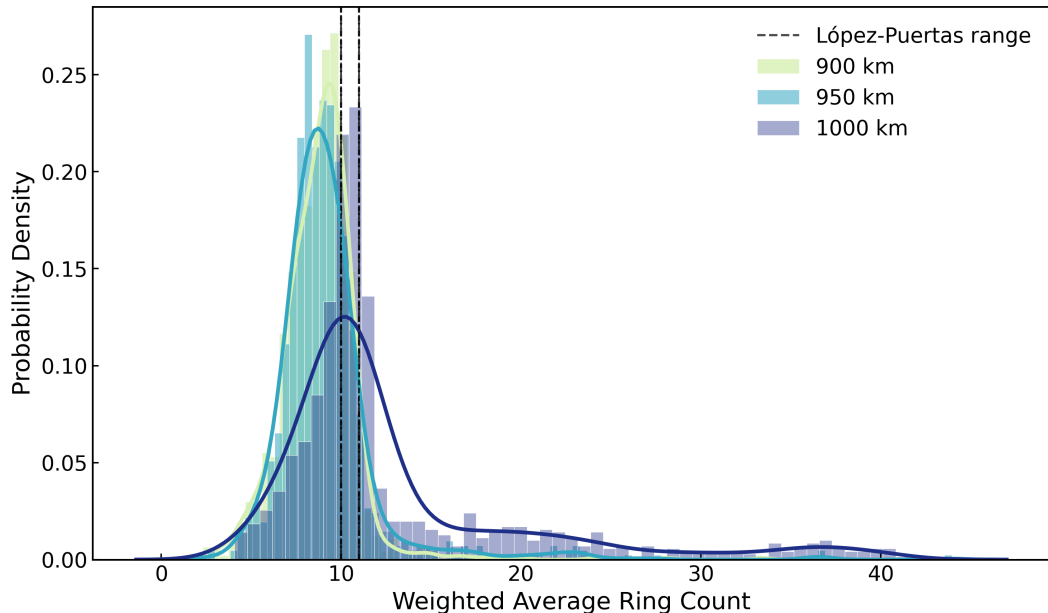


FIG. 3.4 – Distribution of ring counts from the 1000 MC runs using PAHdb v1.20. The x-axis shows PAH ring size; the y-axis shows normalized probability. Black lines mark the range reported by López-Puertas et al. (2013). The median values with  $1\sigma$ -standard deviation for the heights are  $8.93 \pm 2.38$ ,  $8.87 \pm 3.11$ , and  $10.63 \pm 7.02$  for 900, 950 and 1000 km.

## 3.2 Refining the Fit with an expanded PAHdb

Building on the findings discussed in section 3.1, we improve the analysis using PAHdb v3.20 and an enhanced fitting method, as detailed in Section 2. With our PAH constraints from section 2.2.4 version 3.20 of the PAHdb includes 2632 species (2170 neutrals and 462 anions) (Bauschlicher et al. 2018; Mackie et al. 2015). This expanded database allows us to test the role of anions in fitting Titan's infrared emission. We used the updated photon absorption cross section and applied per-PAH normalization (see Section 2.2.4). Fits were performed using both NNLC and Monte Carlo

simulations with NNLS fits.

Figure 3.5 shows the NNLC fit at 950 km. Fits for 900 and 1000 km are shown in Appendix A (Figures A.5 and A.7). In all three heights, the residuals flatten significantly in the red wing compared to the results in section 3.1, except near  $3.15 \mu\text{m}$  where the datapoint has the largest error bar. A residual of  $0.1 \text{ cm erg mol}^{-1}$  remains. Despite this visual improvement, the reduced- $\chi^2$  values decrease well below unity, indicating possible overfitting. For 900, 950, and 1000 km, the values drop from 2.278, 0.969, and 0.518 (v1.20) to 0.618, 0.150, and 0.229 with the updated methods and PAHdb v3.20. These results suggest a trade-off between fit smoothness and statistical reliability, which we explore further below. UID 159 ( $\text{C}_{20}\text{H}_{10}$ ), 527 ( $\text{C}_{10}\text{H}_8\text{N}$ ) are the top contributing PAHs for 900 and 950 km. For 1000 km UID 527 is the second most abundant, with anionic UID 614  $\text{C}_{10}\text{H}_8^-$  being most abundant.

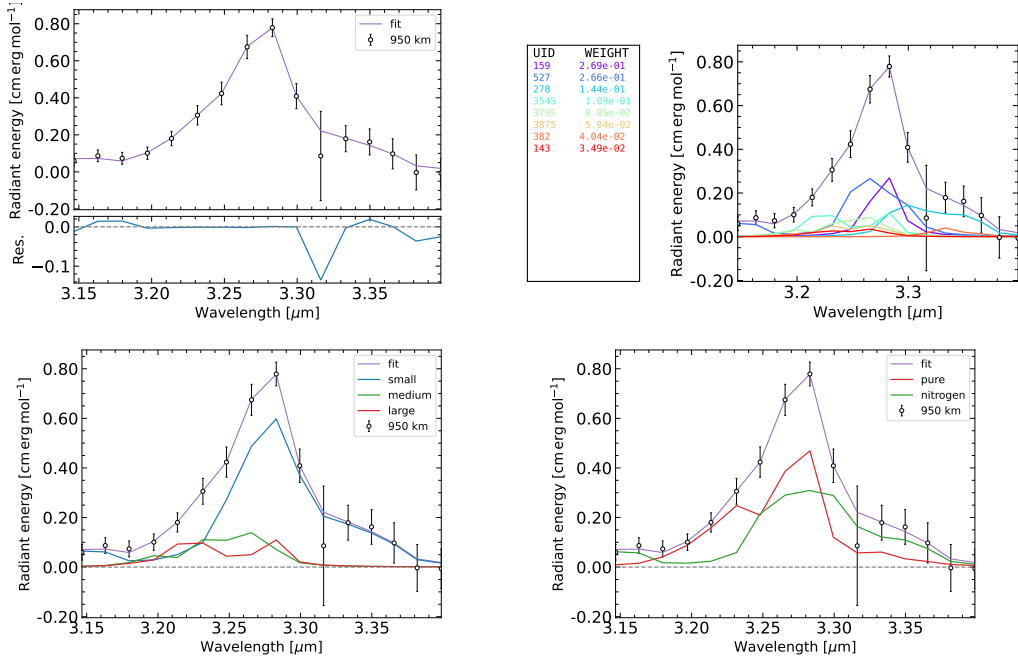


FIG. 3.5 – NNLC fit using PAHdb v3.20 to VIMS observations at 950 km. Top left: contributions from selected PAHs. Top right: observed spectrum (black) and NNLC fit (purple), with residuals. Bottom left: contributions by PAH size class. Bottom right: breakdown by pure PAHs (red) and nitrogen-containing PANHs (green).

In the bottom left panel of figures 3.5, A.5, and A.7 we see a contribution of small ( $N_c < 50$ ) PAHs, but also an increase in medium ( $50 < N_c < 70$ ) and even large ( $N_c > 70$ ) sized PAH species. These appear more towards the blue part of the spectrum. In the bottom right panel of figure 3.5 we again see a significant contribution of nitrogen containing species. Important to note is that v1.20 had 37 Nitrogen containing species, and v3.20 has 40, only 3 more. The same happens for 900 and 1000 km in

figure A.5 and A.7. For 900 and 950 km the PANHs even dominate around 3.30 to 3.32  $\mu\text{m}$ . Compared to the v1.20 results, the inclusion of anions significantly improves the fit to the red wing of the 3.28  $\mu\text{m}$  feature. This is confirmed in Figure 3.6, which reveals that small ( $N_c < 50$ ) anionic species account for a substantial fraction of the total emission in the region of 3.26 to 3.38  $\mu\text{m}$ . This is also visible in figures A.5 and A.7.

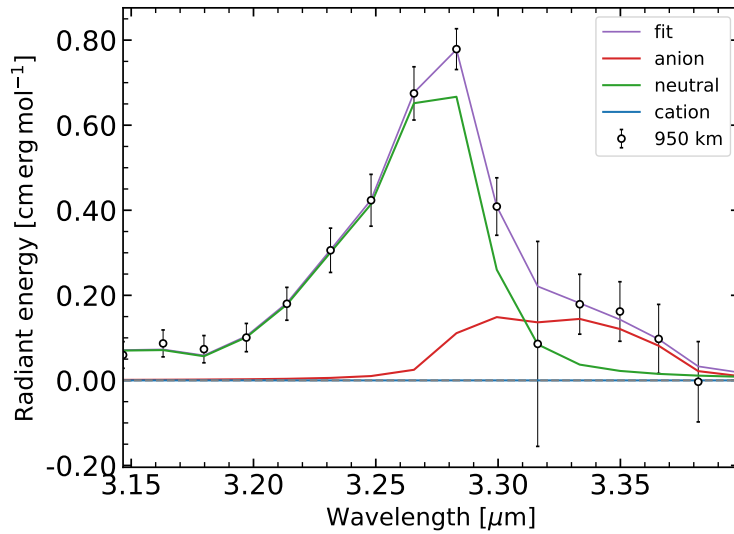


FIG. 3.6 – Charge composition of the NNLC fit at 950 km using v3.20. Neutral (green) and anionic (red) contributions are shown. Cations are not included in this fit.

However, just as in section 3.1 we need to turn to Monte Carlo fitting to properly constrain our fits, because they have become even more degenerate with +2600 PAHs on 16 datapoints. Even though the reduced  $\chi^2$  have worsened, a single fit is not enough to make concrete statements about trends of PAH populations, see section 2.3.3. We also calculate errors on derived populations such as PAH frequencies and PAH ringsizes, see section 2.3.3.

To evaluate the robustness of the fit, we performed 1000 Monte Carlo iterations at each altitude by perturbing the input spectra within their uncertainties and refitting the data using the improved method described in Section 2. Figure 3.7 shows an example MC fit at 950 km, with corresponding fits at 900 and 1000 km shown in Appendix A, the residuals of these breakdowns are again comparable with their single fit counterparts indicating a good match (Figure A.8). To quantify fit quality across the ensemble, we computed the reduced  $\chi^2$  for each of the 1000 iterations of the MC fit. Using PAHdb v3.20, the median values are 1.42 (900 km), 1.02 (950 km), and 1.01 (1000 km), a notable improvement over the v1.20 medians of 2.17, 1.58, and 1.32. These values now cluster closer to the ideal reduced  $\chi^2 \approx 1$ , indicating better overall agreement between the model and data.

This improvement is also visible in the full distributions of the reduced  $\chi^2$  values in Figure 3.8. Compared to the fit performed in section 3.1 the v3.20 fits show narrower, more symmetric curves with shorter tails towards higher reduced  $\chi^2$  values. Fewer extreme outliers appear, and most iterations converge on a statistically sound fit. Taken together, these results point to a more consistent and reliable match between the cascade emission model and the observed VIMS spectra.

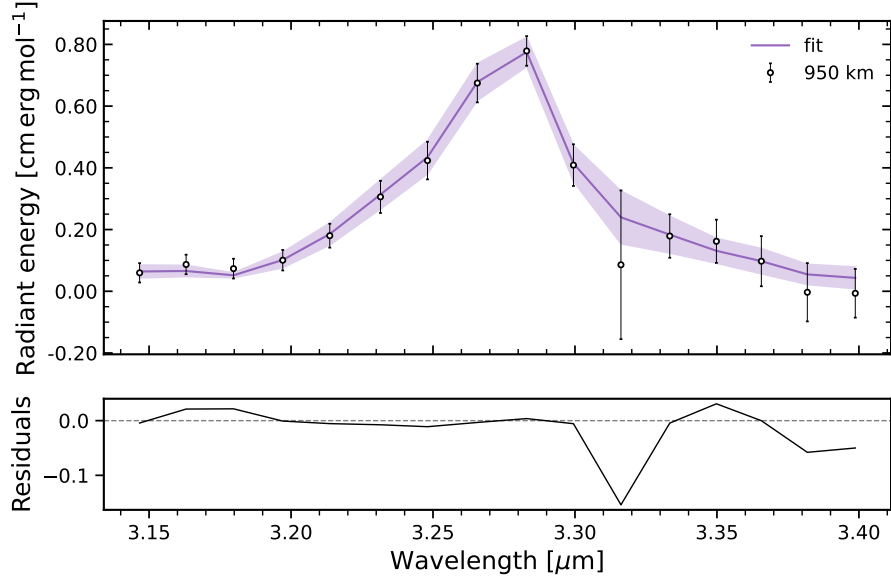


FIG. 3.7 – Monte Carlo fit using PAHdb v3.20 for 950 km, based on 1000 runs. Top: median fit (purple) and  $1\sigma$  uncertainty band overlaid on data. Bottom: residuals between fit and observations.

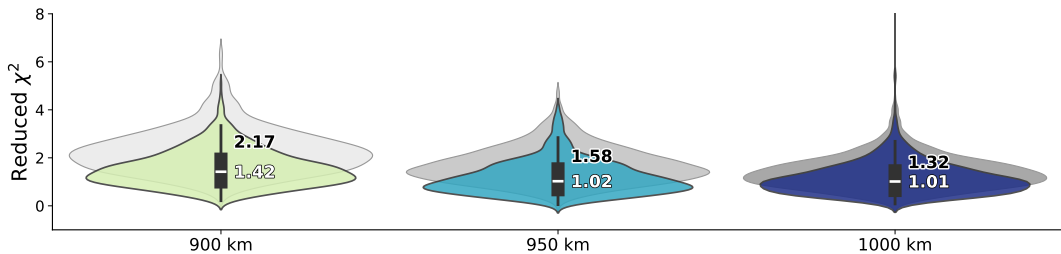


FIG. 3.8 – Distribution of reduced  $\chi^2$  values from 1000 MC NNLS fits across altitudes for v1.20 shaded in grey in the background and v3.20 in color in the foreground. Boxplots show quartiles; vertical ticks indicate median values, black for v1.20 and white for v3.20.

The v3.20 fits reveal a bimodal size distribution dominated by either small ( $N_C < 50$ ) or medium-sized ( $50 < N_C < 70$ ) PAHs, see figure 3.9. Several prominent contributors are nitrogenated or anionic, echoing trends seen in Figure 3.5. Species-level contributions vary with altitude. Small PAHs such as UID 527 ( $C_{10}H_8N$ ), UID 382 ( $C_{10}H_8^-$ ), UID 519 ( $C_{11}H_9$ ), and UID 159 ( $C_{20}H_{10}$ ) dominate the fits at 900

and 950 km. The medium-sized anionic UID 734 ( $C_{63}H_{21}^-$ ) contributes significantly at 900 km. While these species remain present at 1000 km their relative contributions diminish. The fit becomes more diffuse, with a broader mix of lower-abundance PAHs, each contributing less than 5%, suggesting increased compositional diversity or degeneracy at higher altitude.

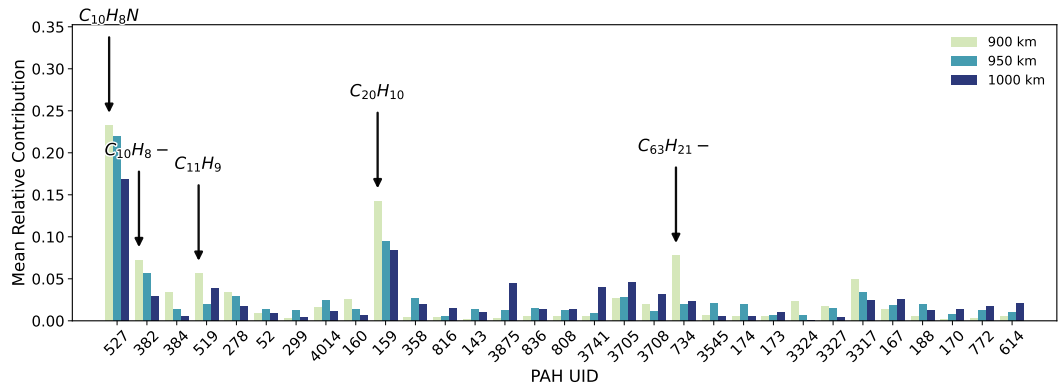


FIG. 3.9 – Relative contribution of each PAH to the 1000 MC fits at all altitudes using PAHdb v3.20. The x-axis shows UID ordered by carbon atom amount. Dominant species are annotated.

When aggregating contributions across heights and comparing to Table 2 of López-Puertas et al. (2013), we find only four overlapping species (Figure 3.10). Notably, UID 143 ( $C_{48}H_{22}$ ), previously the most abundant species, disappears entirely. In contrast, UID 527 ( $C_{10}H_8N$ ) remains significant across both studies. Also, the contribution of UID 159 ( $C_{20}H_{10}$ ) increases, which has a sharp peaked signal at 3.28  $\mu\text{m}$ . There are no other clear abundant PAHs, the most prominent contributions are spread out between PAHs that have less than 5% contribution each, indicating overall more PAHs that can fit the signal.

Next the ring sizes of the PA(N)Hs are calculated, see Figure 3.11. The median values increase compared to v1.20: from  $11.2 \pm 4.6$  (900 km), to  $13.6 \pm 5.5$  (950 km), and  $16.6 \pm 7.4$  (1000 km). However, as in section 3.1 the overlap in distributions implies no significant trend with altitude.

Overall, the reduced  $\chi^2$  distributions in figure 3.8 demonstrate improved fit quality with PAHdb v3.20, and the incorporation of anions, normalisation, and updated cross sections. The resulting PAH population appears larger and more diverse than previously inferred by López-Puertas et al. (2013), with the ringsizes averaging around 14, see figures 3.9 and 3.11. The fit itself has become more degenerate due to the increase of PA(N)Hs that are able to fit the data.

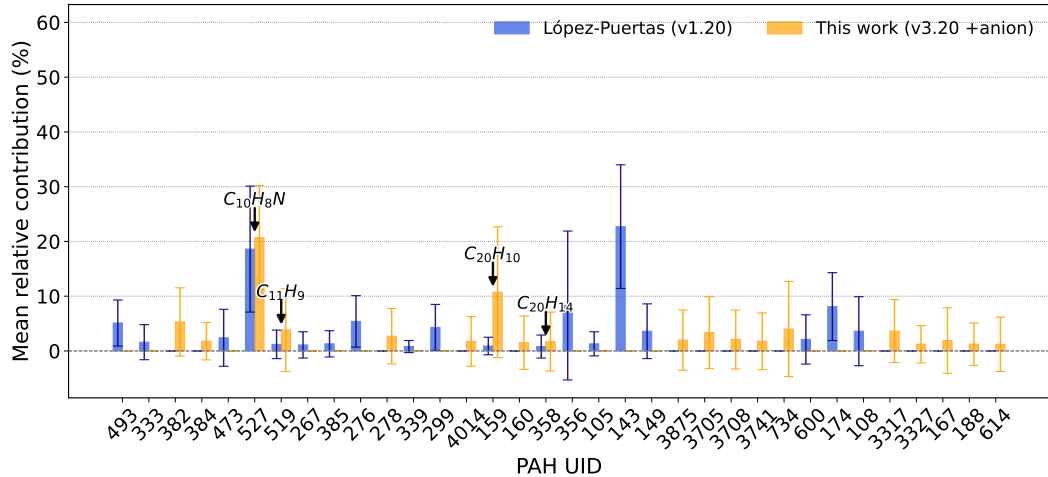


FIG. 3.10 – Comparison of mean relative contributions from our v3.20 MC fit (with anions) and Table 2 from López-Puertas et al. (2013). Overlapping species are labeled and the x-axis with UIDs is ordered by increasing carbon amount. Error bars show standard deviation of the calculated value.

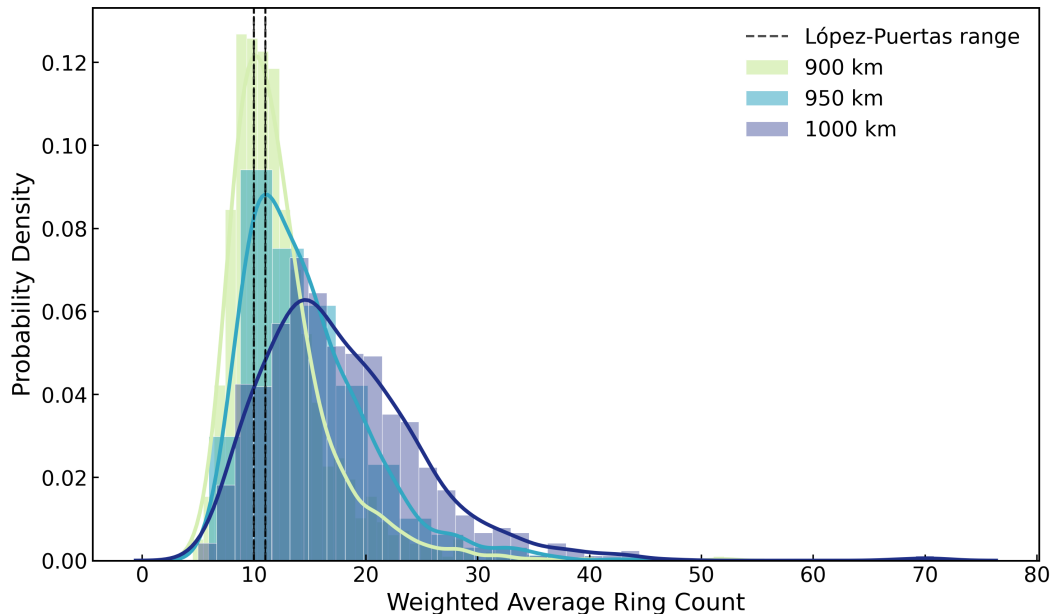


FIG. 3.11 – Distribution of ring counts from the 1000 MC fits using PAHdb v3.20. The shaded region shows the range from López-Puertas et al. (2013) with 10-11 rings. The ring sizes and their  $1\sigma$  standard deviations are:  $11.2 \pm 4.6$ , to  $13.6 \pm 5.5$ , and  $16.6 \pm 7.4$  for 900, 950, and 1000 km, respectively.

### 3.2.1 Additional constraints to the fit

Next we want to decrease the degeneracy of our fit and further improve the quality and physical plausibility of our results. There are two ways to do this: either get more data or inject more physical constraints to the PAHs that go into the fit. The VIMS range extends from 1-5  $\mu\text{m}$ , and there is a lot of data to be gained in that range (Allamandola et al. 2021). However, López-Puertas et al. (2013) already tried to extract that information and were unsuccessful. The datasets with the extended waverange of 1-5  $\mu\text{m}$  were not provided to us.

Thus, we focus on refining the PAH input space by limiting it to molecules that are more likely to exist in Titan's upper atmosphere. We impose a carbon count upper limit of 28 atoms corresponding to a dimer of anthracene (3 rings  $\times$  2), see Figure 1.1, previously suggested to form in Titan's ionosphere (Waite et al. 2007; Haythornthwaite et al. 2021). Applying this constraint to PAHdb v3.20 yields 354 PAHs (330 neutrals, 24 anions), and we re-run the full NNLC and Monte Carlo analysis using this physically filtered subset.

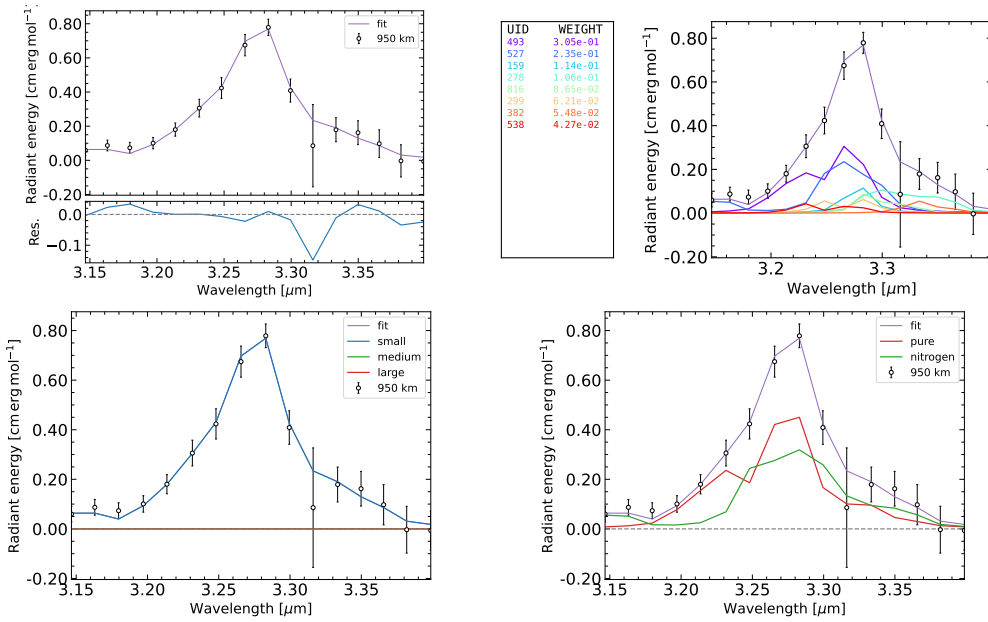


FIG. 3.12 – NNLC fit using PAHdb v3.20 constrained to  $N_c < 29$  at 950 km. Panels show the same as in figure 3.1

Figure 3.12 shows the NNLC fit at 950 km, with 900 and 1000 km shown in figure A.9 and A.11. Compared with the results in section 3.2 we see a flattened out residual in the top left panel, again except for the datapoint with the large error bar at 3.15  $\mu\text{m}$ . In the top right panel we see that UID 493 ( $C_9H_7$ ), 527 ( $C_{10}H_8N$ ), and 816 ( $C_{31}H_{17}$ )

are in the top 2 contributed to the fits in 900, 950, and 1000 km. 493 and 527 have more broader spectral signals while 816 has a sharp rise near  $3.28\text{ }\mu\text{m}$  and a broad dropoff towards the red wing.

The results now consist solely of small PAHs ( $N_c < 50$ ), with the updated charge distribution shown in Figure 3.13, where we again see a contribution of anions in the red wing. The reduced  $\chi^2$  values for these fits are 0.847, 0.352, and 0.480 for 900, 950, and 1000 km, respectively. These values seem more balanced than the ones calculated in section 3.2.

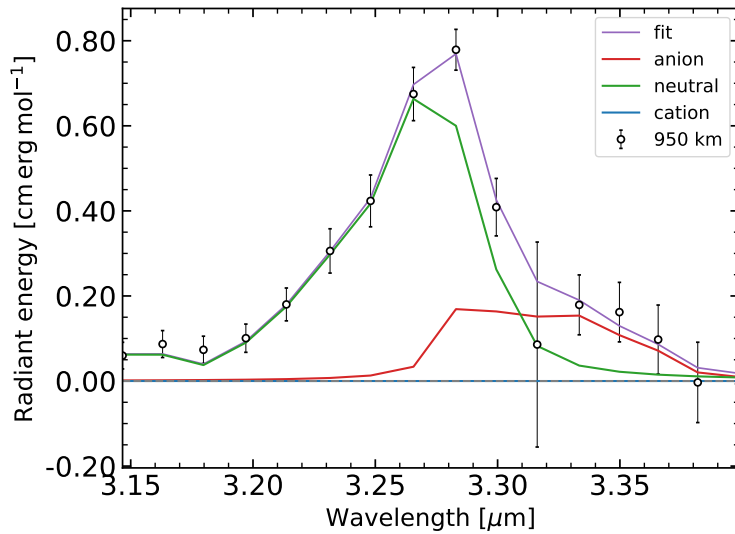


FIG. 3.13 – Charge composition of the NNLC fit (PAHdb v3.20,  $N_c < 29$ ) at 950 km. Neutral (green) and anionic (red) contributions are shown.

If we then apply the Monte Carlo fitting to this dataset, as discussed in section 2.3.3, we generate figures 3.14, 3.15, and 3.16. In figure 3.14 we compare the reduced  $\chi^2$  distributions of the Monte Carlo ensemble with those calculated in section 3.2. We see a slightly elevated median reduced  $\chi^2$  value for all the heights, and a broadened distribution. This is an indication of slight underfitting and therefore a worse fit of the model with the data.

Population statistics shift significantly under this constraint. As shown in Figure 3.15, smaller PAHs now dominate, with UID=527 ( $C_{10}H_8N$ ) still contributing prominently and UID 816 ( $C_{26}H_{16}-$ ) being the largest most abundant PAH. UID 733 ( $C_{28}H_{14}-$ ) is the largest PAH overall, with the highest abundance at 1000 km. The abundances for UID 493 ( $C_9H_7$ ), UID 527 ( $C_{10}H_8N$ ), UID 159 ( $C_{20}H_{10}$ ), and UID 816 ( $C_{26}H_{16}^-$ ) decrease with increasing altitude. The abundance of UID 299 ( $C_{16}H_{10}N_2$ ) remains the same at 950 km and 1000 km, and is the first PAH containing more than one nitrogen we see abundantly. The spectral signal has two peaks at  $3.24\text{ }\mu\text{m}$  and  $3.28\text{ }\mu\text{m}$ . UID 519 ( $C_{11}H_9$ ) and 4015 ( $C_{11}H_9$ ) are notably more abundant at 1000 km

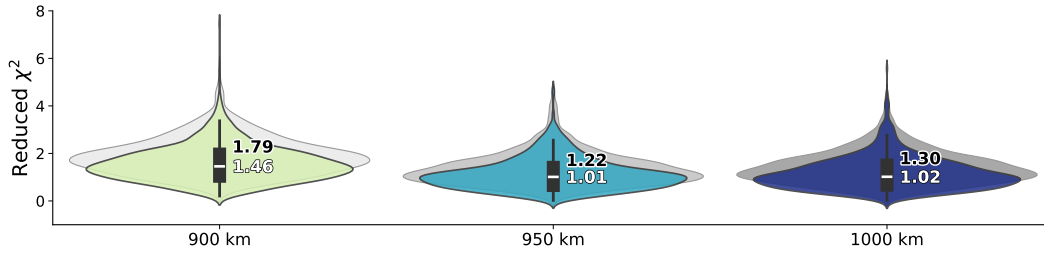


FIG. 3.14 – Reduced  $\chi^2$  distributions for the full (v3.20) on the foreground in colour, median values annotated in white, and constrained (v3.20,  $N_c < 29$ ) PAH sets on the background in grey with median values annotated in black, across 1000 MC runs.

than at the other heights. These have two very different spectral signals and with 519 having a sharp peak, whereas 4015 has an indent between two peaks. Together, they can build up the signal observed at 1000 km.

Next we look at the ring count distribution, in Figure 3.16. The sizes have decreased to 3.5 rings, far below the earlier estimate by López-Puertas et al. (2013) and the one in section 3.2. The standard deviation is the lowest it has been until now. Also since the spread of the population is now so narrow, the probability density peaks nearly at 1, compared to 0.12 in figure 3.11, indicating a highly probable value. However, the populations still overlap within  $1\sigma$  and thus there is again no significant difference between them.

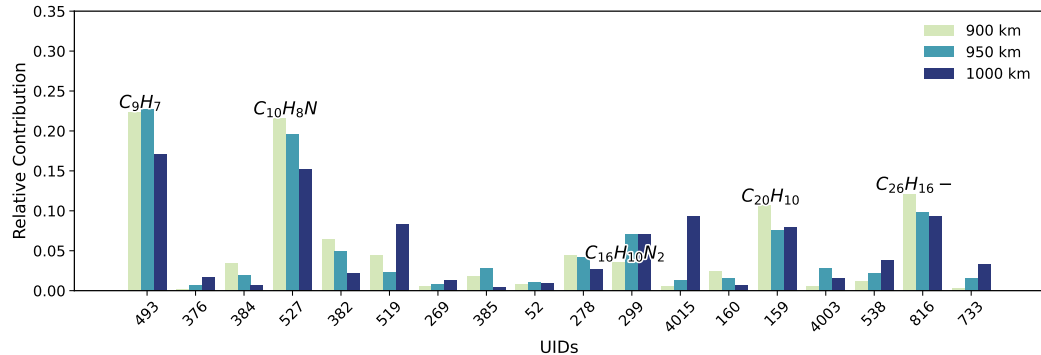


FIG. 3.15 – Relative contribution of each PAH to the 1000 MC fits across all altitudes using the constrained ( $N_c < 29$ ) v3.20 database. The x-axis shows the UIDs ordered by increasing carbon amount.

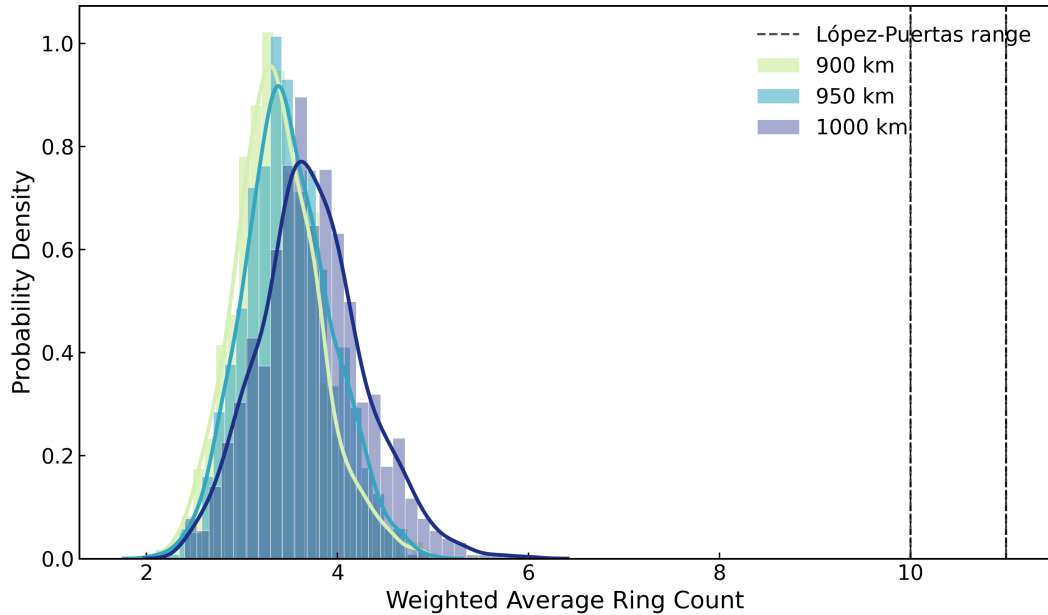


FIG. 3.16 – Ring count distribution for the 1000 MC fits using PAHdb v3.20 ( $N_c < 29$ ). Black lines indicate the earlier range from López-Puertas et al. (2013) at 10–11 rings. The median ring values and their standard deviations per height are:  $3.32 \pm 0.42$ ,  $3.44 \pm 0.47$ , and  $3.69 \pm 0.53$  for 900, 950, and 1000 km, respectively.

### 3.3 Fits Using PAHdb Version 4.00

We also tested the most recent PAHdb release, version 4.00. This version includes 4919 PAHs (3681 neutrals, 1238 anions, and 1016 PAHNs). This version improves upon earlier releases by removing the need for an anharmonic redshift correction (Maragkoudakis et al. 2024). PAHdb version 4.00 features a greatly expanded and more chemically accurate set of DFT-computed spectra, including neutral, ionized, nitrogenated, and large irregular PAH species, using improved basis sets for the quantum calculations (Ricca et al. 2021). Due to this enhanced spectral fidelity, the empirical anharmonic redshift ( $15 \text{ cm}^{-1}$ ) previously used is no longer necessary and Maragkoudakis et al. (2024) do not apply this shift in their fitting processes, so neither will we. We only show the MC population results. For the specific NNLC fits and MC fit summaries, look in appendix A.4.

Figure 3.17 shows the reduced  $\chi^2$  values for version 4.00, which are comparable to v3.20 but show slight underfitting at 1000 km. The sides of the distribution also seem to protrude outward more, indicating more fits with reduced  $\chi^2$  at those values. However, the distributions do become more asymmetric, most notably at 950 km. A bump appears in the distribution at reduced  $\chi^2 \approx 4$ , indicating more underfitted sets.

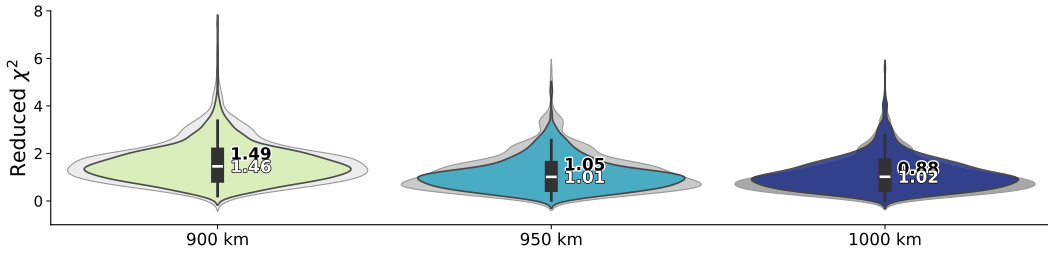


FIG. 3.17 – Reduced  $\chi^2$  distributions for the v4.00 database (grey, median values indicated in black) compared to the distributions of v3.20 on the foreground, median values indicated in white.

Furthermore, the population statistics (Figure 3.18) indicate a dominance of medium and large PAHs, including some  $N_2$  and even  $N_3$  PANHs. Once again, UID=527 ( $C_{10}H_8N$ ) remains a significant contributor, and has a similar contribution across all heights. UID 8858 ( $C_{93}H_{24}N_3$ ) is the most abundant PA(N)H overall, especially at 900 and 950 km. In figures A.13, A.14, and A.15 we see that large PAHs now dominate over the small species.

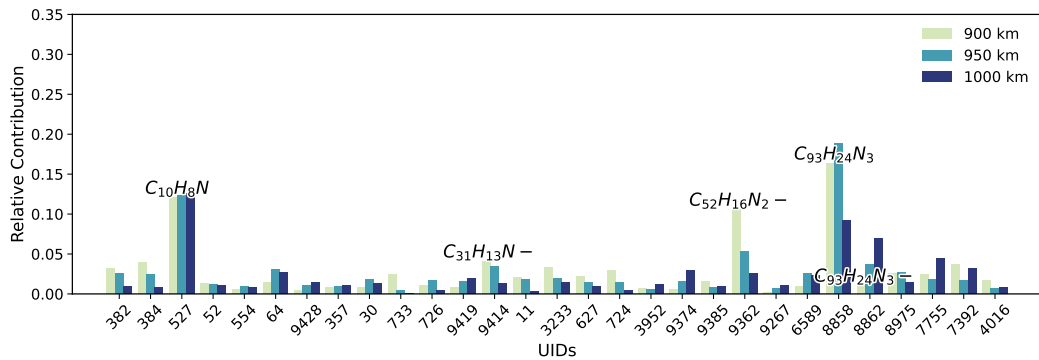


FIG. 3.18 – Relative contributions of each PAH to the 1000 MC fits across all altitudes using v4.00 of the NASA Ames PAHdb. The x-axis shows the UID's ordered by increasing carbon amount.

Finally, we look at the ringsize population distributions across the 1000 MC runs in Figure 3.19. It has the largest values until now at around 20 rings and is far from the range proposed by López-Puertas et al. (2013). The value is relatively close to the one defined in section 3.2. The spread of the population is large, indicating large uncertainties on the values defined. The distributions also seem skewed, especially for 1000 km, meaning the population does not follow a normal distribution as expected.

### 3.3.1 Physically Constrained Fit with v4.00 ( $N_c < 29$ )

Finally, we repeated the carbon cut with v4.00. This yields 365 PAHs (335 neutral, 30 anions, 49 PAHNs). The population results from the MC ensemble are shown

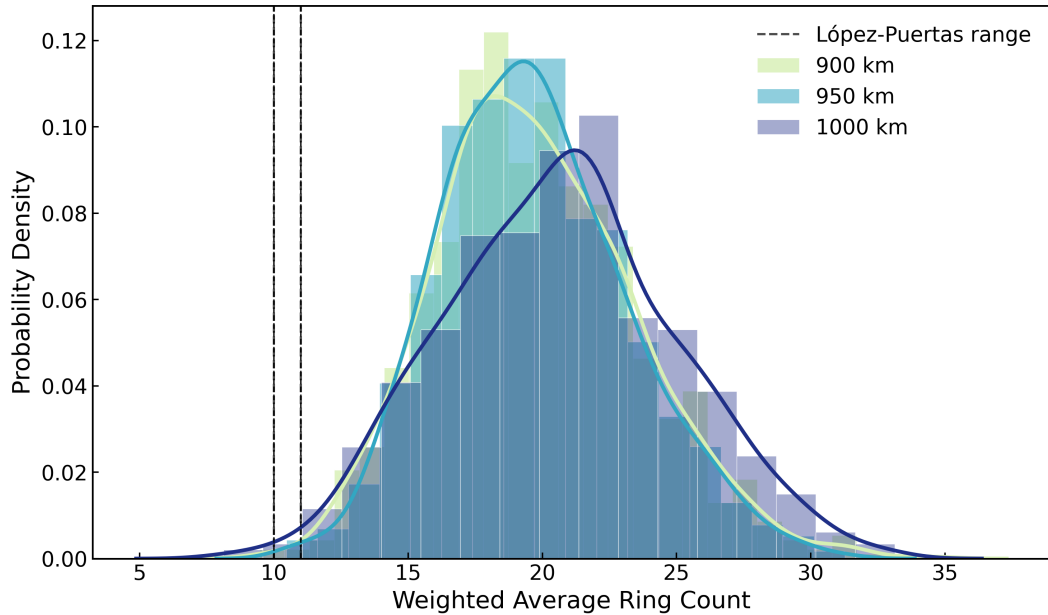


FIG. 3.19 – Ring count distribution for the 1000 MC fits using PAHdb v4.00. The x-axis shows the ring count and the black lines indicate the range of 10-11 rings calculated by López-Puertas et al. (2013). The mean ring sizes with  $1\sigma$  standard deviation are  $19.52 \pm 3.72$ ,  $19.41 \pm 3.46$ , and  $20.66 \pm 4.32$ .

below. Figure 3.20 shows a slightly worse fit statistically with the medians being further away from 1 and the distributions extended upward. However, the frequency distribution in Figure 3.21 appears more physically plausible. Once more,  $C_{10}H_8N$  (UID=527) remains a stable presence across all tests. UID 339 ( $C_{14}H_{16}$ ) and 299 ( $C_{16}H_{10}N_2$ ) also appear prominent with the former more present at 900 and the latter more at 1000 km. Same as in section 3.2.1, UID 733 ( $C_{28}H_{14}^-$ ) is the largest PAH present and has similar contributions across all heights.

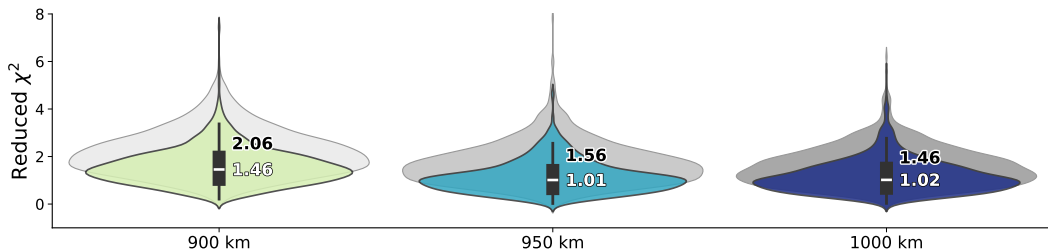


FIG. 3.20 – Reduced  $\chi^2$  comparison between the constrained v4.00 ( $N_c < 29$ ), indicated in grayscale with medians annotated in black, and v3.20 fits in colour and medians annotated in white.

If we then finally look at the ringsize distribution for this set of PAHs in the MC fit, in figure 3.22, we see a binomial distribution across all height. The first peak is

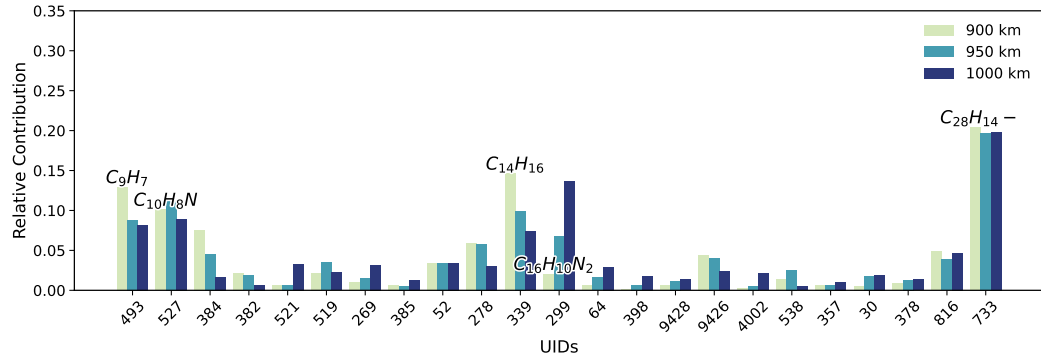


FIG. 3.21 – PAH contribution frequencies from the MC fits using v4.00 constrained to  $N_c < 29$ . The UIDs on the x-axis are ordered by increasing number of carbon atoms.

centered around 3.5, same as in section 3.2.1, and the second peak is at 5 rings. This indicates a distribution reflected in figure 3.21. It seems that in this fit either 2-3 rings, or 5-6 rings appear.

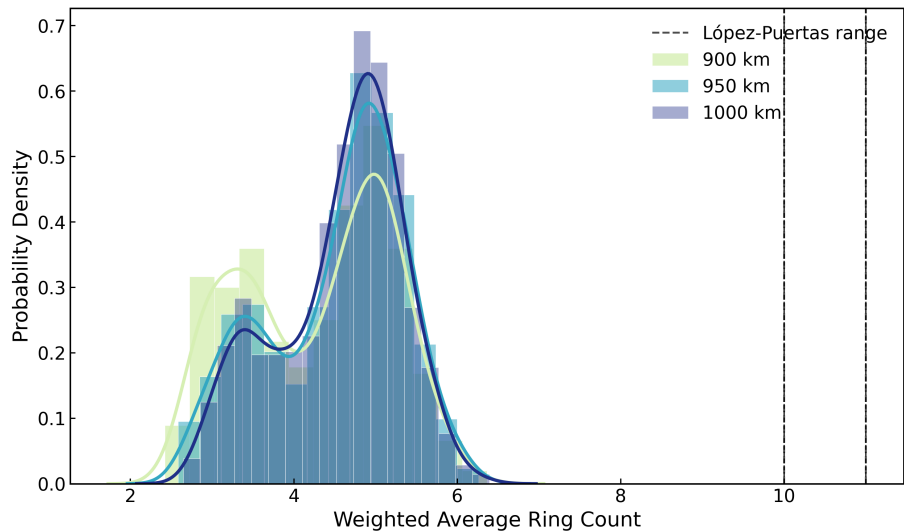


FIG. 3.22 – Ring count distribution for the 1000 MC fits using PAHdb v4.00 with constraints of  $C < 29$ . The x-axis shows the ring count and the black lines indicate the range of 10-11 rings calculated by López-Puertas et al. (2013). The mean ring sizes with  $1\sigma$  standard deviation are  $4.50 \pm 0.92$ ,  $4.73 \pm 0.83$ , and  $4.73 \pm 0.76$ .

# Chapter 4

## Discussion

This chapter interprets the results presented in Section 3. We first evaluate how well our methods reproduce and extend the work of [López-Puertas et al. \(2013\)](#). We then examine the implications of these results for Titan’s atmospheric chemistry, discuss methodological limitations, and conclude with directions for future work.

### 4.1 Comparison with López-Puertas et al. (2013)

Our first goal was to reproduce the results of [López-Puertas et al. \(2013\)](#). Using PAHdb v1.20 and their methodology, see section 3.1). We find that ten of the most prominent species in our fits match their Table 2 (Figure 3.3). The main differences are a smaller contribution from UID 356 ( $C_{22}H_{16}$ ) and stronger contributions from UID 357 ( $C_{24}H_{24}$ ), 378 ( $C_{24}H_{24}$ ), and 105 ( $C_{42}H_{18}$ ). Inspection of individual spectra (Appendix A.6) shows that species that disappear are replaced by others with similar spectral shapes. The retrieved ring-size distribution (Figure 3.4) agrees with their 10–11 ring median. Unlike their results, we include standard deviations in the distributions and see no significant trend with altitude. This contradicts their inference of larger PAHs at high altitude due to ion–neutral chemistry ([Westlake et al. 2014](#); [López-Puertas et al. 2013](#)). Instead, our results suggest that multiple formation pathways contribute across all altitudes (Section 1.2.2).

Finally, the PAHs we retrieve are heavier than the positive ions seen by CAPS/IBS but consistent with the negative ions detected by CAPS/ELS ([Waite et al. 2007, 2010](#); [Crary et al. 2009](#); [Coates et al. 2007](#)). Overall, despite methodological differences between IDL and Python ([Kouatchou & Medema 2018](#)), we reproduce the main findings of [López-Puertas et al. \(2013\)](#) reasonably and can now refine these results with updated PAH databases and fitting methods.

## 4.2 Impact of database updates and constrained fits

We extended the analysis to four database configurations: v3.20, v4.00, and constrained versions of both where only species with fewer than 29 carbons were allowed, consistent with limits on Titan’s upper atmosphere ([Waite et al. 2007](#); [Haythorntwaite et al. 2021](#)). Later versions of PAHdb include more molecules and more accurate vibrational frequencies (Section 1.2.1, [Bauschlicher et al. 2018](#); [Maragkoudakis et al. 2024](#)).

Table 4.1 summarizes the molecular content of these databases. The most significant change is the strong increase in nitrogen-containing PAHs (PAHNs) from 1% in v3.20 to 21% in v4.00. The database has also grown toward medium and large species, but not so much in small species [Bauschlicher et al. \(2018\)](#); [Maragkoudakis et al. \(2024\)](#).

	Neutral	Anion	Total	Neutral N	Anion N	Total N	$\frac{N}{Total}$
v1.20	201	58	259	37	2	39	15%
v3.20	2170	462	2632	40	2	42	1%
v3.20 C < 29	330	24	354	40	2	42	12%
v4.00	3681	1238	4919	529	487	1016	21%
v4.00 C < 29	335	30	365	44	5	49	13%

TABLE 4.1 Number of molecules in different versions of the NASA Ames PAH IR Spectroscopic Database.

Across all scenarios, a small set of compact PA(N)Hs dominates (Section 3, Appendix A). UID 527 ( $C_{10}H_8N$ ) appears in every fit as the strongest contributor, see figure 4.1 for its molecular structure. Nitrogen-bearing and anionic species (e.g., UID 278, 382, 384) also appear consistently. Larger neutrals (e.g., UID 159) and mid-sized contributors (299, 538, 493, 816) occur but vary with database constraints. Very large PAHs (3317, 3705, 3875, 8858) only appear in unconstrained fits, indicating that Titan’s 3  $\mu m$  emission is primarily driven by a compact, chemically stable core of PA(N)Hs.

Fit quality, quantified by the reduced  $\chi^2$ , also reflects these trends. Monte Carlo NNLC fits systematically reduce degeneracy compared to single fits, shifting ensemble  $\chi^2$  values toward unity (Figures 3.1 and 3.5). The constrained v3.20 fits achieve the most balanced trade-off: good  $\chi^2$  values without introducing unphysical large PAHs.

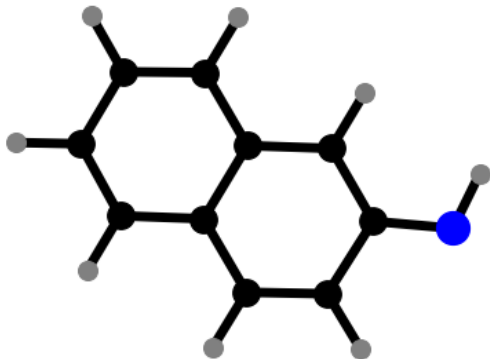


FIG. 4.1 – The molecular structure of UID 527 ( $C_{10}H_8N$ ). Black dots are carbon atoms, grey ones are hydrogen, and blue is nitrogen. The molecule is assymetric.

### 4.3 Interpretation for Titan’s atmospheric chemistry

These results strengthen the view that Titan’s  $3.28 \mu m$  emission is produced mainly by small, stable aromatic species. In contrast to [López-Puertas et al. \(2013\)](#), we find no altitude trend in ring size. Instead, ion-neutral chemistry appears active across the full altitude range, and possibly other formation mechanisms as well, see section 1.2.2.

Nitrogen-containing PAHs (PANHs) stand out.  $C_{10}H_8N$  (UID 527) appears in every scenario, suggesting that incorporation of nitrogen from Titan’s abundant  $N_2$  is a key pathway in PAH growth. This finding highlights the need to include PANHs in Titan photochemical models. We even find some  $N_2$  and  $N_3$  containing species, in line with what we would expect in Titan’s atmosphere ([Derenne et al. 2012](#)).

A key methodological improvement over earlier work is the inclusion of anions in the fits. These anions are essential to reproduce the red wing of the  $3.3 \mu m$  feature. Combined with Cassini’s in situ measurements of positive ions, our results show that all charge states—neutral, positive, and negative—play a role in Titan’s upper atmosphere [Coates et al. \(2007\)](#); [Crary et al. \(2009\)](#); [Haythornthwaite et al. \(2021\)](#).

Alternative carriers of the  $3.28 \mu m$  band were considered, but no non-PAH candidates can explain the observations (Appendix B). Aromatics remain the best explanation, with some room for contributions from other hydrocarbons ([Crary et al. 2009](#); [Haythornthwaite et al. 2021](#)). [Niraula et al. \(2025\)](#) highlight the degeneracy of  $1\text{--}5 \mu m$  hydrocarbons but also point to distinctive peaks that may help separate

them.

These aromatic molecules likely act as precursors for haze particle formation, consistent with aerosol growth models ([Waite et al. 2007](#); [Schulz et al. 2021](#)). Recent models and laboratory work confirm that cyano-PAHs such as C<sub>10</sub>H<sub>8</sub>N form efficiently in Titan’s ionosphere ([Zhou et al. 2025](#)), matching our results.

## 4.4 Methodological limitations

Three main limitations affect our conclusions: First there is database coverage, since v4.00 significantly improves PAH coverage, but the fits do not significantly improve, see section 3.3. The database may still lack key species for Titan’s atmosphere, particularly small/middle/large PANHs. Secondly, there is the line shape used for convolving the cascade emission. There is a debate on whether and when to use Gaussian or Lorentzian profiles. While computationally efficient, Gaussian broadening may not fully capture the true line shapes of vibrational modes in Titan’s upper atmosphere, where anharmonic effects and pressure broadening could play a role ([Tielens 2008](#); [Mackie et al. 2021](#)). We can look at the direct effect of Gaussian vs. Lorentzian in figure 4.2. In our improved v3.20 fit there is a clear discrepancy between the use of Gaussian vs Lorentzian profiles with the Gaussian giving worse fits. This discrepancy nearly completely disappears with the 4.00 database but the results taken from those fits. However from this we can conclude that Lorentzians are the proper lineprofiles to use because they reproduce the observed band wings and asymmetries more accurately and remain consistent with the physics of pressure- and anharmonic-broadened molecular emission in Titan’s upper atmosphere ([Tielens 2008](#)).

Finally there are the Instrumental uncertainties. The dominant source of uncertainty in the PAH retrievals arises from the instrumental noise near 3.3  $\mu\text{m}$ , which is approximately 30 nW m<sup>-2</sup> nm<sup>-1</sup> sr<sup>-1</sup> ([López-Puertas et al. 2013](#)). Additional systematic uncertainties, such as the efficiency of energy redistribution and PAH band strengths, can contribute errors of up to a factor of two in the derived concentrations.

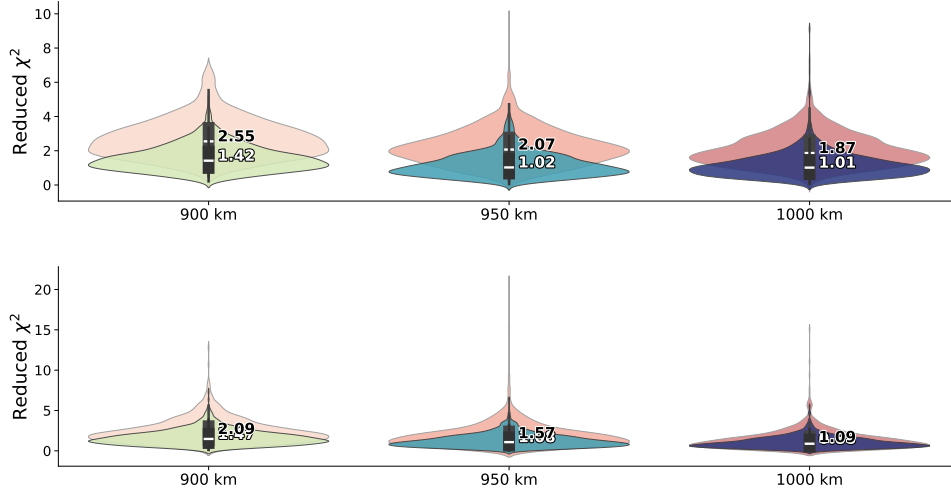


FIG. 4.2 – Reduced  $\chi^2$  distributions for Lorentzian vs. Gaussian line profiles (shaded in red). Top panel: v3.20, Bottem panel: v4.00.

## 4.5 Future work

The spectral window analyzed here is narrow ( $3.15\text{--}3.40\ \mu\text{m}$ ), with only 16 data points and a large number of possible carriers, leading to degeneracy. Future work should extend the fitting to a broader wavelength range. Even extending to  $3.0\text{--}3.5\ \mu\text{m}$  already reveals distinctive peaks, such as the  $3.14\ \mu\text{m}$  feature of UID 527 (Figure 4.3). Broader coverage, particularly in the  $1\text{--}5\ \mu\text{m}$  region, would help identify unique PAH features such as the C≡N stretch at  $4.69\ \mu\text{m}$  (Zhou et al. 2025).

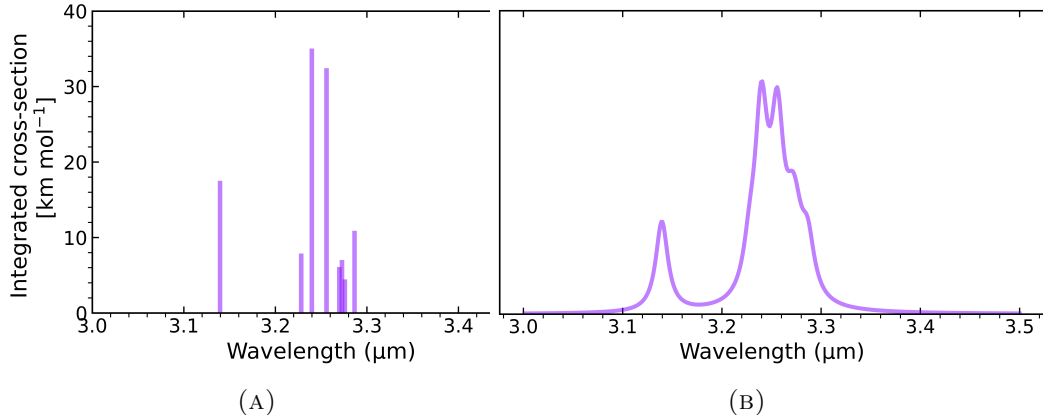


FIG. 4.3 – DFT-calculated spectrum of  $\text{C}_{10}\text{H}_8\text{N}$  UID = 527 from the NASA Ames PAH database around the  $3.28\ \mu\text{m}$  feature before (A) and after (B) the cascade emission modelling.

Finally, the consistently dominant UID 527 ( $\text{C}_{10}\text{H}_8\text{N}$ ) is a prime target for future work, figure 4.1 shows the molecular structure. The presence of 527 is invariant

and appears to be necessary to make the fit work. Also, the molecular weight of this molecule is 142.0657 amu. This corresponds with a peak in the CAPS/IBS mass spectrometry (Crary et al. 2009; Haythornthwaite et al. 2021). According Crary et al. (2009) Group 4 peaks at 141 amu, and was most likely attributed to the aromatic compound  $C_{11}H_9^-$ , but  $C_{10}H_8N$  would also be a strong match for that measurement. To research we can utilize the molecules strong dipole moment. Because this suggests UID 527 may also be detectable at radio or millimeter wavelengths through rotational spectroscopy with for instance ALMA.

The open-source pipeline developed for this thesis is available at `Titan_PAHs`<sup>1</sup> for future studies of Titan's complex atmospheric chemistry.

---

<sup>1</sup>[https://github.com/STIK98/Titan\\_PAHs](https://github.com/STIK98/Titan_PAHs)

# Chapter 5

## Conclusion

In this thesis we investigated the population of polycyclic aromatic hydrocarbons (PAHs) in Titan’s upper atmosphere using CH<sub>4</sub>-subtracted Cassini-VIMS spectra at 900, 950, and 1000 km. We modelled emission spectra for PA(N)Hs and fit them to the data with PAHdb v3.20. Building on López-Puertas et al. (2013), we expanded the molecules to include anions and removed fully dehydrogenated species. Using nonnegative least squares (NNLS), concentration-weighted (NNLC) fitting, photon cross-section updates, per-PAH normalisation, and Monte Carlo analysis, we built a framework that improves model–data agreement, with reduced  $\chi^2$  values near 1.

Our analysis shows a consistent ring-size distribution of about 10–18 rings at 900–1000 km, with no vertical variation. This range agrees with Titan PAH formation models (Vuitton et al. 2008) but exceeds previous estimates (López-Puertas et al. 2013). When applying a carbon limit ( $N_C < 29$ ) (Waite et al. 2007) and PAHdb v4.00 (Maragkoudakis et al. 2024), fits favoured smaller, nitrogenated PAHs, consistent with emerging data (Zhou et al. 2025). We tested five model scenarios (Table 4.1).

Notably, C<sub>10</sub>H<sub>8</sub>N (UID 527) appeared in all scenarios, suggesting chemical relevance. Although our method seeks trends rather than single molecules, the constant need for UID 527 hints that it may exist in Titan’s atmosphere. We recommend analysis of VIMS data at longer wavelengths, where signals near 3.28  $\mu\text{m}$  were missed, or follow-up ALMA observations targeting its rovibrational modes.

These results support a chemically complex, nitrogen-rich aromatic inventory in Titan, similar to processes thought to shape early Earth (Hörst 2017; Sandford et al. 2020; Zahnle et al. 2010). The identified PAH populations likely help form Titan’s haze and act as precursors to more complex organics interacting with the surface (Desai et al. 2017; Zhou et al. 2025). Our framework provides a foundation for future infrared retrievals of PA(N)Hs in Titan and other atmospheres. With JWST and ALMA able to detect rotational and vibrational transitions of key species, particu-

larly C<sub>10</sub>H<sub>8</sub>N and other cyanonaphthalenes ([Zhou et al. 2025; Nixon 2024](#)), this work links modelled PAH populations to targeted spectral signatures.

## Acknowledgements

I dedicate this thesis to Frans Schuurman, who believed in me over ten years ago at a time when I didn't believe in myself. He gave me the chance to build a future that would not have been possible otherwise.

My heartfelt thanks go to my supervisor, Dr. Alessandra Candian, one of the best scientists I've had the pleasure of working with. Her constant guidance, kindness, and encouragement inspired me to become the best version of myself during this project. She is also quite simply one of the nicest people I've ever met. Working with her was a true joy, and I hope our paths cross again.

To the Astrochemistry group thank you for patiently explaining basic chemistry to me. I think I finally almost understand what wavenumbers are.

A special thank you to Elise Koo, my steadfast companion in a man's world these past seven years. Though two years my junior, you've always been my academic senior and a continuous source of inspiration. Even apart, we'll keep Girlbossing too close to the Sun.

To Friso Eigenhuis, thank you for doing the groceries and cooking when I was too stressed and buried in thesis work to remember to eat. Thank you to Lars & Renée for leaving the country and allowing me to focus on my work. And to all my other wonderful friends: thank you for the distractions, laughter, and support when I needed them most.

Roel Brüll deserves thanks for encouraging me to pursue my studies and reassuring my parents along the way. Thank you also to my parents for their support, *Hopelik ziet ge gruuets op mich.*

And finally, thank you to my younger self for making the bold choice to take a leap and come to Amsterdam and study Physics & Astronomy. There were a lot of times when I felt like I couldn't do it, but somehow it seems that I've managed to make it through. Because of this I am never afraid to not understand something ever again!

# Bibliography

- Allamandola, L., Tielens, A., & Barker, J. 1985, *Astrophysical Journal*, 290, L25
- Allamandola, L. J., Boersma, C., Lee, T. J., Bregman, J. D., & Temi, P. 2021, *The Astrophysical Journal Letters*, 917, L35
- Allamandola, L. J., Tielens, G. G. M., & Barker, J. R. 1989, *The Astrophysical Journal Supplement Series*, 71, 733, publisher: American Astronomical Society
- Andrews, H., Boersma, C., Werner, M. W., et al. 2015, *The Astrophysical Journal*, 807, 99, publisher: The American Astronomical Society
- Bakes, E. L. O., Tielens, A. G. G. M., & Bauschlicher, Jr., C. W. 2001, *The Astrophysical Journal*, 556, 501
- Balmer, J. E., Hung, H., Yu, Y., Letcher, R. J., & Muir, D. C. G. 2019, *Emerging Contaminants*, 5, 128
- Bauschlicher, C. W., Boersma, C., Ricca, A., et al. 2010, *The Astrophysical Journal Supplement Series*, 189, 341
- Bauschlicher, C. W., Ricca, A., Boersma, C., & Allamandola, L. J. 2018, *The Astrophysical Journal Supplement Series*, 234, 32, publisher: The American Astronomical Society
- Berné, O. & Joblin, C. 2019, *Astronomy & Astrophysics*, 632, A84, publisher: EDP Sciences
- Boersma, C., Bauschlicher, C. W., Allamandola, L. J., et al. 2010, *Astronomy and Astrophysics*, 511, A32
- Boersma, C., Bauschlicher, C. W., Ricca, A., et al. 2014, *The Astrophysical Journal Supplement Series*, 211, 8, publisher: The American Astronomical Society
- Boersma, C., Bauschlicher, C. W., Ricca, A., et al. 2011, *The Astrophysical Journal*, 729, 64, publisher: The American Astronomical Society
- Brent, R. P. 2013, *Algorithms for Minimization Without Derivatives* (Courier Corporation), google-Books-ID: AITCAgAAQBAJ

## Bibliography

---

- Bro, R. & Jong, S. 1997, Journal of Chemometrics, 11, 393
- Brown, R. H., Baines, K. H., Bellucci, G., et al. 2004, Space Science Reviews, 115, 111
- Brown, R. H., Lebreton, J.-P., & Waite, J. H., eds. 2010, Titan from Cassini-Huygens (Dordrecht: Springer Netherlands)
- Candian, A., Zhen, J., & Tielens, A. G. G. M. 2018, Physics Today, 71, 38
- Chown, R., Sidhu, A., Peeters, E., et al. 2024, Astronomy & Astrophysics, 685, A75, publisher: EDP Sciences
- Coates, A. J., Crary, F. J., Lewis, G. R., et al. 2007, Geophysical Research Letters, 34, eprint: <https://onlinelibrary.wiley.com/doi/pdf/10.1029/2007GL030978>
- Crary, F., Magee, B., Mandt, K., et al. 2009, Planetary and Space Science, 57, 1847
- Derenne, S., Coelho, C., Anquetil, C., et al. 2012, Icarus, 221, 844
- Desai, R. T., Coates, A. J., Wellbrock, A., et al. 2017, The Astrophysical Journal Letters, 844, L18, arXiv:1706.01610 [astro-ph]
- Dieck, R. H. 2007, Measurement Uncertainty: Methods and Applications (ISA)
- Dinelli, B. M., López-Puertas, M., Adriani, A., et al. 2013, Geophysical Research Letters, 40, 1489, eprint: <https://onlinelibrary.wiley.com/doi/pdf/10.1002/grl.50332>
- Désesquelles, P., Ha, M. H., Korichi, A., LeBlanc, F., & Petrache, C. 2009, Journal of Physics G-nuclear and Particle Physics - J PHYS G-NUCL PARTICLE PHYS, 36
- Flasar, F. M., Samuelson, R. E., & Conrath, B. J. 1981, Nature, 292, 693, publisher: Nature Publishing Group
- García-Comas, M., López-Puertas, M., Funke, B., et al. 2011, Icarus, 214, 571
- Gillett, F. C., Forrest, W. J., & Merrill, K. M. 1973, The Astrophysical Journal, 183, 87, publisher: American Astronomical Society
- Haythornthwaite, R. P., Coates, A. J., Jones, G. H., et al. 2021, The Planetary Science Journal, 2, 26, publisher: IOP Publishing
- Hörst, S. M. 2017, Journal of Geophysical Research: Planets, 122, 432, eprint: <https://agupubs.onlinelibrary.wiley.com/doi/pdf/10.1002/2016JE005240>
- Imanaka, H., Khare, B. N., Elsila, J. E., et al. 2004, Icarus, 168, 344, publisher: Elsevier BV

- Kaiser, R. I. & Hansen, N. 2021, *The Journal of Physical Chemistry A*, 125, 3826, publisher: American Chemical Society
- Kouatchou, J. & Medema, A. 2018, *Modeling Guru–National Aeronautics and Space Administration, USA*
- Kuiper, G. P. 1944, *Astrophysical Journal*, 100, 378
- Leger, A. & Puget, J. 1984, *Astronomy and Astrophysics*, 137, L5
- Li, A. & Draine, B. T. 2001, *The Astrophysical Journal*, 554, 778
- Li, Q., Tang, Y., Hu, W., & Li, Z. 2018, *Small*, 14, 1801560
- Lunine, J. I. 1998, in *Solar System Ices: Based on Reviews Presented at the International Symposium “Solar System Ices” held in Toulouse, France, on March 27–30, 1995*, ed. B. Schmitt, C. De Bergh, & M. Festou (Dordrecht: Springer Netherlands), 639–653
- López-Puertas, M., Dinelli, B. M., Adriani, A., et al. 2013, *The Astrophysical Journal*, 770, 132, publisher: The American Astronomical Society
- López-Puertas, M. & Taylor, F. W. 2001, *Series on Atmospheric, Oceanic and Planetary Physics*, Vol. 3, *Non-LTE Radiative Transfer in the Atmosphere* (WORLD SCIENTIFIC)
- Mackie, C. J., Candian, A., Huang, X., et al. 2018, *Physical Chemistry Chemical Physics*, 20, 1189, publisher: The Royal Society of Chemistry
- Mackie, C. J., Candian, A., Lee, T. J., & Tielens, A. G. G. M. 2021, *Theoretical Chemistry Accounts*, 140, 124
- Mackie, C. J., Peeters, E., Bauschlicher Jr., C. W., & Cami, J. 2015, *The Astrophysical Journal*, 799, 131, publisher: The American Astronomical Society
- Mallocci, G., Mulas, G., Cecchi-Pestellini, C., & Joblin, C. 2008, *Astronomy & Astrophysics*, 489, 1183, number: 3 Publisher: EDP Sciences
- Maragkoudakis, A., Boersma, C., Temi, P., Bregman, J. D., & Allamandola, L. J. 2022, *The Astrophysical Journal*, 931, 38, publisher: The American Astronomical Society
- Maragkoudakis, A., Boersma, C., Temi, P., et al. 2024, A sensitivity analysis of the modeling of Polycyclic Aromatic Hydrocarbon emission in galaxies, arXiv:2412.01875 [astro-ph]
- Mattioda, A. L., Allamandola, L. J., & Hudgins, D. M. 2005a, *The Astrophysical Journal*, 629, 1183

## Bibliography

---

- Mattioda, A. L., Hudgins, D. M., & Allamandola, L. J. 2005b, *The Astrophysical Journal*, 629, 1188
- Mattioda, A. L., Hudgins, D. M., Boersma, C., et al. 2020, *The Astrophysical Journal Supplement Series*, 251, 22, publisher: The American Astronomical Society
- Mattioda, A. L., Rutter, L., Parkhill, J., et al. 2008, *The Astrophysical Journal*, 680, 1243
- Nawaz, M. S., Ferdousi, F., Rahman, A., & Alam, A. 2014, *International Scholarly Research Notices*, Volume 2014
- Niraula, P., Wit, J. d., Hargreaves, R., Gordon, I. E., & Sousa-Silva, C. 2025, The Detection-vs-Retrieval Challenge: Titan as an Exoplanet, arXiv:2506.12144 [astro-ph]
- Nixon, C. A. 2024, *ACS Earth and Space Chemistry*, 8, 406, publisher: American Chemical Society
- Ricca, A., Boersma, C., & Peeters, E. 2021, *The Astrophysical Journal*, 923, 202, publisher: The American Astronomical Society
- Rosenberg, M. J. F., Berné, O., Boersma, C., Allamandola, L. J., & Tielens, A. G. G. M. 2011, *Astronomy & Astrophysics*, 532, A128
- Sagan, C. & Khare, B. 1979, *Nature*, 277, 102
- Sandford, S. A., Nuevo, M., Bera, P. P., & Lee, T. J. 2020, *Chemical Reviews*, 120, 4616, publisher: American Chemical Society
- Schulz, F., Maillard, J., Kaiser, K., et al. 2021, *The Astrophysical Journal Letters*, 908, L13, publisher: The American Astronomical Society
- Tielens, A. G. G. M. 2008, *Annual Review of Astronomy and Astrophysics*, 46, 289, publisher: Annual Reviews
- Tielens, A. G. G. M. 2013, *Reviews of Modern Physics*, 85, 1021, publisher: American Physical Society (APS)
- Trainer, M. G. 2013, *Current Organic Chemistry*, 17, 1710, publisher: Bentham Science Publishers
- Vuitton, V., Yelle, R., & McEwan, M. 2007, *Icarus*, 191, 722, publisher: Elsevier BV
- Vuitton, V., Yelle, R. V., & Cui, J. 2008, *Journal of Geophysical Research: Planets*, 113, \_eprint: <https://onlinelibrary.wiley.com/doi/pdf/10.1029/2007JE002997>
- Waite, J. H., Young, D. T., Cravens, T. E., et al. 2007, *Science*, 316, 870, publisher: American Association for the Advancement of Science

- Waite, J. H., Young, D. T., Westlake, J. H., et al. 2010, in *Titan from Cassini-Huygens*, ed. R. H. Brown, J.-P. Lebreton, & J. H. Waite (Dordrecht: Springer Netherlands), 201–214
- Westlake, J. H., Waite Jr., J. H., Carrasco, N., Richard, M., & Cravens, T. 2014, *Journal of Geophysical Research: Space Physics*, 119, 5951, eprint: <https://onlinelibrary.wiley.com/doi/pdf/10.1002/2014JA020208>
- Zahnle, K., Schaefer, L., & Fegley, B. 2010, *Cold Spring Harbor Perspectives in Biology*, 2, a004895, company: Cold Spring Harbor Laboratory Press Distributor: Cold Spring Harbor Laboratory Press Institution: Cold Spring Harbor Laboratory Press Label: Cold Spring Harbor Laboratory Press Publisher: Cold Spring Harbor Lab
- Zhao, L., Kaiser, R. I., Xu, B., et al. 2018, *Nature Astronomy*, 2, institution: Univ. of Hawaii at Manoa, Honolulu, HI (United States) Publisher: Springer Nature
- Zhou, L., Li, K., Li, A., & Zhou, Z. 2025, *Infrared Emission of Polycyclic Aromatic Hydrocarbon Molecules in Titan: Cyanonaphthalenes*, arXiv:2503.20147 [astro-ph]

## **Appendix A**

# **Fitting Results**

### **A.1 V1.20 neutrals**

#### **A.1.1 NNLS 900 km**

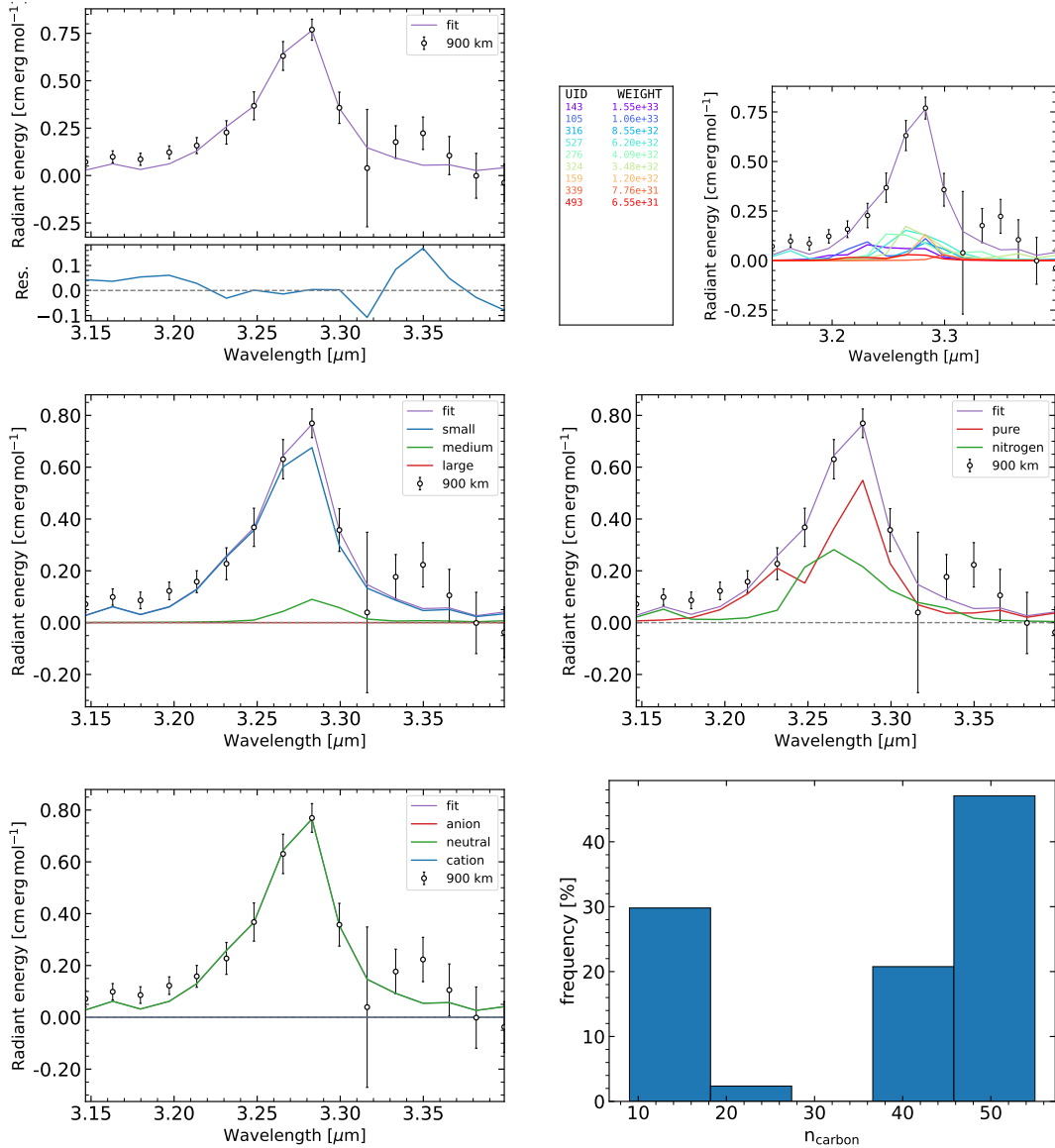


FIG. A.1 – NNLS fit breakdown for 900 km using version 1.20 of the NASA Ames database, limited to neutral PAH species. Top left: overall fit with residuals. Top right: contribution of individual PAHs, with UIDs and weights shown in legend. Center left: size breakdown into small, medium, and large PAHs. Center right: chemical composition split into pure and nitrogen-containing species. Bottom left: charge-type breakdown showing contributions from neutrals, cations, and anions. Bottom right: histogram of carbon atom counts for PAHs contributing to the fit. The reduced  $\chi^2 = 2.278$ . The PA(N)Hs in the fit are: UIDs 143 ( $C_{48}H_{22}$ ), 105 ( $C_{42}H_{18}$ ), 316 ( $C_{55}H_{20}$ ), 527 ( $C_{10}H_8N$ ), 276 ( $C_{13}H_9N$ ), 324 ( $C_{15}H_{12}$ ), 159 ( $C_{20}H_{10}$ ), 339 ( $C_{14}H_{16}$ ), and 493 ( $C_9H_7$ ).

### A.1.2 NNLS 950 km

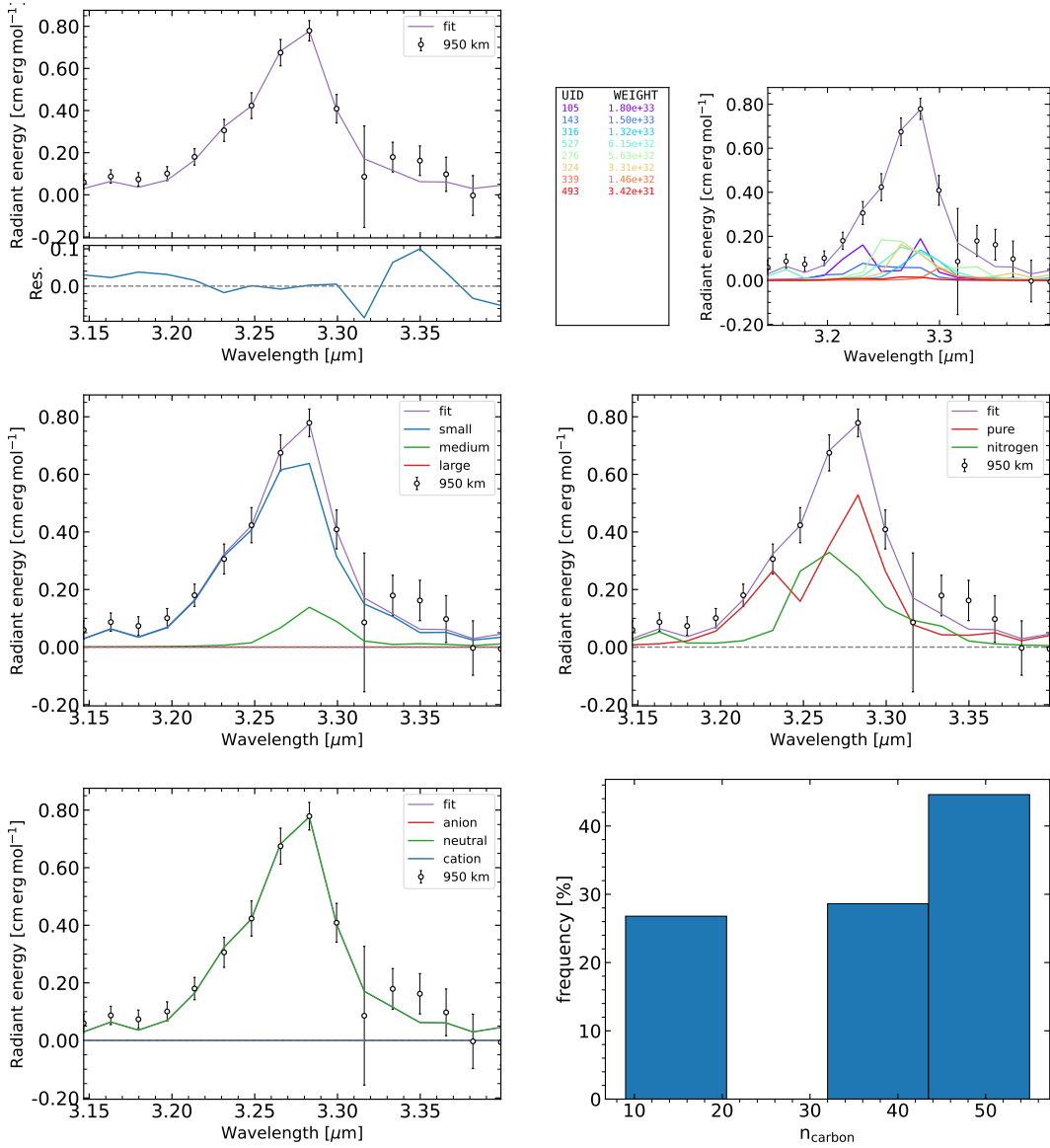


FIG. A.2 – NNLS fit breakdown for 950 km using version 1.20 of the NASA Ames database, limited to neutral PAH species. Panels show the same as in figure A.1. The reduced  $\chi^2 = 0.969$  and the PA(N)Hs present in the fit are: UIDs 105 ( $\text{C}_{42}\text{H}_{18}$ ), 143 ( $\text{C}_{48}\text{H}_{22}$ ), 316 ( $\text{C}_{55}\text{H}_{20}$ ), 527 ( $\text{C}_{10}\text{H}_8\text{N}$ ), 276 ( $\text{C}_{13}\text{H}_9\text{N}$ ), 324 ( $\text{C}_{15}\text{H}_{12}$ ), 339 ( $\text{C}_{14}\text{H}_{16}$ ), and 493 ( $\text{C}_9\text{H}_7$ ).

### A.1.3 NNLS 1000 km

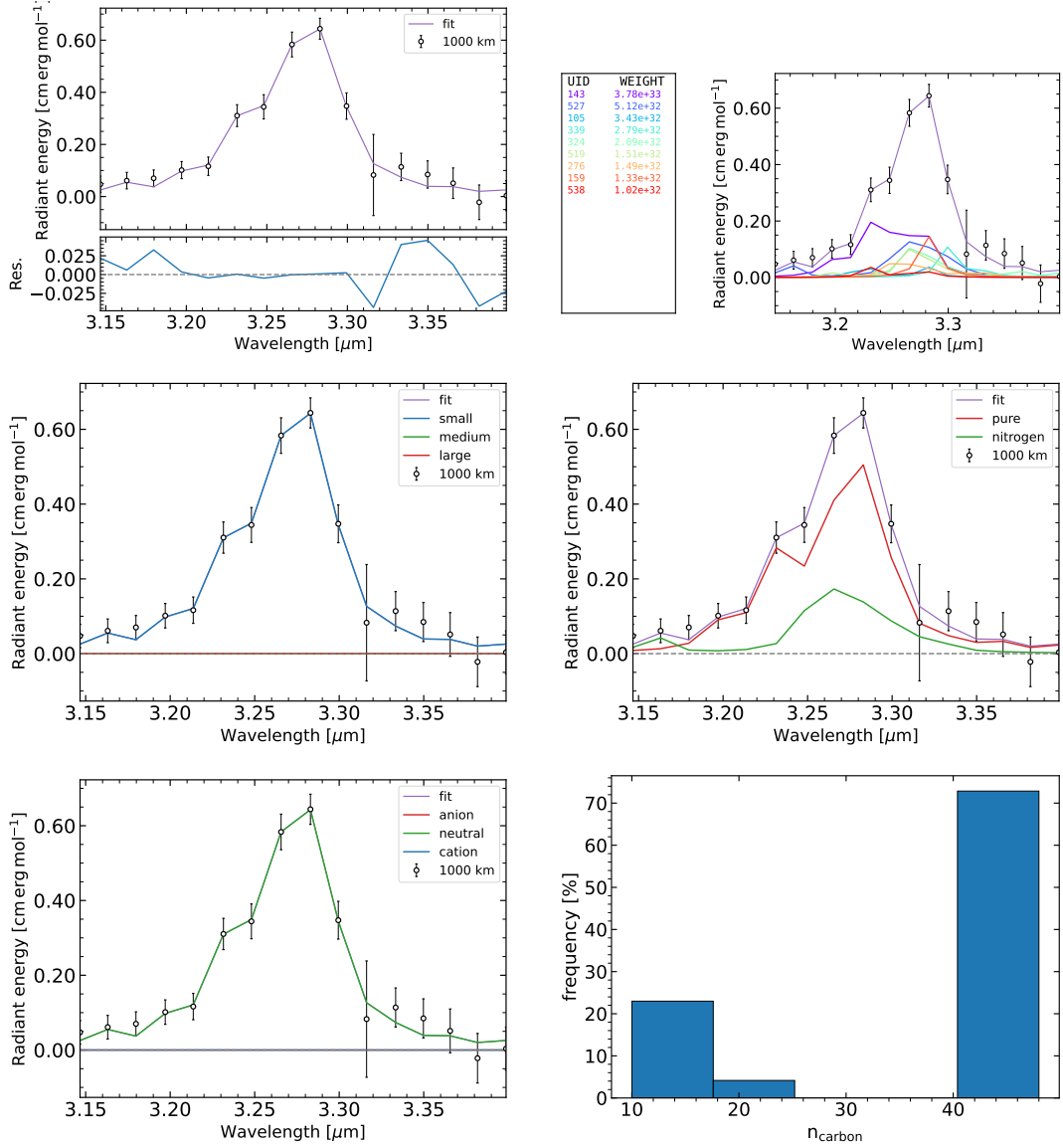


Figure A.3: NNLS fit breakdown for 1000 km using version 1.20 of the NASA Ames database, limited to neutral PAH species. Panels show the same as in figure A.1. The reduced  $\chi^2 = 0.518$  and the PA(N)Hs that make up the fit are: UIDs 143 ( $\text{C}_{48}\text{H}_{22}$ ), 527 ( $\text{C}_{10}\text{H}_8\text{N}$ ), 105 ( $\text{C}_{42}\text{H}_{18}$ ), 339 ( $\text{C}_{14}\text{H}_{16}$ ), 324 ( $\text{C}_{15}\text{H}_{12}$ ), 519 ( $\text{C}_{11}\text{H}_9$ ), 276 ( $\text{C}_{13}\text{H}_9\text{N}$ ), 159 ( $\text{C}_{20}\text{H}_{10}$ ), and 538 ( $\text{C}_{24}\text{H}_{14}$ ). 519 and 538 have not appeared in other heights.

#### A.1.4 Monte Carlo simulations

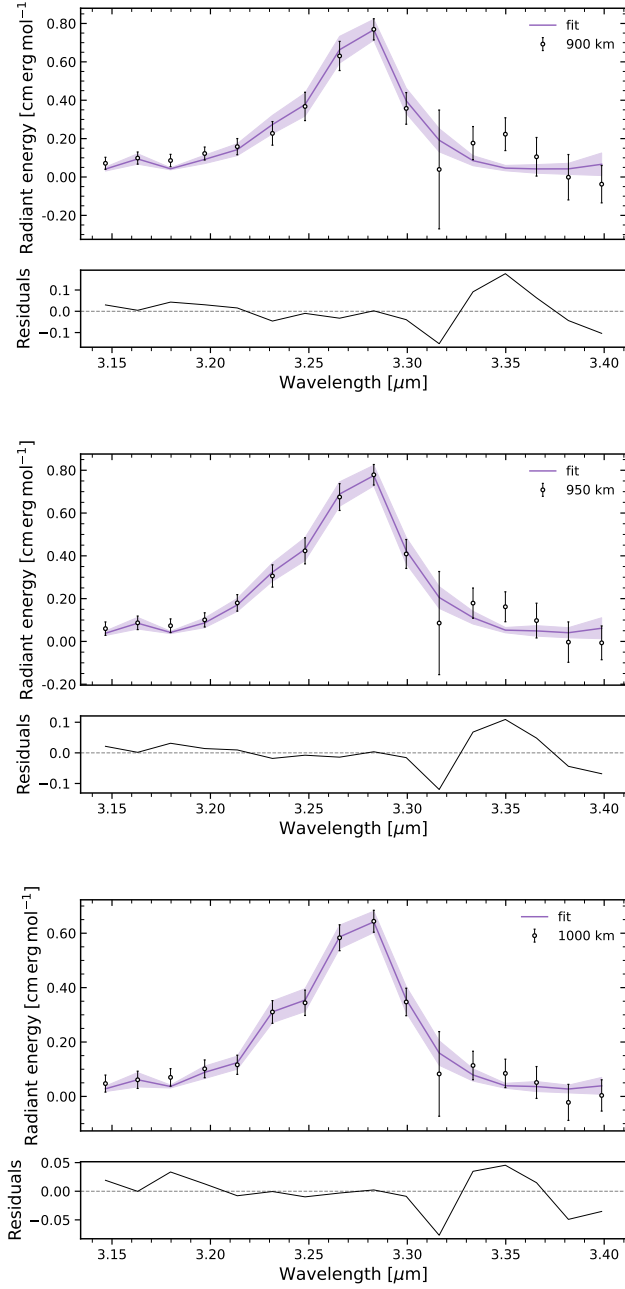


FIG. A.4 – Overview of Monte Carlo fitting results using version 1.20 of the NASA Ames database, limited to neutral PAH species. Each panel shows the ensemble-averaged fit and component breakdown at 900, 950, and 1000 km and the median reduced  $\chi^2$  values are  $\chi^2 = 2.17$ , 1.58, and 1.32, respectively.

## A.2 V3.20 neutrals + anions

### A.2.1 NNLC 900 km

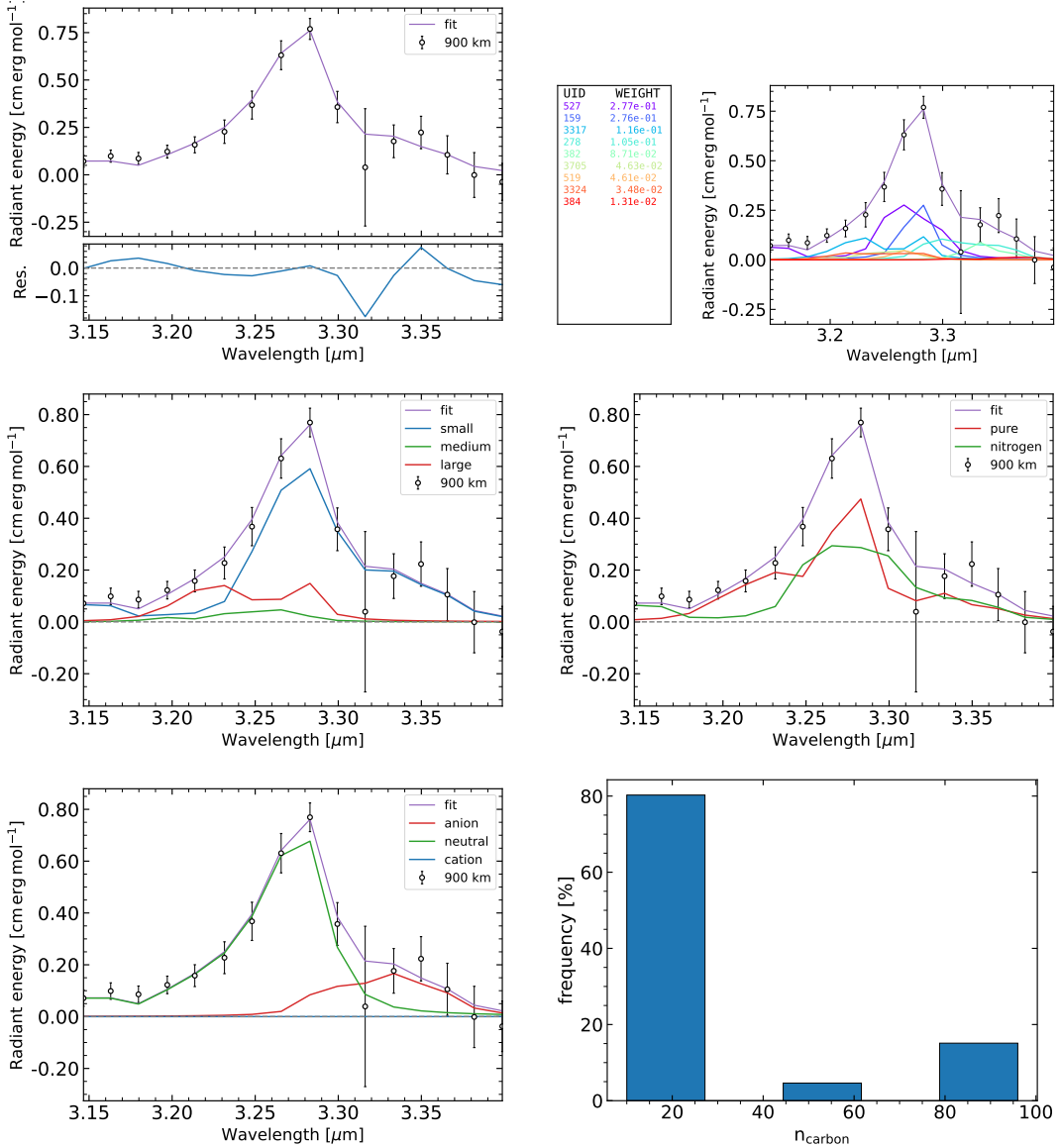


FIG. A.5 – NNLS fit breakdown for 900 km using version 3.20 of the NASA Ames database, using neutral and anionic species. Explanation of plots are the same as in figure A.1. The reduced  $\chi^2 = 0.618$ . The PA(N)Hs that make up the fit are: UIDs 527 ( $\text{C}_{10}\text{H}_8\text{N}$ ), 159 ( $\text{C}_{20}\text{H}_{10}$ ), 3317 ( $\text{C}_{96}\text{H}_{30}$ ), 278 ( $\text{C}_{13}\text{H}_9\text{N}^-$ ), 382 ( $\text{C}_{10}\text{H}_8^-$ ), 3705 ( $\text{C}_{60}\text{H}_{26}$ ), 519 ( $\text{C}_{11}\text{H}_9$ ), 3324 ( $\text{C}_{96}\text{H}_{30}$ ), and 384 ( $\text{C}_{10}\text{H}_9^-$ ). 3317, 278, 382, 3705, 3324, and 384 are new compared to the v1.20 fit.

### A.2.2 NNLC 950 km

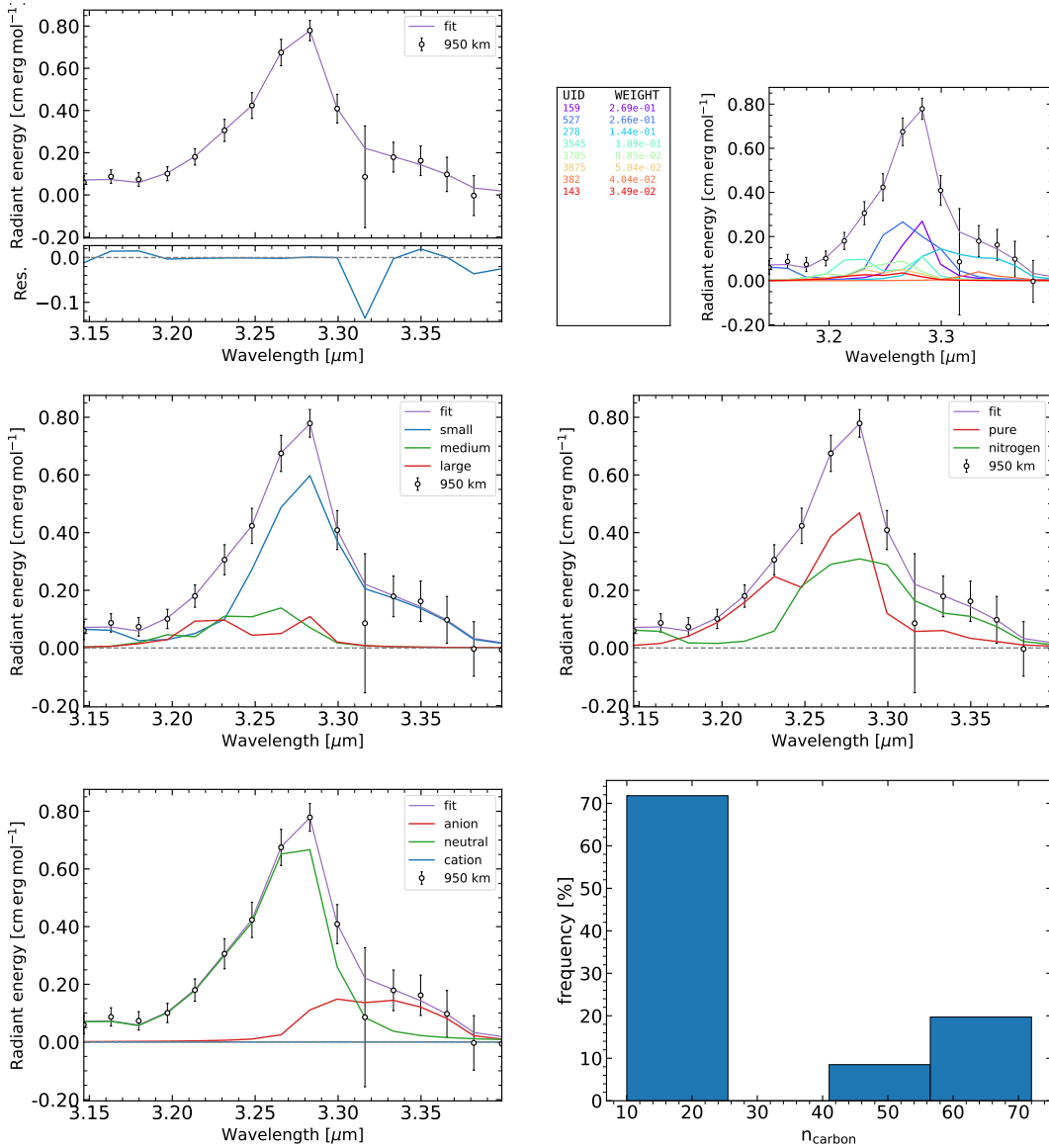


FIG. A.6 – NNLS fit breakdown for 950 km using version 3.20 of the NASA Ames database, using neutral and anionic species. Explanation of plots are the same as in figure A.1. The reduced  $\chi^2 = 0.150$ , the PA(N)Hs that make up the fit are: UIDs 159 ( $C_{20}H_{10}$ ), 527 ( $C_{10}H_8N$ ), 278 ( $C_{13}H_9N^-$ ), 3545 ( $C_{72}H_{26}$ ), 3705 ( $C_{60}H_{26}$ ), 3875 ( $C_{54}H_{24}$ ), 382 ( $C_{10}H_8^-$ ), and 143 ( $C_{48}H_{22}$ ). UID 3545 and 3875 were not seen before.

### A.2.3 NNLC 1000 km

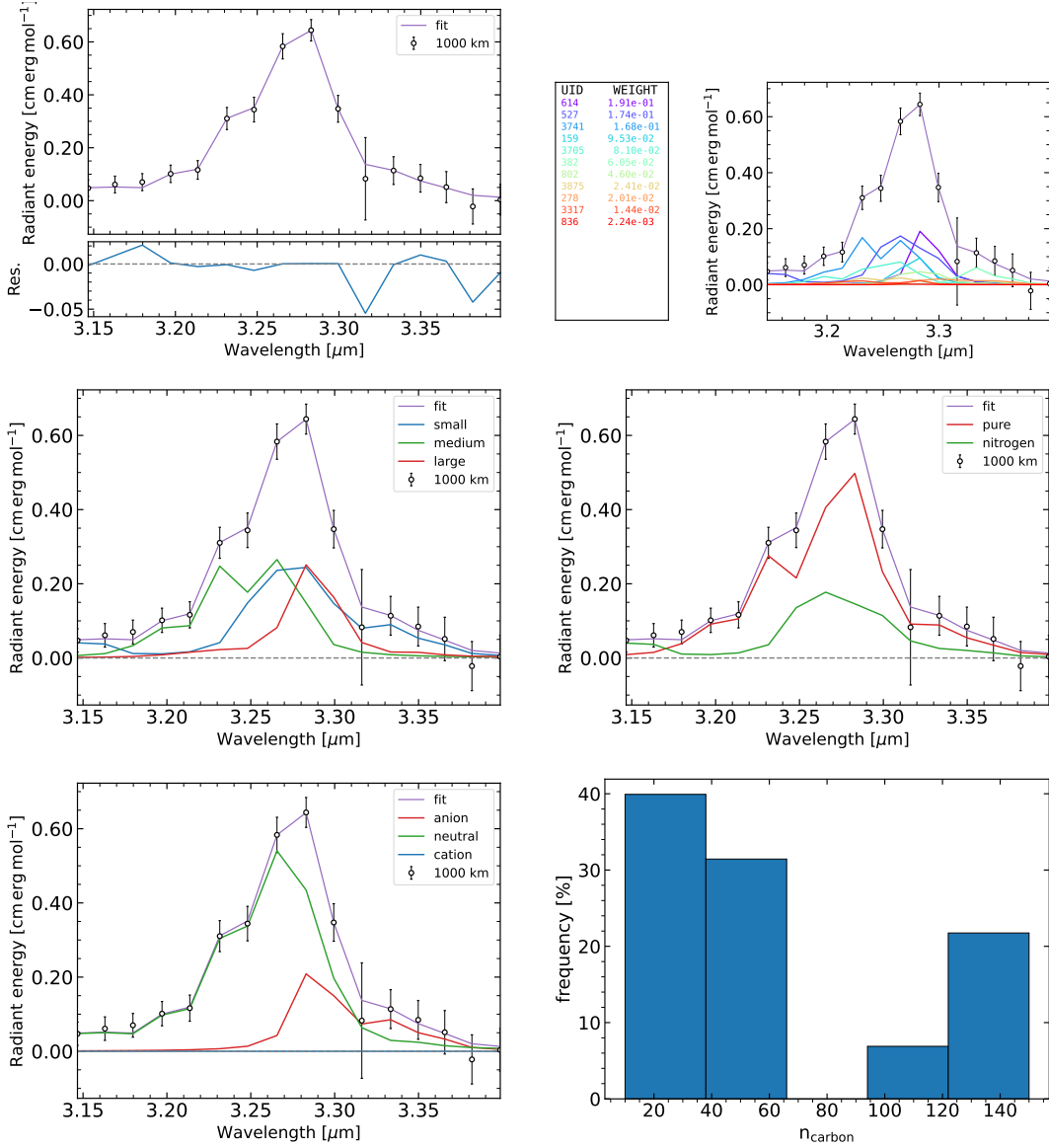


FIG. A.7 – NNLS fit breakdown for 1000 km using version 3.20 of the NASA Ames database, using neutral and anionic species. Explanation of plots are the same as in figure A.1. The reduced  $\chi^2 = 0.229$ , The PA(N)H $^-$ s that make up the fit are 614 ( $\text{C}_{150}\text{H}_{30}^-$ ), 527 ( $\text{C}_{10}\text{H}_8\text{N}$ ), 3741 ( $\text{C}_{60}\text{H}_{26}$ ), 159 ( $\text{C}_{20}\text{H}_{10}$ ), 3705 ( $\text{C}_{60}\text{H}_{26}$ ), 382 ( $\text{C}_{10}\text{H}_8^-$ ), 802 ( $\text{C}_{99}\text{H}_{28}$ ), 3875 ( $\text{C}_{54}\text{H}_{24}$ ), and 278 ( $\text{C}_{13}\text{H}_9\text{N}^-$ ), , 3317 ( $\text{C}_{96}\text{H}_{30}$ ), and 836 ( $\text{C}_{54}\text{H}_{18}$ ).

#### A.2.4 Monte Carlo simulations

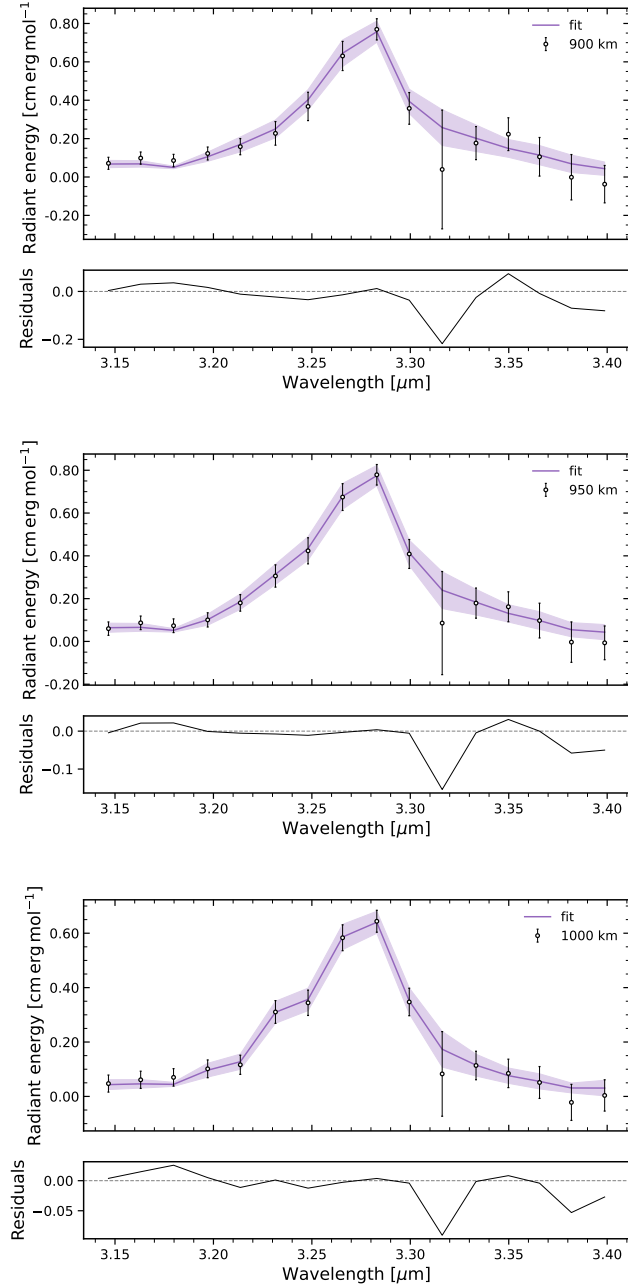


FIG. A.8 – Overview of Monte Carlo fitting results with version 3.20 of the NASA Ames database, using neutral and anionic species. Each panel shows the ensemble-averaged fit and component breakdown at 900, 950, and 1000 km, and the median reduced- $\chi^2$  values are  $\chi^2 = 1.42$ , 1.02, and 1.01, respectively.

### A.3 V3.20 neutrals + anions C<29

#### A.3.1 NNLC 900 km

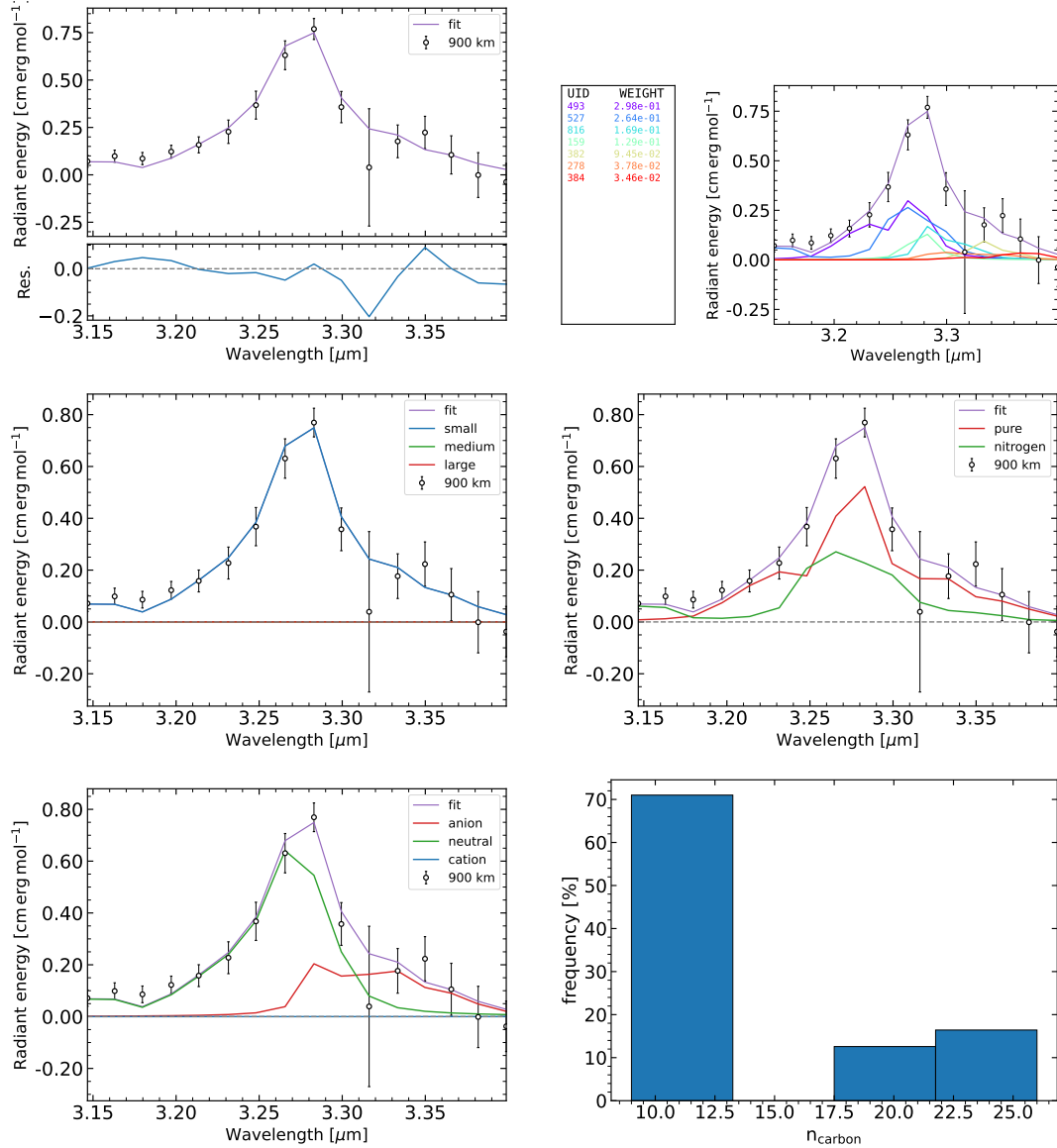


FIG. A.9 – NNLS fit breakdown for 900 km using the reduced version 3.20 of the NASA Ames database, using neutral and anionic species and C <29. Explanation of plots are the same as in figure A.1. The reduced  $\chi^2 = 0.847$ , the PA(N)Hs that make up the fit are: The PA(N)Hs that make up the fit are 493 ( $C_9H_7$ ), 527 ( $C_{10}H_8N$ ), 159 ( $C_{20}H_{10}$ ), 278 ( $C_{13}H_9N^-$ ), 816 ( $C_{26}H_{16}^-$ ), 299 ( $C_{16}H_{10}N_2$ ), 382 ( $C_{10}H_8^-$ ), and 538 ( $C_{24}H_{14}$ ).

### A.3.2 NNLC 950 km

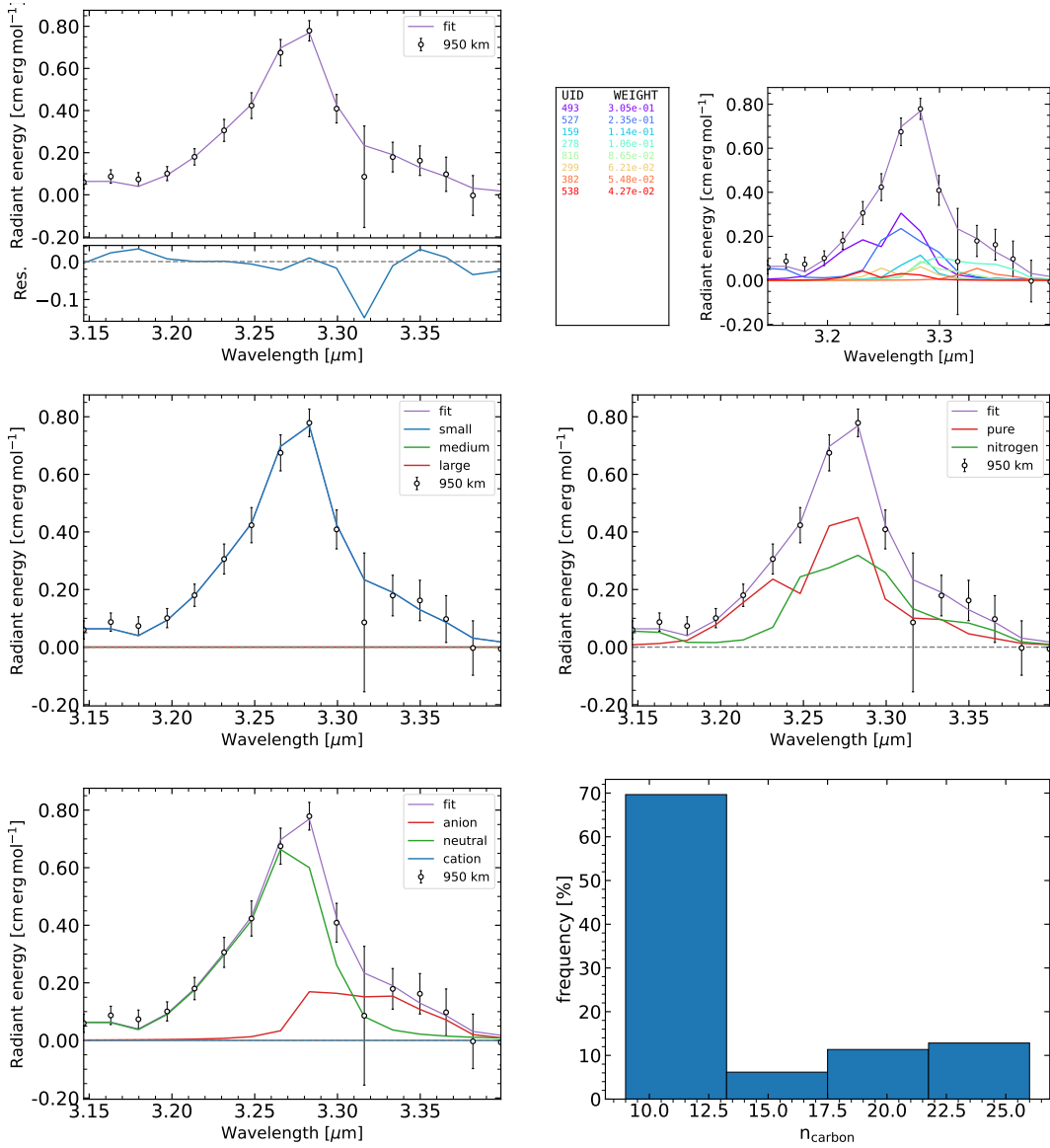


FIG. A.10 – NNLS fit breakdown for 950 km using the reduced version 3.20 of the NASA Ames database, using neutral and anionic species and C <29. Explanation of plots are the same as in figure A.1. The reduced  $\chi^2 = 0.352$ . The PA(N)Hs that make up the fit are 493 ( $C_9H_7$ ), 527 ( $C_{10}H_8N$ ), 159 ( $C_{20}H_{10}$ ), 278 ( $C_{13}H_9N^-$ ), 816 ( $C_{26}H_{16}^-$ ), 299 ( $C_{16}H_{10}N_2$ ), 382 ( $C_{10}H_8^-$ ), and 538 ( $C_{24}H_{14}$ ).

### A.3.3 NNLC 1000 km

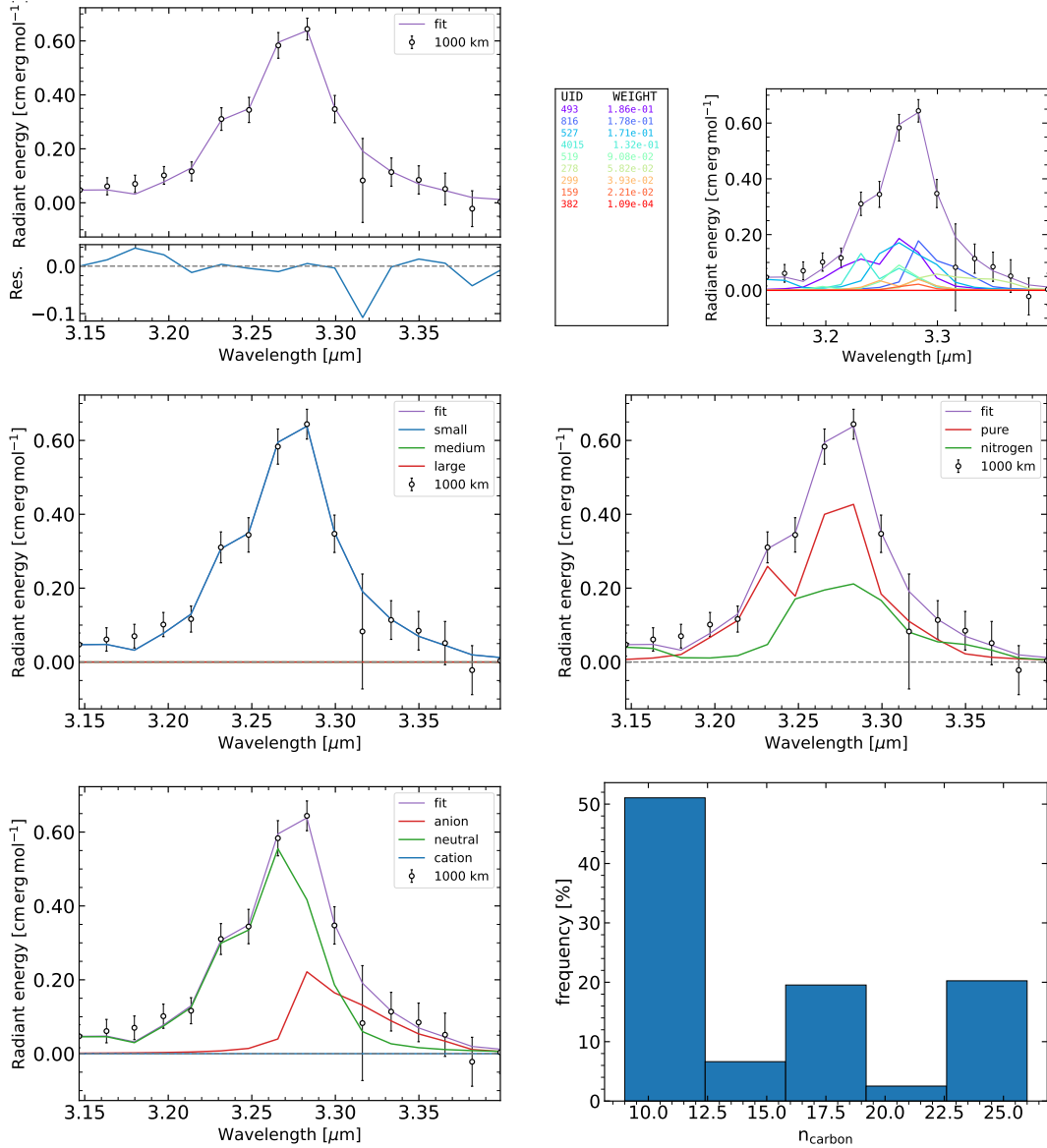


FIG. A.11 – NNLS fit breakdown for 1000 km using the reduced version 3.20 of the NASA Ames database, using neutral and anionic species and C <29. Explanation of plots are the same as in figure A.1. The reduced  $\chi^2 = 0.480$ . The PA(N)Hs that make up the fit are 493 ( $\text{C}_9\text{H}_7$ ), 816 ( $\text{C}_{26}\text{H}_{16}^-$ ), 527 ( $\text{C}_{10}\text{H}_8\text{N}$ ), 4015 (X), 519 ( $\text{C}_{11}\text{H}_9$ ), 278 ( $\text{C}_{13}\text{H}_9\text{N}^-$ ), 299 ( $\text{C}_{16}\text{H}_{10}\text{N}_2$ ), 159 ( $\text{C}_{20}\text{H}_{10}$ ), and 382 ( $\text{C}_{10}\text{H}_8^-$ ).

### A.3.4 Monte Carlo simulations

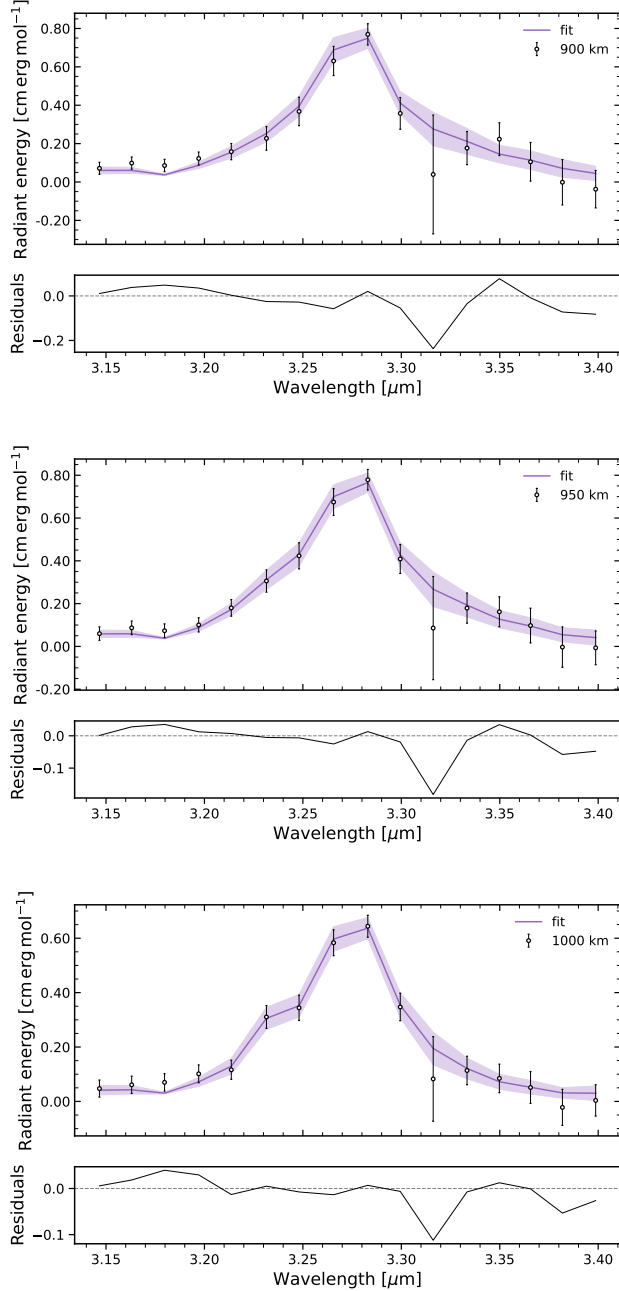


FIG. A.12 – Overview of Monte Carlo fitting results with the reduced version 3.20 of the NASA Ames database, using neutral and anionic species and  $C < 29$ . Each panel shows the ensemble-averaged fit and component breakdown at 900, 950, and 1000 km, and the median reduced- $\chi^2$  values are  $\chi^2 = 1.77$ , 1.25, and 1.33, respectively.

## A.4 V4.00 neutrals + anions

### A.4.1 NNLC 900 km

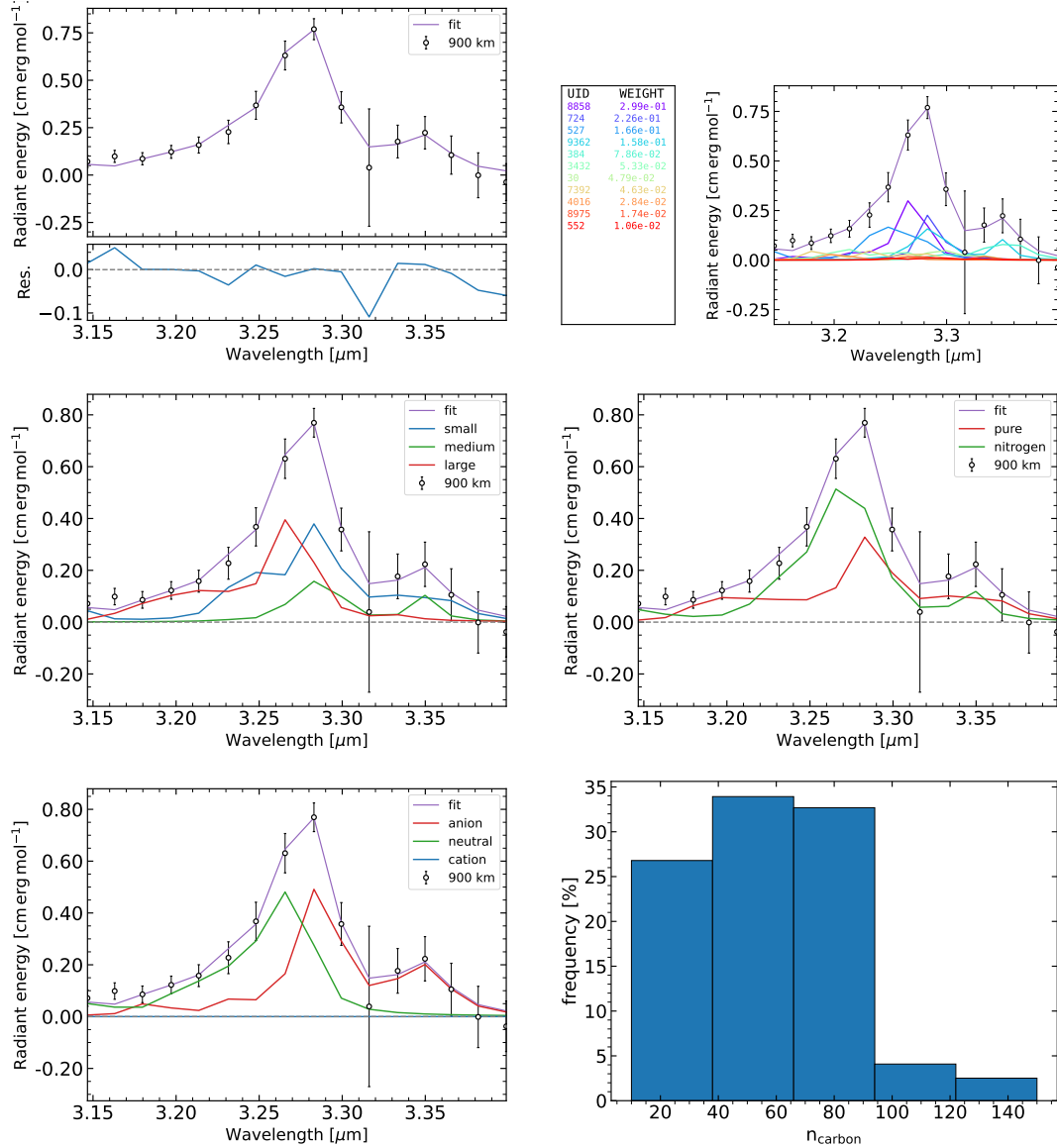


FIG. A.13 – NNLS fit breakdown for 900 km using version 4.00 of the NASA Ames database, using neutral and anionic species. Explanation of plots are the same as in figure A.1. The reduced  $\chi^2 = 0.781$ . The PA(N)Hs that make up the fit are 8858 ( $C_{93}H_{24}N_3$ ), 724 ( $C_{45}H_{15}^-$ ), 527 ( $C_{10}H_8N$ ), 9362 ( $C_{52}H_{16}N_2^-$ ), 384 ( $C_{10}H_9^-$ ), 3432 ( $C_{78}H_{28}$ ), 30 ( $C_{24}H_{13}^-$ ), 7392 ( $C_{116}H_{32}^-$ ), 4016 ( $C_{150}H_{36}$ ), 8975 ( $C_{93}H_{21}N_3^-$ ), and 552 ( $C_{20}H_{12}^-$ ).

### A.4.2 NNLC 950 km

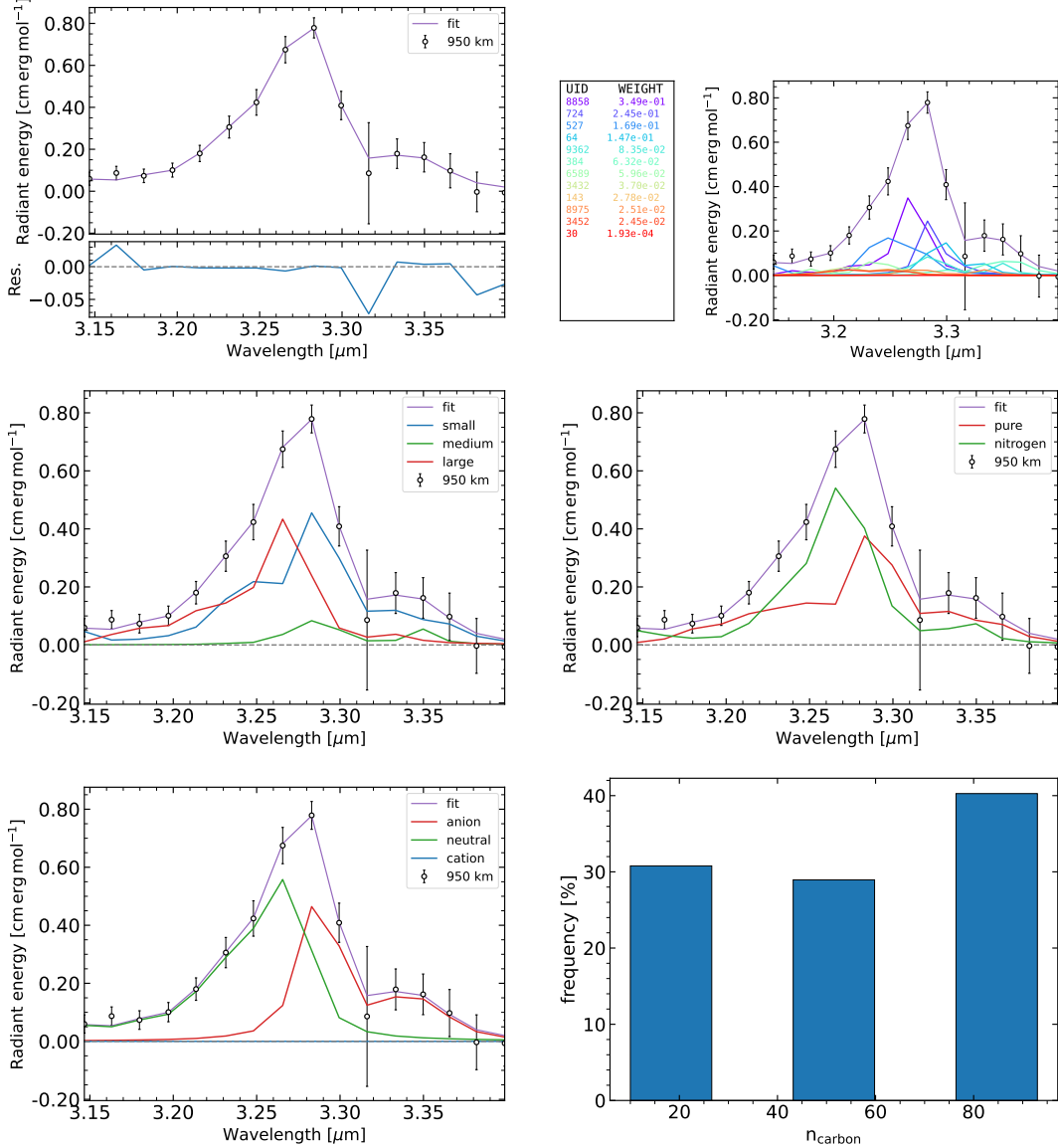


FIG. A.14 – NNLS fit breakdown for 950 km using version 4.00 of the NASA Ames database, using neutral and anionic species. Explanation of plots are the same as in figure A.1. The reduced  $\chi^2 = 0.393$ . The PA(N)Hs that make up the fit are 8858 ( $\text{C}_{93}\text{H}_{24}\text{N}_3$ ), 724 ( $\text{C}_{45}\text{H}_{15}^-$ ), 527 ( $\text{C}_{10}\text{H}_8\text{N}$ ), 64 ( $\text{C}_{19}\text{H}_{11}^-$ ), 9362 ( $\text{C}_{52}\text{H}_{16}\text{N}_2^-$ ), 384 ( $\text{C}_{10}\text{H}_9^-$ ), 6589 ( $\text{C}_{78}\text{H}_{30}$ ), 3432 ( $\text{C}_{78}\text{H}_{28}$ ), 143 ( $\text{C}_{48}\text{H}_{22}$ ), 8975 ( $\text{C}_{93}\text{H}_{21}\text{N}_3^-$ ), 3452 ( $\text{C}_{78}\text{H}_{28}$ ), and 30 ( $\text{C}_{24}\text{H}_{13}^-$ ).

### A.4.3 NNLC 1000 km

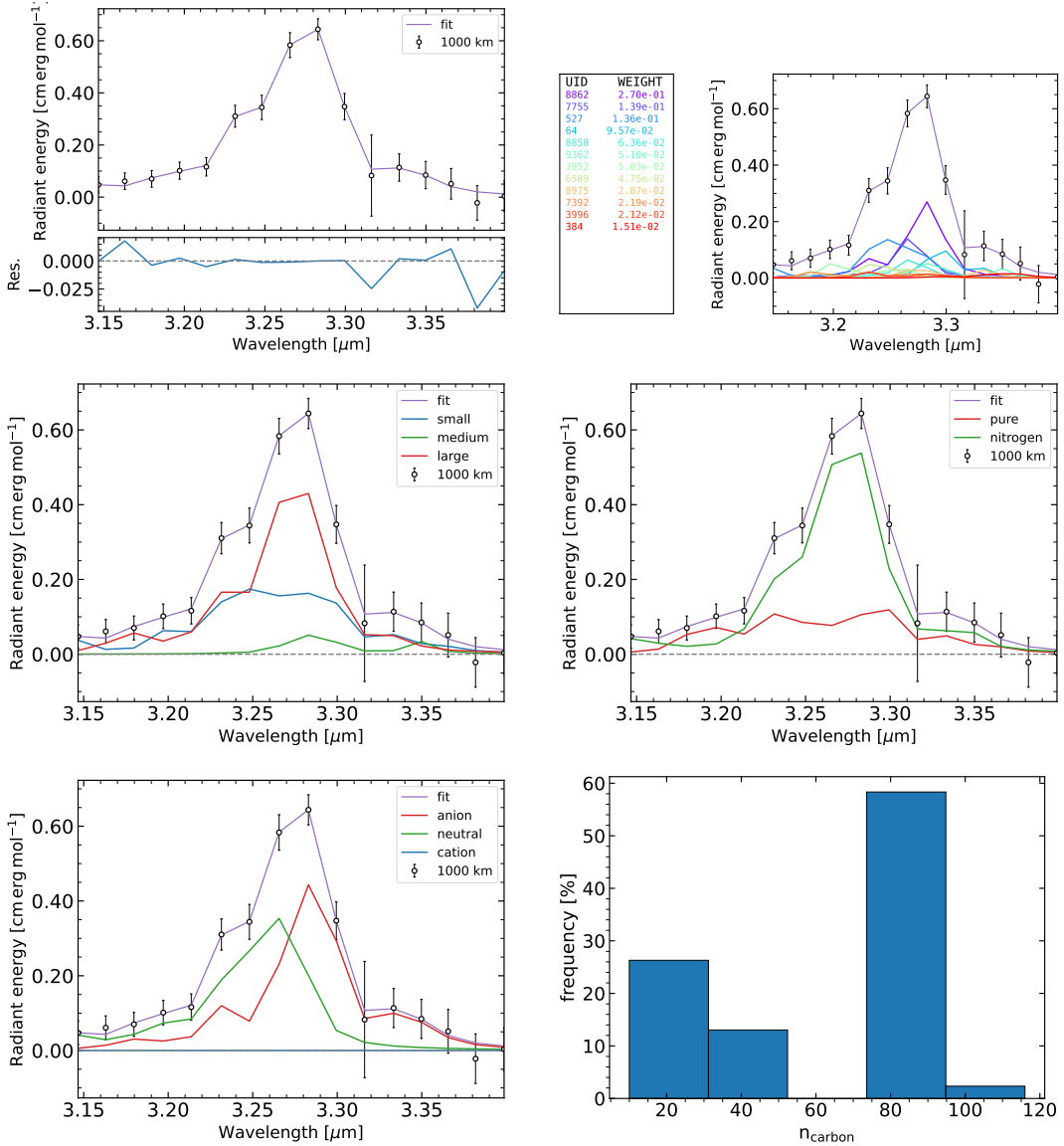


FIG. A.15 – NNLS fit breakdown for 1000 km using version 4.00 of the NASA Ames database, using neutral and anionic species. Explanation of plots are the same as in figure A.1. The reduced  $\chi^2 = 0.213$ . The PA(N)Hs that make up the fit are 8862 ( $C_{93}H_{24}N_3^-$ ), 7755 ( $C_{94}H_{24}N_2$ ), 527 ( $C_{10}H_8N$ ), 64 ( $C_{19}H_{11}^-$ ), 8858 ( $C_{93}H_{24}N_3$ ), 9362 ( $C_{52}H_{16}N_2^-$ ), 3952 ( $C_{48}H_{20}$ ), 6589 ( $C_{78}H_{30}$ ), 8975 ( $C_{93}H_{21}N_3^-$ ), 7392 ( $C_{116}H_{32}^-$ ), 3996 ( $C_{36}H_{18}^-$ ), and 384 ( $C_{10}H_9^-$ ).

#### A.4.4 Monte Carlo simulations

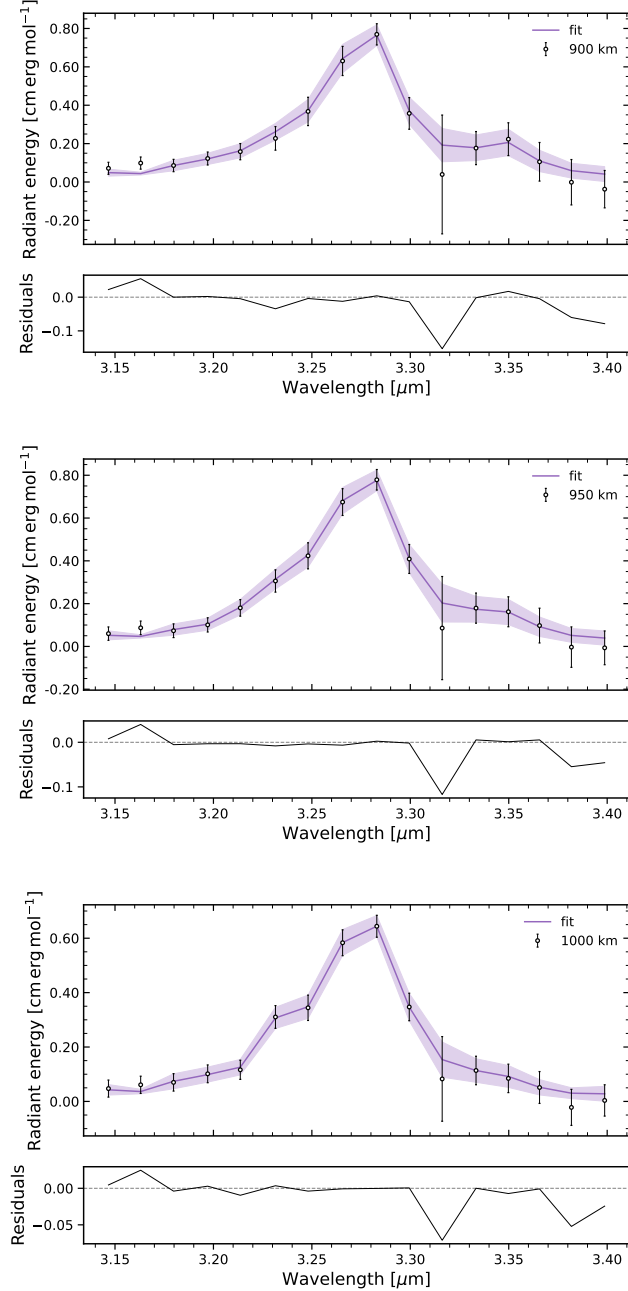


FIG. A.16 – Overview of Monte Carlo fitting results with version 4.00 of the NASA Ames database, using neutral and anionic species. Each panel shows the ensemble-averaged fit and component breakdown at 900, 950, and 1000 km, and the median reduced- $\chi^2$  values are  $\chi^2 = 1.42$ ,  $1.14$ , and  $0.92$ , respectively.

## A.5 V4.00 neutrals + anions C<29

### A.5.1 NNLC 900 km

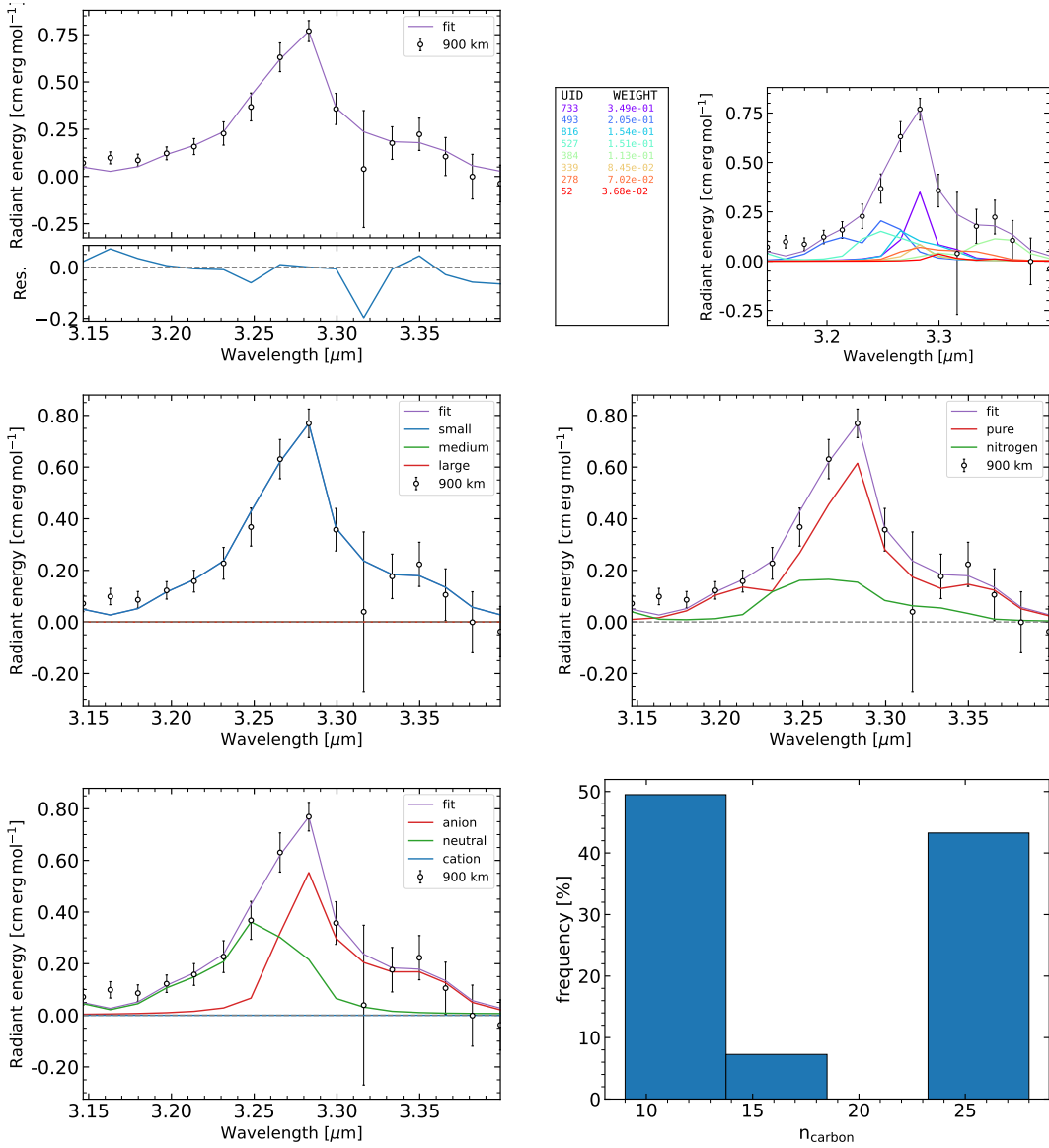


FIG. A.17 – NNLS fit breakdown for 900 km using the reduced version 4.00 of the NASA Ames database, using neutral and anionic species and C < 29. Explanation of plots are the same as in figure A.1. The reduced  $\chi^2 = 1.125$ . The PA(N)Hs that make up the fit are 733 ( $C_{28}H_{14}^-$ ), 493 ( $C_9H_7$ ), 816 ( $C_{26}H_{16}^-$ ), 527 ( $C_{10}H_8N$ ), 384 ( $C_{10}H_9^-$ ), 339 ( $C_{14}H_{16}$ ), 278 ( $C_{13}H_9N^-$ ), and 52 ( $C_{13}H_9$ ).

### A.5.2 NNLC 950 km

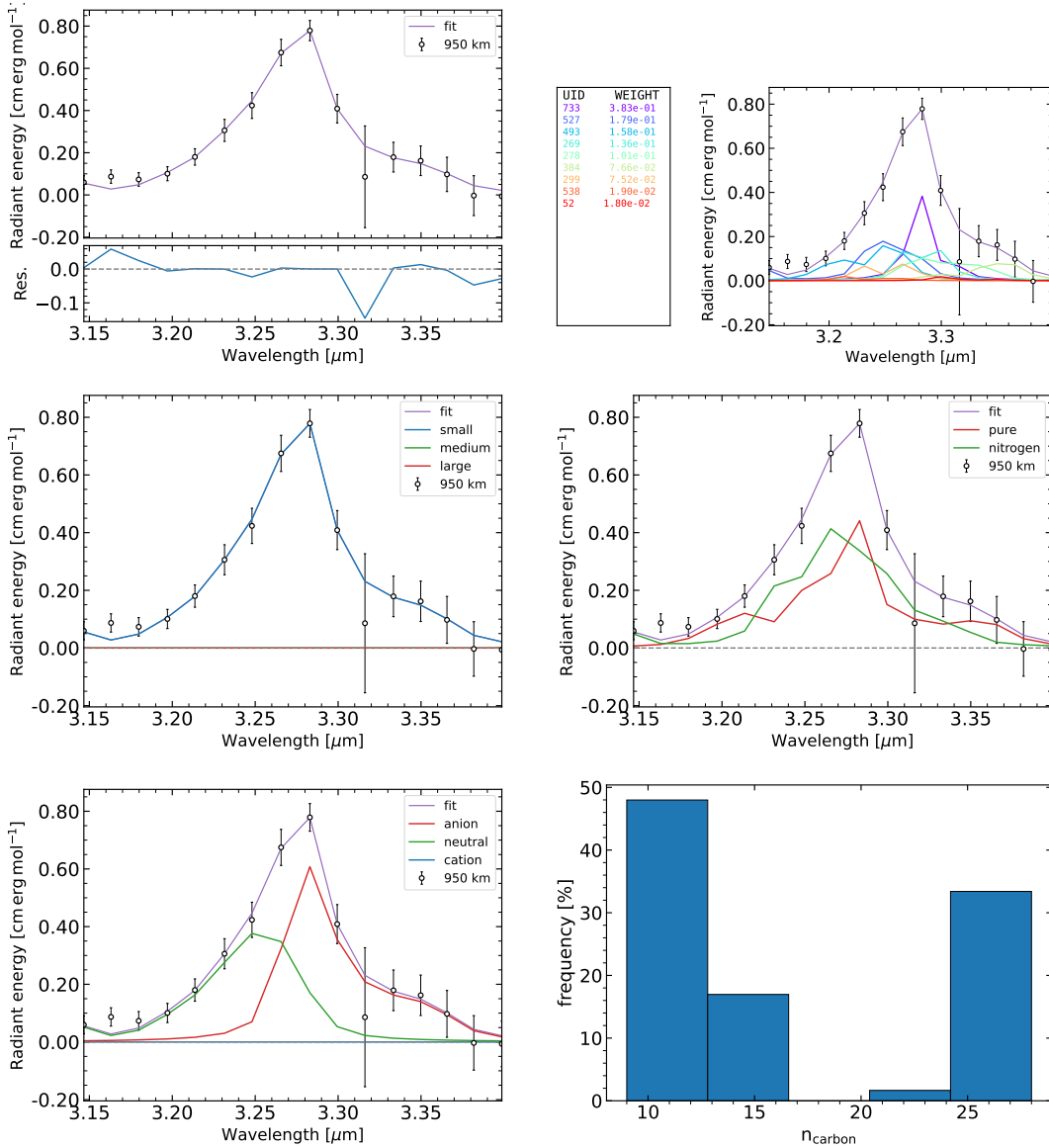


FIG. A.18 – NNLS fit breakdown for 950 km using the reduced version 4.00 of the NASA Ames database, using neutral and anionic species and  $C < 29$ . Explanation of plots are the same as in figure A.1. The reduced  $\chi^2 = 0.0726$ . The PA(N)Hs that make up the fit are 733 ( $\text{C}_{28}\text{H}_{14}^-$ ), 527 ( $\text{C}_{10}\text{H}_8\text{N}$ ), 493 ( $\text{C}_9\text{H}_7$ ), 269 ( $\text{C}_{12}\text{H}_8\text{N}_2^-$ ), 278 ( $\text{C}_{13}\text{H}_9\text{N}^-$ ), 384 ( $\text{C}_{10}\text{H}_9^-$ ), 299 ( $\text{C}_{16}\text{H}_{10}\text{N}_2$ ), 538 ( $\text{C}_{24}\text{H}_{14}$ ), and 52 ( $\text{C}_{13}\text{H}_9^-$ ).

### A.5.3 NNLC 1000 km

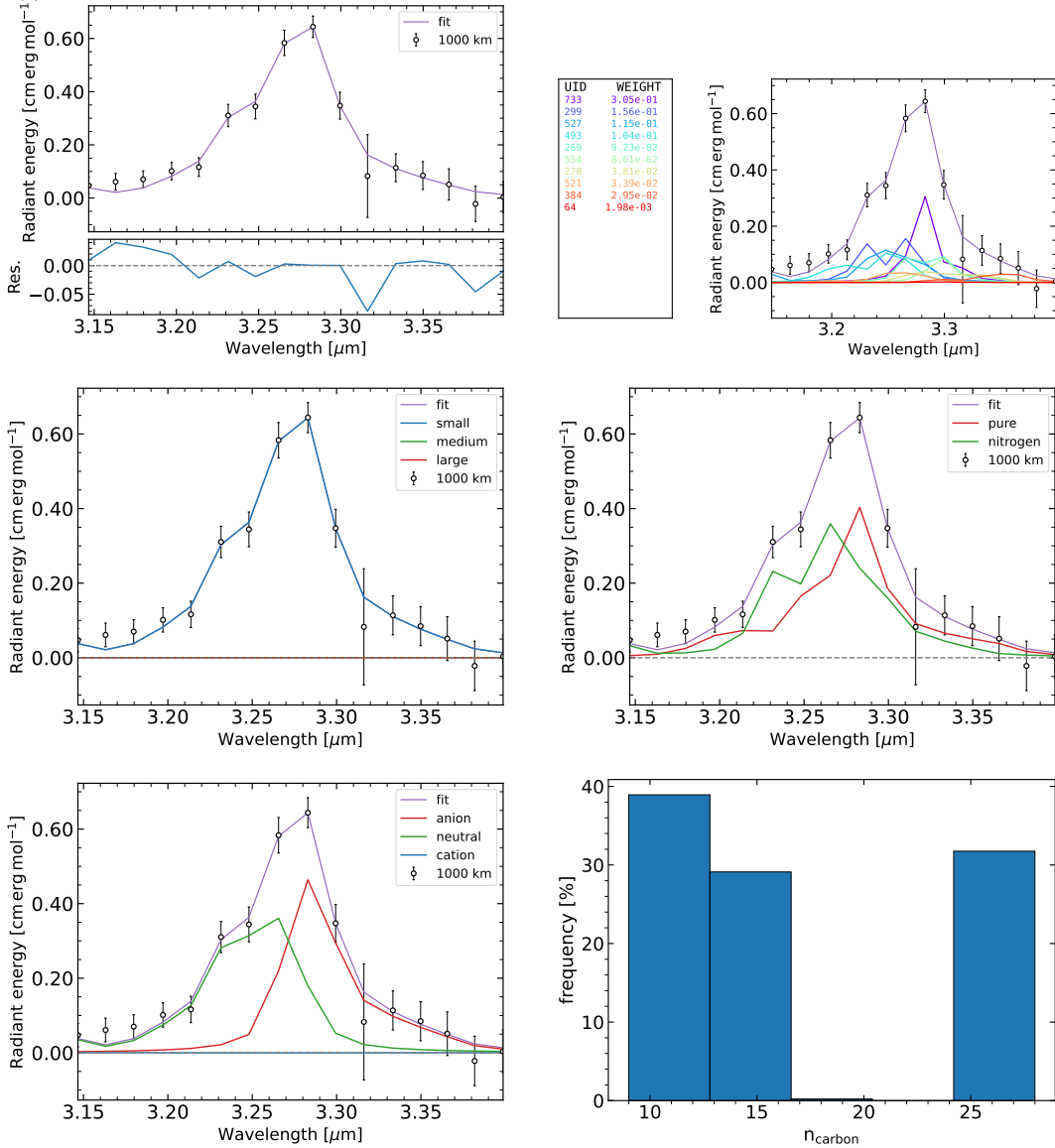


FIG. A.19 – NNLS fit breakdown for 1000 km using the reduced version 4.00 of the NASA Ames database, using neutral and anionic species and  $C < 29$ . Explanation of plots are the same as in figure A.1. The reduced  $\chi^2 = 0.734$ . The PA(N)Hs that make up the fit are 733 ( $\text{C}_{28}\text{H}_{14}^-$ ), 299 ( $\text{C}_{16}\text{H}_{10}\text{N}_2$ ), 527 ( $\text{C}_{10}\text{H}_8\text{N}$ ), 493 ( $\text{C}_9\text{H}_7$ ), 269 ( $\text{C}_{12}\text{H}_8\text{N}_2^-$ ), 554 ( $\text{C}_{16}\text{H}_{10}^-$ ), 278 ( $\text{C}_{13}\text{H}_9\text{N}^-$ ), 521 ( $\text{C}_{11}\text{H}_9$ ), 384 ( $\text{C}_{10}\text{H}_9^-$ ), and 64 ( $\text{C}_{19}\text{H}_{11}^-$ ).

#### A.5.4 Monte Carlo simulations

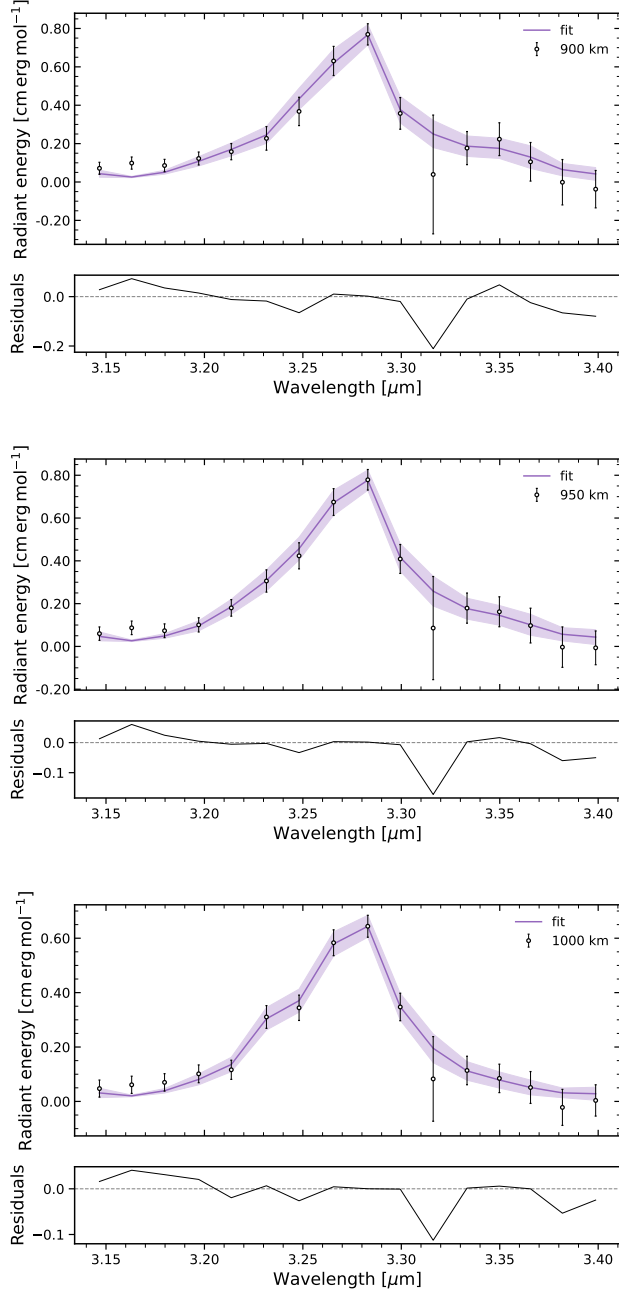


FIG. A.20 – Overview of Monte Carlo fitting results with the reduced version 4.00 of the NASA Ames database, using neutral and anionic species and C <29. Each panel shows the ensemble-averaged fit and component breakdown at 900, 950, and 1000 km, and the median reduced- $\chi^2$  values are  $\chi^2 = 2.03, 1.59$ , and  $1.44$ , respectively.

## A.6 Single PAH signals

In this section we fit the signal of singular PAHs in the atmosphere of Titan, at 950 km. We do this to see how the spectral shape of the modelled signal holds up to the VIMS spectrum and make inferences about what PAHs are necessary to produce the spectral shape.

## Single PAH signals

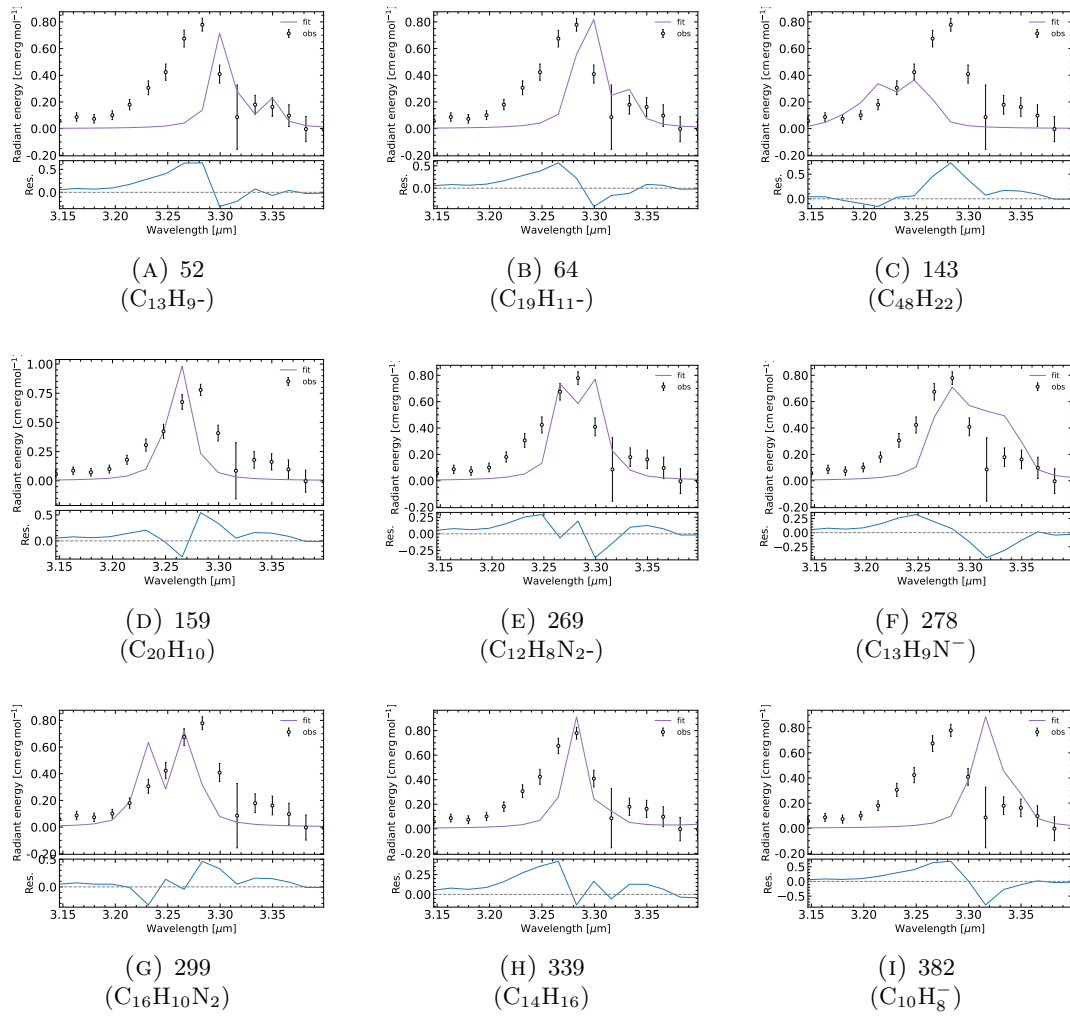


FIG. A.21 – Theoretical emission spectra of PAHs used in this study (UIDs 52–382). Each panel shows one molecule normalized at 950 km for comparison.

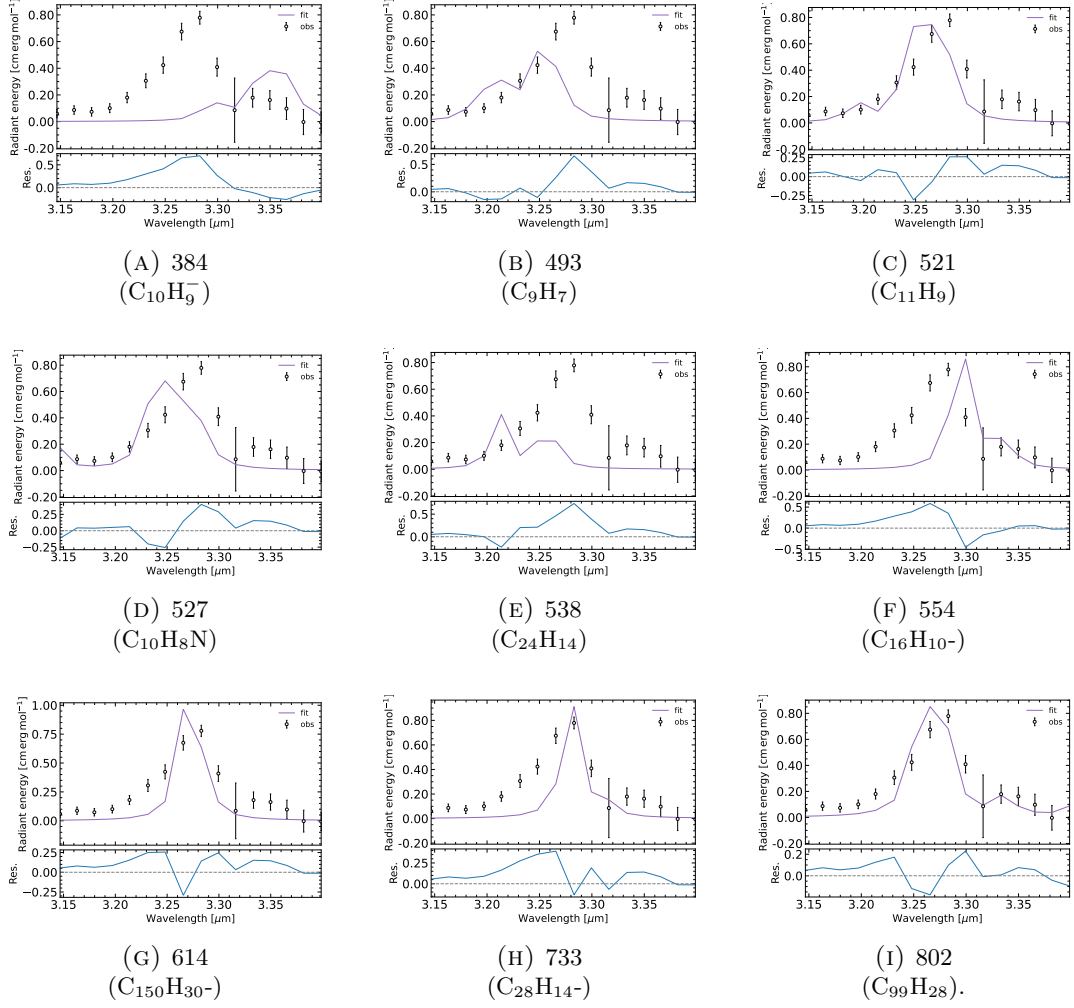


FIG. A.22 – Theoretical emission spectra of PAHs used in this study (UIDs 384–802).

## Single PAH signals

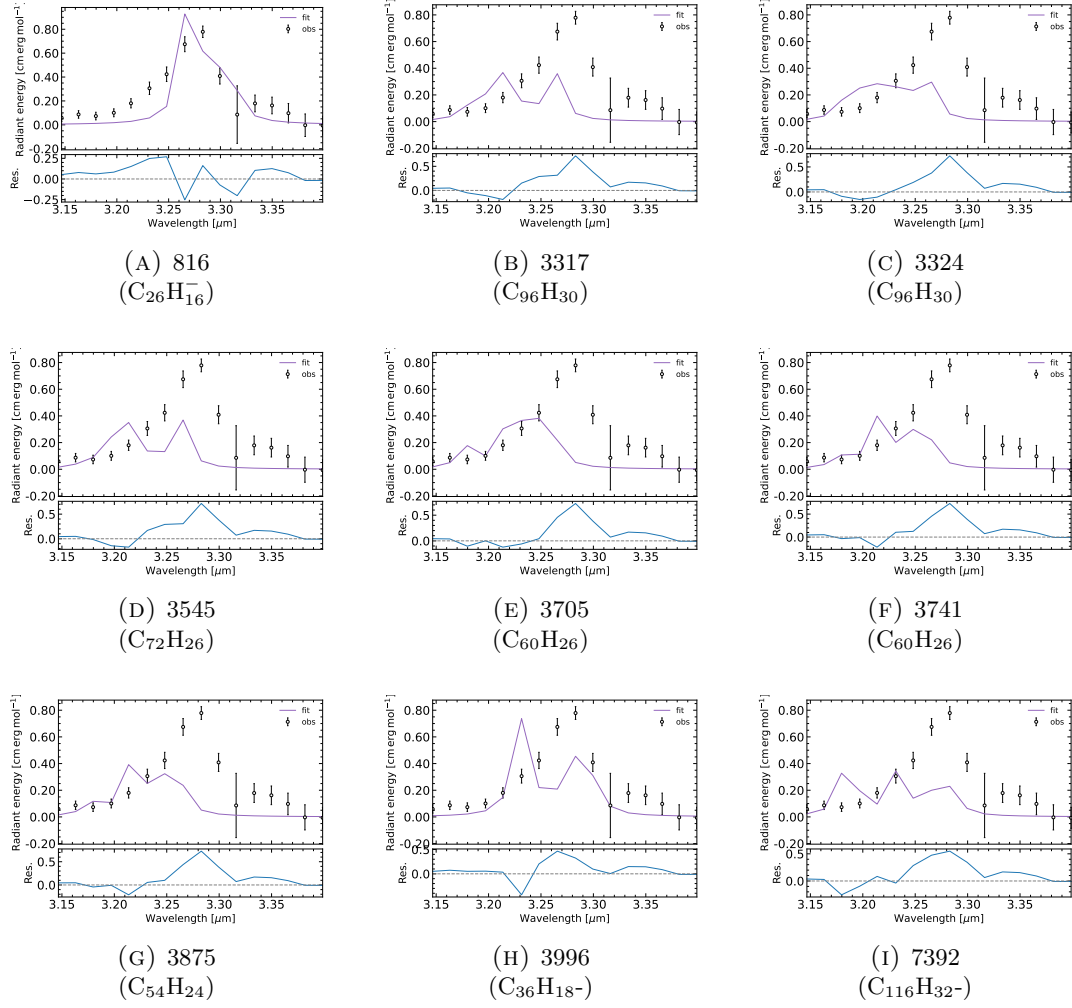


FIG. A.23 – Theoretical emission spectra of PAHs used in this study (UIDs 816–7392).

## Appendix B

### NIST list

TABLE B.1

Name	Molecular	wavelength ( $\mu\text{m}$ )	wavenumber ( $\text{cm}^{-1}$ )
1-Azetine	C <sub>3</sub> H <sub>5</sub> N	3,316749585	3015
1-Butyl radical	C <sub>4</sub> H <sub>9</sub>	3,306878307	3024
1-Pentyl radical	C <sub>5</sub> H <sub>11</sub>	3,305785124	3025
1,3-Butadiene	C <sub>4</sub> H <sub>6</sub>	3,273322422	3055
2-Methylallyl radical	C <sub>4</sub> H <sub>7</sub>	3,305785124	3025
2H-Azirine	C <sub>2</sub> H <sub>3</sub> N	3,265839321	3062
4-CH <sub>3</sub> (cyc-C <sub>7</sub> H <sub>5</sub> )	C <sub>8</sub> H <sub>8</sub>	3,305785124	3025
4-CH <sub>3</sub> (cyc-C <sub>7</sub> H <sub>5</sub> )	C <sub>8</sub> H <sub>8</sub>	3,28731098	3042
4-CH <sub>3</sub> (cyc-C <sub>7</sub> H <sub>5</sub> )	C <sub>8</sub> H <sub>8</sub>	3,25732899	3070
5-CH <sub>3</sub> (cyc-C <sub>7</sub> H <sub>5</sub> )	C <sub>8</sub> H <sub>8</sub>	3,311258278	3020
5-CH <sub>3</sub> (cyc-C <sub>7</sub> H <sub>5</sub> )	C <sub>8</sub> H <sub>8</sub>	3,28731098	3042
Allene	C <sub>3</sub> H <sub>4</sub>	3,316749585	3015
Allyl radical	C <sub>3</sub> H <sub>5</sub>	3,311258278	3020
Allyl radical	C <sub>3</sub> H <sub>5</sub>	3,311258278	3020
Allyl radical	C <sub>3</sub> H <sub>5</sub>	3,307972213	3023
Allyl radical	C <sub>3</sub> H <sub>5</sub>	3,303600925	3027
Allyl radical	C <sub>3</sub> H <sub>5</sub>	3,295978906	3034
Allyl radical	C <sub>3</sub> H <sub>5</sub>	3,276539974	3052
Benzyl radical	C <sub>7</sub> H <sub>7</sub>	3,258390355	3069
Benzyne	C <sub>6</sub> H <sub>4</sub>	3,279763857	3049
Benzyne	C <sub>6</sub> H <sub>4</sub>	3,256268317	3071
c-CH <sub>3</sub> CH=NH	C <sub>2</sub> H <sub>5</sub> N	3,313452618	3018
C(CH <sub>2</sub> ) <sub>3</sub>	C <sub>4</sub> H <sub>6</sub>	3,312355084	3019
C(CH <sub>2</sub> ) <sub>3</sub>	C <sub>4</sub> H <sub>6</sub>	3,299241175	3031
C <sub>3</sub> H <sub>7</sub> N	C <sub>3</sub> H <sub>7</sub> N	3,25732899	3070
C <sub>6</sub> H <sub>5</sub> CCH <sub>3</sub>	C <sub>8</sub> H <sub>8</sub>	3,291639236	3038

**Table B.1 continued from previous page**

C6H5CCH3	C <sub>8</sub> H <sub>8</sub>	3,25203252	3075
CH <sub>2</sub> =C	C <sub>2</sub> H <sub>2</sub>	3,305785124	3025
CH2CCH	C <sub>3</sub> H <sub>3</sub>	3,302509908	3028
cyc-C3H5	C <sub>3</sub> H <sub>5</sub>	3,297065612	3033
cyc-C3H5	C <sub>3</sub> H <sub>5</sub>	3,288391976	3041
cyc-C3H5	C <sub>3</sub> H <sub>5</sub>	3,28731098	3042
cyc-C3H5	C <sub>3</sub> H <sub>5</sub>	3,286230693	3043
cyc-C3H5	C <sub>3</sub> H <sub>5</sub>	3,279763857	3049
cyc-C6H5N	C <sub>6</sub> H <sub>5</sub> N	3,305785124	3025
cyc-C6H7	C <sub>6</sub> H <sub>7</sub>	3,300330033	3030
cyc-C6H7	C <sub>6</sub> H <sub>7</sub>	3,278688525	3050
cyc-C7H6	C <sub>7</sub> H <sub>6</sub>	3,318951211	3013
cyc-C7H6	C <sub>7</sub> H <sub>6</sub>	3,310162198	3021
cyc-C7H6	C <sub>7</sub> H <sub>6</sub>	3,291639236	3038
cyc-C7H6	C <sub>7</sub> H <sub>6</sub>	3,288391976	3041
cyc-C7H6	C <sub>7</sub> H <sub>6</sub>	3,280839895	3048
Cyclopropane	C <sub>3</sub> H <sub>6</sub>	3,305785124	3025
Cyclopropane	C <sub>3</sub> H <sub>6</sub>	3,291639236	3038
Ethenamine, N-methyl-	C <sub>3</sub> H <sub>7</sub> N	3,292723082	3037
Ethyl radical	C <sub>2</sub> H <sub>5</sub>	3,297065612	3033
Ethyl radical	C <sub>2</sub> H <sub>5</sub>	3,297065612	3033
Ethyl radical	C <sub>2</sub> H <sub>5</sub>	3,292723082	3037
Ethylenimine	C <sub>2</sub> H <sub>5</sub> N	3,316749585	3015
H2C=C=NCH3	C <sub>3</sub> H <sub>5</sub> N	3,278688525	3050
H2C=C=NCN	C <sub>3</sub> H <sub>2</sub> N <sub>2</sub>	3,294892916	3035
H2C=C=NCN	C <sub>3</sub> H <sub>2</sub> N <sub>2</sub>	3,28407225	3045
i-C4H9	C <sub>4</sub> H <sub>9</sub> -	3,307972213	3023
Isopropyl radical	C <sub>3</sub> H <sub>7</sub>	3,276539974	3052
m-Benzyne	C <sub>6</sub> H <sub>4</sub>	3,292723082	3037
m-CH3C6H4CH:	C <sub>8</sub> H <sub>8</sub>	3,30141961	3029
m-CH3C6H4CH:	C <sub>8</sub> H <sub>8</sub>	3,281916639	3047
m-CH3C6H4CH:	C <sub>8</sub> H <sub>8</sub>	3,255208333	3072
Methanimine	CH <sub>3</sub> N	3,306878307	3024
Methanimine	CH <sub>3</sub> N	3,293807642	3036
Methyl isocyanide	C <sub>2</sub> H <sub>3</sub> N	3,317850033	3014
N-Methyl methanimine	C <sub>2</sub> H <sub>5</sub> N	3,306878307	3024
n-Propyl radical	C <sub>3</sub> H <sub>7</sub>	3,313452618	3018
Neopentyl radical	C <sub>5</sub> H <sub>11</sub>	3,311258278	3020
o-Xylylene	C <sub>8</sub> H <sub>8</sub>	3,28407225	3045
o-Xylylene	C <sub>8</sub> H <sub>8</sub>	3,25732899	3070
p-(CH2)2C6H4	C <sub>8</sub> H <sub>8</sub>	3,291639236	3038
p-(CH2)2C6H4	C <sub>8</sub> H <sub>8</sub>	3,281916639	3047

**Table B.1 continued from previous page**

p-(CH <sub>2</sub> ) <sub>2</sub> C <sub>6</sub> H <sub>4</sub>	C <sub>8</sub> H <sub>8</sub>	3,269042171	3059
p-CH <sub>3</sub> C <sub>6</sub> H <sub>4</sub> CH:	C <sub>8</sub> H <sub>8</sub>	3,310162198	3021
p-CH <sub>3</sub> C <sub>6</sub> H <sub>4</sub> CH:	C <sub>8</sub> H <sub>8</sub>	3,275466754	3053
p-CH <sub>3</sub> C <sub>6</sub> H <sub>4</sub> CH:	C <sub>8</sub> H <sub>8</sub>	3,25414904	3073
p-HC=C <sub>6</sub> H <sub>4</sub> =CH	C <sub>8</sub> H <sub>6</sub>	3,277613897	3051
PhCH	C <sub>7</sub> H <sub>6</sub>	3,294892916	3035
PhCH	C <sub>7</sub> H <sub>6</sub>	3,267973856	3060
PhCH	C <sub>7</sub> H <sub>6</sub>	3,25414904	3073
Phenyl radical	C <sub>6</sub> H <sub>5</sub>	3,292723082	3037
Phenyl radical	C <sub>6</sub> H <sub>5</sub>	3,267973856	3060
Phenyl radical	C <sub>6</sub> H <sub>5</sub>	3,256268317	3071
Phenyl radical	C <sub>6</sub> H <sub>5</sub>	3,255208333	3072
Phenyl radical	C <sub>6</sub> H <sub>5</sub>	3,255208333	3072
Propadienylidene	C <sub>3</sub> H <sub>2</sub>	3,278688525	3050
Propadienylidene	C <sub>3</sub> H <sub>2</sub>	3,267973856	3060
t-CH <sub>3</sub> CH=NH	C <sub>2</sub> H <sub>5</sub> N	3,313452618	3018